TÉCNICO LISBOA

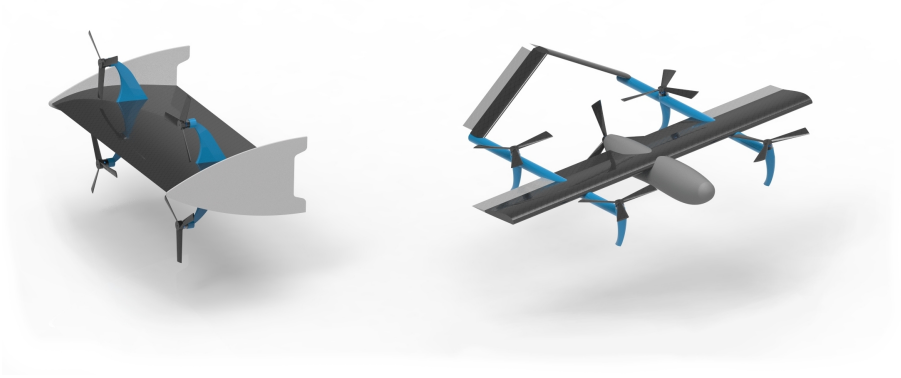

Modelling, Simulation and Control of two Hybrids between a Quadrotor and a Fixed Wing Aircraft

Bruno Miguel Gomes de Oliveira

Thesis to obtain the Master of Science Degree in

Mechanical Engineering

Supervisor: Prof. José Raúl Carreira Azinheira

Examination Committee

Chairperson: Prof. Paulo Jorge Coelho Ramalho Oliveira
Supervisor: Prof. José Raúl Carreira Azinheira
Member of the Committee: Prof. Filipe Szolnoky Ramos Pinto Cunha

June 2017

Dedicated to those in my life

Acknowledgements

First, would like to thank my advisor, Professor José Raul Azinheira, for his support, guidance, and availability throughout the course of this work.

Also want to thank my friends, who spend the last few months working on their thesis at SEDEM, side by side with me, for their fellowship and support.

And thank all my friends and family for their support, not only throughout this thesis but during the past few years.

Resumo

Durante a ultima década ocorreu uma explosão de desenvolvimento de veículos de descolagem e aterragem vertical (VTOL), como quadrotors, hexarotors, e semelhantes. Mas em anos mais recentes tem aumentado o interesse em veículos capazes de descolar verticalmente e capazes de realizar voo como um avião, para superar algumas das limitações dos quadrotors.

Este trabalho pretende realizar uma análise preliminar deste tipo de veículos, para avaliar as suas vantagens e desvantagens.

Duas abordagens diferentes deste tipo de veículos foram escolhidas, para proporcionar uma visão mais alargada do que pode ser conseguido. E para esses veículos, foi obtido um modelo dinâmico e cinemático extenso.

Devido a condições específicas de funcionamento destes veículos, um modelo mais avançado para as hélices, do que o tradicionalmente usado para os quadrotors, foi obtido.

Com o modelo completo dos veículos, foi realizada uma analise da dinâmica e de alcance dos veículos, variando a velocidade.

Por ultimo, mas não menos importante, foi proposta e testada uma estratégia de controlo capaz de lidar com as peculiaridades deste tipo de veículos.

Palavras-chave: Quadrotor Híbrido, Avião Híbrido, Modelação de Hélices, Modelação dinâmica e cinemática, Regulador Linear-Quadrático

Abstract

The past decade saw the boom of Vertical Take-Off and Landing (VTOL) vehicles, such as quadrotors, hexarotors, and similar. But in more recent years there has been growing interest in vehicles that can take off vertically, and capable of flying like an airplane, to overcome some of the limitations of multirotors.

This work aims at providing a preliminary analysis of these types of vehicles, to assess their advantages and disadvantages.

First, two different approaches to these types of vehicles were selected, to provide a wider view of what can be accomplished. And for those vehicles, an extensive dynamic and kinematic model was obtained. Due to the specific working conditions of these vehicles, a more advanced model for the propellers than the traditionally used for quadrotors was obtained.

With the complete model for the vehicles, an analysis on the vehicles dynamics and range, for varying airspeed was performed.

Finally, a control strategy capable of dealing with the peculiarities of these vehicles was proposed and tested.

Keywords: Hybrid Quadrotor, Hybrid Plane, Propeller modeling, Dynamic and Kinematic modeling, Linear-Quadratic Regulator

Contents

List of Tables

List of Figures

Nomenclature

Acronyms

LQR	Linear Quadratic Regulator
UAV	Unmanned Aerial Vehicle
$VTOL$	Vertical Take-Off and Landing

Greek symbols

α	Angle of attack
β	Propeller lateral incidence angle
δ	Control surface angle
δ^c	Control surface input
$\boldsymbol{\eta}$	Vehicle orientation
λ	Inflow coefficient
μ_x	Dimensionless axial airspeed
μ_y	Dimensionless lateral airspeed
$\boldsymbol{\omega}$	Vehicle angular speed
Ω	Propeller angular speed
ψ	Propeller azymuthal coordinate
ρ	Air Density
θ_0	Initial blade angle
θ_{tw}	Blade twisting rate
ξ	Propeller axial incidence angle
ζ	Wing inclination

Roman symbols

$\boldsymbol{A_{ss}}$	State matrix
A	Wing surface area
$\boldsymbol{B_{ss}}$	Input matrix
B_m	Motor friction constant
C_D	Drag coefficient
$C_{D\alpha}$	Drag form coefficient
C_L	Lift coefficient
C_M	Pitching Moment coefficient
C_P	Power Coefficient
c_p	Propeller blade cord
C_T	Thrust Coefficient
c_w	Wing cord
C_{D_0}	Static drag coefficient
C_{L_α}	Lift form coefficient
C_{L_Δ}	Lift offset coefficient
C_{L_M}	Maximum lift coefficient
$\boldsymbol{e}$	Reference error
e_F	Propeller model error function
$\boldsymbol{F_a}$	Aerodynamic forces
$\boldsymbol{F_p}$	Propulsion forces
$\boldsymbol{g}$	Gravity acceleration
I	Motor current
i_w	Wing incidence angle
$\boldsymbol{J_v}$	Vehicle Inertia
J	Advance ratio
K_δ	Control surface constant
K_e	Counter-electromotive force constant
K_t	Torque constant

k_x	Inflow unbalance coefficient
U	Air speed
$\boldsymbol{M_a}$	Aerodynamic moments
$\boldsymbol{M_p}$	Propulsion moments
M_y	Propeller moment around y
M_z	Propeller moment around z
N_b	Number of blades
$\boldsymbol{p}$	Vehicle Position
P	Power
Q	Torque
$\boldsymbol{R_a^b}$	Rotation matrix from 'a' to 'b'
R_0	Base reference frame (NED)
R_b	Body reference frame
R_f	Aerodynamic forces reference frame
R_i	Propeller blade inner radius
r_i	Dimensionless propeller blade inner radius
R_m	Motor resistance
R_p	Propeller radius
R_w	Wing reference frame
T	Thrust
$\boldsymbol{u}$	Input vector
$\boldsymbol{V_b}$	Vehicle speed
$\boldsymbol{V_{ef}}$	Wing effective airspeed
V_m	Motor voltage
v_m	Dimensionless motor input
$\|X\|$	Absolute value of X
$\boldsymbol{x}$	State vector

Subscripts

b Body reference frame

f Aerodynamic forces reference frame

w Wing reference frame

x, y, z Cartesian components

Superscripts

T Transpose.

Chapter 1

Introduction

The present work intends to model, simulate, and control two hybrids between quadrotors and fixed-wing aircrafts, as an alternative to those two types of vehicles.

Due to the wider range of conditions those vehicles are subjected to, a more comprehensive analysis of its components is necessary, along with other aproaches for control strategies.

1.1 Motivation

Quadrotors and unmanned airplanes are both widely used nowadays. Quadrotors for tasks such as recording events from the air or high voltage poles inspection. And unmanned airplanes for long range surveillance, or transport. But still, there are scenarios where none of those vehicles fit the needs.

To fill that space, hybrid vehicles are looked at, to overcome some of the limitations of both types of vehicles. A quadrotor can take off and land nearly anywhere, but has a very limited range. An airplane has a large range, but needs a runway to take off and landing.

One of the scenarios considered is delivering parcels. The vehicle needs to be able to land in a limited space do deliver the package, but also needs range to be able to deliver those packages at long distances.

Other of the cases considered is maritime surveillance, to enable the launch of these vehicles from small water crafts. Quadrotors do not possess the range to significantly increase the surveillance area, nor the speed to keep up with other watercrafts. An unmanned airplane would have to be launched from the ground, possibly far from the location of the boat, wasting some of the range of the aircraft. A hybrid vehicle would allow for a large increase in surveillance area, and fast deployment from the watercraft location in case of need.

1.2 Historical Introduction

The last century saw the boom in airplane and helicopter development, and, as those types of vehicles matured, interest in vehicles that combine attributes from both started to grow.

The military was the main precursor of those early designs (fig 1.1), nowadays civilian applications are increasingly the focus of development (fig 1.2).

(a) Bell, XV-3 [1] (b) Bell-Boeing, V-22 Osprey [2] (c) EWR, VJ 101 [3] (d) Lockheed Martin, F-35B [4]

Figure 1.1: Military hybrid aircrafts

In the past decade, big advancements in electronic miniaturisation, improvements in battery specific power, and more efficient motors, created that same boom on small unmanned aerial vehicles.

(a) Joby, S2 concept [5] (b) Lilium Aviation concept [6] (c) AgustaWestland AW609 [7]

Figure 1.2: Civilian hybrid aircrafts

There has been a massification of small helicopter-like vehicles (multirotors) and small airplanes (fig 1.3), specially for the consumer market given their low cost.

(a) DJI, Phantom 4 [8] (b) Parrot, Bebop 2 [9] (c) UAVision, Wingo [10]

Figure 1.3: Unmanned Aerial Vehicles

More recently, there has been increased interest in hybrid designs from the most varied areas, in order to overcome the limitations of each one and add versatility, allowing for new use cases. Some of these hybrid designs take inspiration from those precursors, others implementing new approaches.

Amazon is developing Unmanned Aerial Vehicles (UAVs) to deliver packages, Prime Air service. Their latest vehicle is a hybrid VTOL UAV (fig 1.4), with 8 rotors for takeoff and landing. For long range flight a 9th rotor on the back for propulsion, wings for lift, and control surfaces for flight control. This allows it to deliver an order directly to the customer backyard, at longer distances.

Arcturus UAV has a series of vehicles following the same approach, such as the JUMP 15, but only 4 rotors instead of 8 for takeoff and landing. And Textron Systems prototype Aerosonde, to be used for

reconnaissance, surveillance and as a communications platform.

(a) Amazon, Prime Air [11] (b) Arcturus UAV, Jump 15 [12] (c) Textron Systems, Aerosonde [13]

Figure 1.4: Hybrid UAVs (Amazon, Arcturus UAV, Textron Systems)

Their design and control is fairly straightforward, they are very similar to current UAVs, like the Wingo, but with the addition of vertical rotors.

On the other hand, NASA's GL-10 Greased Lightning takes inspiration from those larger hybrids. Instead of having independent rotors for the 2 scenarios, the entire wing (with the rotors attached) rotates in relation to the fuselage.

On the Kari TR60 only the rotors rotate. Intend for reconnaissance and surveillance, can carry large payloads and multiple sensors.

(a) NASA, GL-10 Greased Lightning [14] (b) Kari, TR60 [15]

Figure 1.5: Hybrid UAVs (NASA, Kari)

There are models that stray even further away from those simpler designs. The Quadshot was the first from Transition Robotics, in what looks like a wing with 4 rotors. The entire aircraft changes orientation depending on the scenario, making the control more difficult, but reduces the need of independent rotors for each use or having moving "structures". Reduces structural complexity, weight, and cost. Can have a camera mounted, or other small sensors. Their more recent project, the JumpShip, has a biplane-like airframe, but follows the same operating principle, and capable of carrying multiple sensors or a package up to 5Kg.

The Wingtra 1, unlike these, uses control surfaces, and thus only requiring 2 rotors. Can be equipped with a camera or other small sensors.

1.3 State of the art

Over the past few years there has been a growing academic interest in quadrotor fixed wing hybrid vehicles. Increased research in the characteristics from each vehicle type to merge, development

(a) Transition Robotics, Quadshot [16] (b) Transition Robotics, Jumpship [17] (c) Wingtra, Wingtra 1 [18]

Figure 1.6: Hybrid UAVs (Transition Robotics, Wingtra)

of models to accurately represent those vehicles in their working conditions, and control strategies to provide a stable flight.

Many approaches have been proposed, William J. Fredericks *et al.* [19], at the NASA Langley Research Center, performed an analysis of 4 different vehicles (fig. 1.7), to assess their feasibility and expected performance.

One of those variants, the Greased Lightning, has been further developed, passing through various prototypes, with one being the GL-10 prototype (fig.1.5(a)). That prototype is studied by Paul M. Rothhaar *et al.* in [20]. First testing the vehicle aerodynamics using Computational Fluid Dynamics, and later in a wind tunnel. A total of 3 different propellers were also tested in the wind tunnel, to assess the effects of the angle of attack, and to obtain an equivalent model [21].

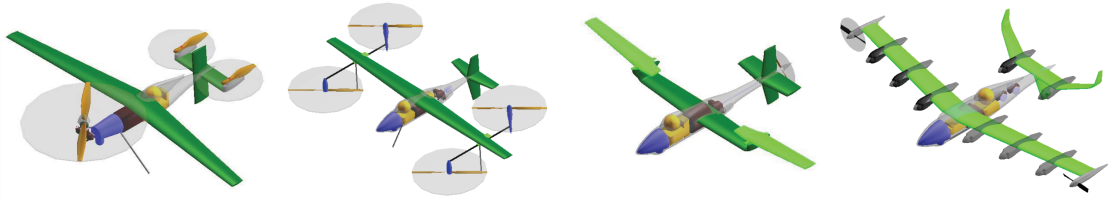

(a) Trifecta (b) Split Wing (c) Dos Samara (d) Greased Lightning

Figure 1.7: Hybrid vehicle concepts

The SUAVI was a vehicle developed and constructed by E. Cetinsoy *et al.* [22]. Composed of 2 wings, capable of rotating relative to its fuselage, with each wing divided in 2 sections with one propeller each. The entire dynamical model is presented, with the dynamics described using Newton-Euler, and the formulation for the propellers considering constant thrust and power coefficients. For its control a hierarchical control system is implemented, the high level controller is responsible for generating the trajectories, and low level controllers for the different flight modes, to transform those trajectories into actions in the actuators.

In [23] a similar controller for the Quadshot (fig. 1.8) is proposed. An outer loop takes the state variables and desired position and generates a series of waypoints to follow. An inner controller calculates the necessary thrust and orientation. The model considered for the Quadshot is a concise representation of its dynamics, without entering into the detail of the actuators and wing.

The MAVion (fig. 1.9) is in development at the Institut Supérieur de l'Aéronautique et de l'Espace since 2009, intended to be a vehicle capable of operating in complex urban environments, both outdoor

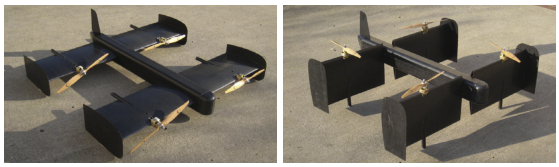

(a) Forward flight configuration (b) Axial flight configuration

Figure 1.8: Sabanci University Unmanned Aerial Vehicle

and indoor.

Yann Ameho, in his PhD thesis [24], presents a very detailed model for the vehicle dynamics. For the propellers a model was obtained using Blade Element Theory that includes some of the effects of the external airflow and blade flapping. The vehicle propellers are directly in front of the wings, the interaction between the airflow at the propeller exit and the wing is also accounted for, with the aerodynamic coefficients approximated with sinusoidal functions. The control was assured using Adaptive Control.

Later, in [25], a different model is proposed and validated with experimental data, for the case of forward flight. The control strategy consists in linearizing the system for 10 fixed points in Axial flight, transition and Forward flight, and using an external controller to transition between them.

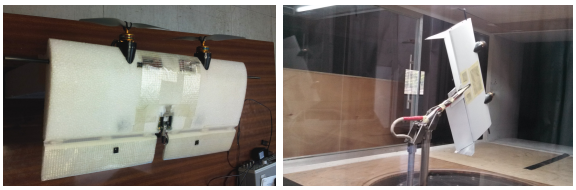

(a) MAVion structure (b) Wind tunnel test

Figure 1.9: MAVion

In [26] another type of vehicle is proposed, one where only the propellers rotate to transition from Axial flight to Forward flight (fig. 1.10). A model for the propellers is derived based on the Blade Element Theory. For the wings linear and quadratic approximations for the lift and drag coefficients were considered, as they will not be subject to large angles of attack. To control the vehicle, 2 controllers are obtained, switching between them depending on the propellers tilt.

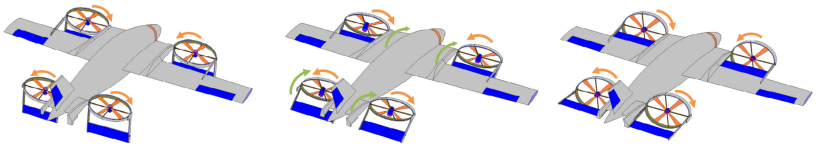

(a) Axial flight configuration (b) Transition (c) Forward flight configuration

Figure 1.10: Tilt-rotor aircraft

At KU Leuven, Menno Hochstenbach *et al.* [27], designed a hybrid similar to the Quadshot, the VertiKUL. It was developed to be capable of transporting packages up to 1Kg. Designed with the minimum moving parts possible, to keep the costs down, reduce the chance of failure and maintenance. It takes

off with the wing oriented vertically, and transitions to airplane-like flight by rotating the entire vehicle (fig. 1.11). Two control modes were implemented, a low level and a mid level modes. In the low level, using the RF remote transmitter, the pilot commands directly the collective thrust and the vehicle angular speeds. Using the mid level control mode is uses a separate controller for Axial flight and for Forward flight. The transition between modes is activated by a switch, and it is performed autonomously by a third controller.

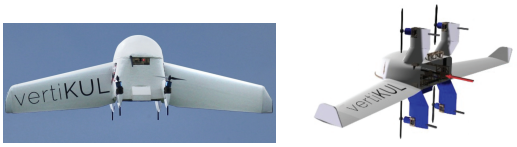

(a) Axial flight configuration (b) Forward flight configuration

Figure 1.11: VertiKUL

1.4 Objectives

One of the main objectives of this work is to obtain a model that describes comprehensibly the dynamics of these types of vehicles, taking into account that the wings in these vehicles will be subject to high angles of attack, and that the propellers will be subject to high incidence angles and lateral and axial external air flows.

It is also intented to carry out a preliminary analysis of the vehicles range with different propeller, for varying airspeed to assess their potential compared to quadrotors and fixed wing aircrafts.

And last, implement a control strategy capable of controlling these vehicles throughout their varying working conditions and attitudes.

1.5 Thesis Outline

In chapter 1 the motivation that led to this work, an historical introduction to hybrid vehicles, and some of the most recent research in the area are presented. The objectives for this work are also presented.

In chapter 2 the dynamic and kinematic modeling for these vehicles, detailing the model used for the propellers, wings and motor.

Chapter 3 details the procedure used to obtain the model for the propellers. The various approximations considered and comparison of the result between them, and the final choice of model to be used.

Chapter 4 presents an analysis on the vehicles range and attitude for varying air speed, with different propellers. From those results, are chosen the most adequate propeller for the vehicles.

The control strategy obtained is presented in chapter 5, along with the results in the presence of disturbances, and for a complete flight.

In chapter 6 the final conclusions of this work, the contributions made by this work to the area, and suggestions for future work are presented .

Chapter 2

Vehicle models

In this work, 2 different vehicles are modeled in order to test different approaches to the problem at hand.

The first one, which will be addressed as Hybrid Quadrotor, can be considered more unconventional. Although it has some similarities with a conventional quadrotor when it comes to the propulsion system, the structure and operating mode are very different and unique.

The second one, called Hybrid Plane, could be considered as a more traditional approach. It can be characterised mainly as a traditional airplane, but with the addition of 4 propellers responsible for the vertical take off and landing, like a quadrotor.

The dimensions and other specifications, of both vehicles, are presented in table A.1 and A.2.

2.1 Vehicle definition

Hybrid Quadrotor

Starting with the Hybrid Quadrotor, its body is composed mainly of a wing (fig 2.1), and the battery and electronics are housed inside it. For propulsion it has 4 brushless motors and 4 propellers.

At low speeds the vehicle will move like a traditional quadrotor. For higher speeds, the vehicle will tilt and use the wing to provide lift, and thus increasing power efficiency.

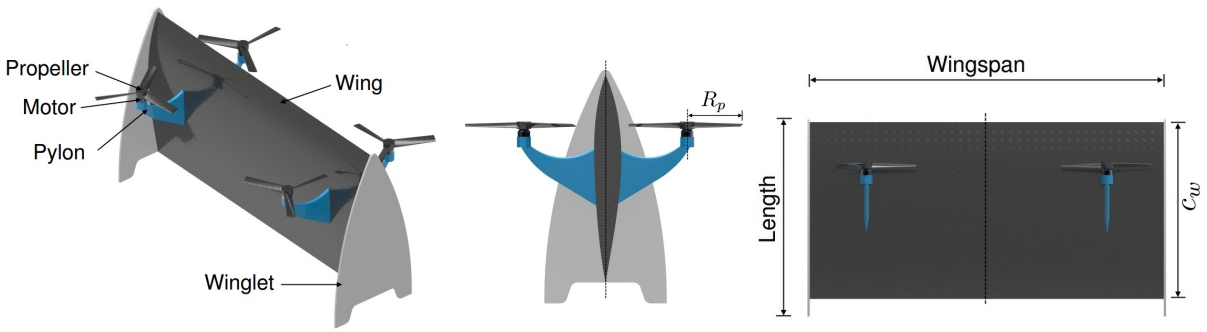

(a) Isometric view (b) Side view (c) Front view

Figure 2.1: Hybrid Quadrotor

These 2 flight modes will be addressed as Axial flight and Forward flight respectively, and are illustrated in figure 2.2

- **Axial flight:** for take off, landing, other operations that may require the vehicle to move at low airspeed, or even stationary. The thrust generated by the propellers is responsible to keeping the vehicle in the air and to move in any given direction. The movement is controlled just like a standard quadrotor, by providing differential thrust with the propellers in order to produce torque and move the vehicle as desired.

- **Forward flight:** for a higher airspeed flight. The lift generated by the wing is responsible, for the most part, for keeping the vehicle in the air, and the thrust generated by the propeller to keep the vehicle moving forward. Although the wing could include a pair of ailerons, it is assumed here that no control surfaces are available, neither ailerons, elevators nor rudder like in a conventional airplane. Instead differential thrust is also used to control the direction of flight .

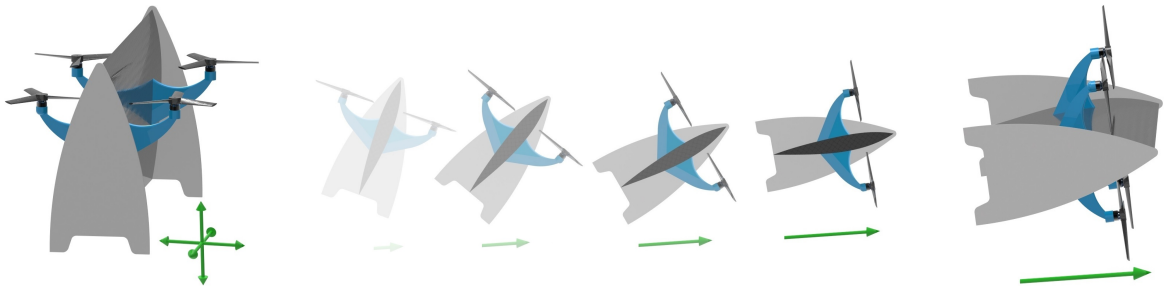

(a) Axial flight (b) Transition (c) Forward flight

Figure 2.2: Flight modes and transition

In the transition between Axial flight and Forward flight, the vehicle will start moving forward, by leaning in that direction. As it gains speed the wing generates increasingly more lift and the vehicle can be rotated further, until is reaches the Forward flight attitude.

Oppositely, to transition from Forward flight to Axial flight, it will start to decelerate and tilt backwards until reaching Axial flight position.

Regarding the differential thrust control, an illustration of the various possible combinations for thrust, common for both Axial flight and Forward flight can be seen in figure 2.3. But depending on the flight mode they will correspond to slightly different actions, detailed in table 2.1

As for an usual quadrotor, the propellers are not equal, one pair produces thrust when rotating clockwise, and the other pair when rotating counterclockwise. With the propellers distributed alternately as shown in the figure 2.3, when performing any of the movements from $a)$ to $g)$, or any combination of them, the resulting torque in the propeller axis will be null. And with $h)$ and $i)$ the opposite, it is intended to maximise the torque along that axis.

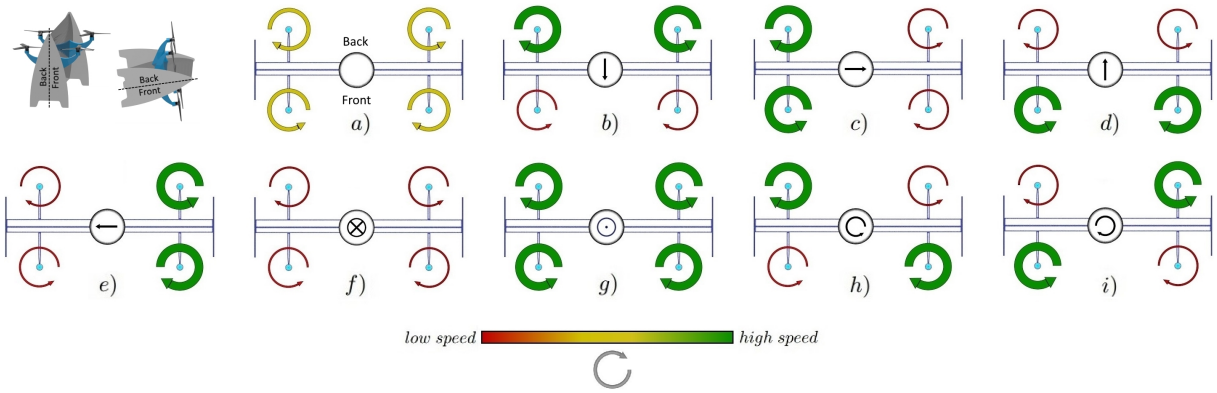

Figure 2.3: Flight movements

Axial flight	fig 2.3	**Forward flight**
hover	$a)$	cruise speed flight
tilt forward	$b)$	pitch down
tilt left	$c)$	yaw left
tilt backwards	$d)$	pitch up
tilt right	$e)$	yaw right
move down	$f)$	decrease speed
move up	$g)$	increase speed
rotate counterclockwise	$h)$	negative roll
rotate clockwise	$i)$	positive roll

Table 2.1: Flight movements description

Hybrid Plane

Moving on to the Hybrid Plane, it is very similar to a fixed-wing aircraft, more specifically a twin-boom aircraft. A large wing to provide lift, on the back an aerodynamic structure that acts as both vertical and horizontal stabiliser, the fuselage, and two booms connecting the back structure to the wing. On the back of the fuselage, a rotor for propulsion, and the battery and electronics are housed inside the fuselage.

However, it contains 4 extra rotors, with their axis of rotation normal to the ground, which will be used for take off and landing, meaning it can take off vertically without the need of a runway. And the booms not only connect the back structure to the wing but also work as support for the extra rotors, by extending beyond the wing (fig 2.4).

The aircraft possess two ailerons on the wing, and two other surfaces on the back that act as elevator and rudder, depending on their combination. To pitch the vehicle both surfaces on the back are actuated in the same direction, for yaw they are actuated in opposite directions. To actuate them servo motors would be used, however those motors will not be modelled, their action will considered as nearly instantaneous.

The wing is not aligned with the axis of the back rotor, it has an incidence angle i_w, in such a way that when in Forward flight, at cruise speed, the back propeller can be aligned with relative air speed while the wing is at angle of attack equal to i_w. This could also be achieved by using a wing with lift coefficient grater than zero for an angle of attack equal to zero. The aerodynamic structure on the back is aligned

with the axis of rotation of the back rotor, but not aligned with the main wing lateral direction, they have an inclination of ζ.

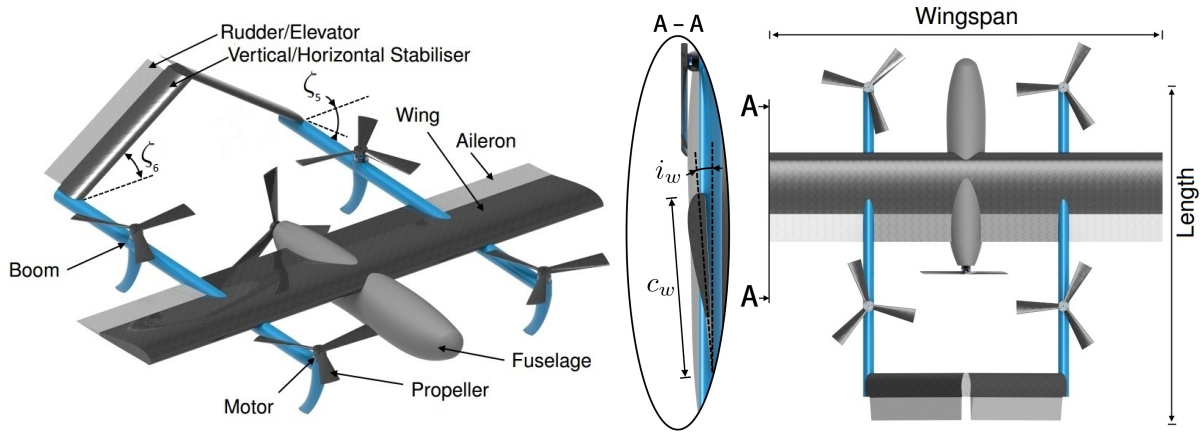

(a) Isometric view (b) Wing (c) Top view

Figure 2.4: Hybrid Plane

Similarly to the Hybrid Quadrotor, it has 2 flight modes (fig 2.5).

- **Axial flight:** for take off, landing or other operations that may require the vehicle to move at low airspeed, or even stationary. The 4 extra propellers provide the thrust for lift and movement, the motor in the back of the fuselage is turned off in most situations. The movement is controlled by providing differential thrust to each propeller, just like for a basic quadrotor.
- **Forward flight:** for higher airspeed flight and longer distances. The back propeller provides thrust for movement, and the wing provides the lift. The direction of movement is governed by the control surfaces.

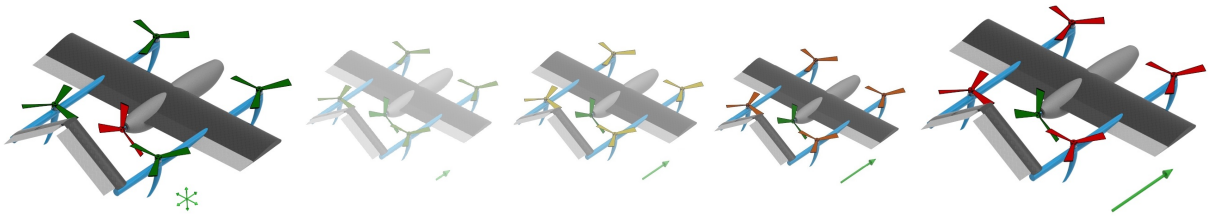

(a) Axial flight (b) Transition (c) Forward flight

Figure 2.5: Flight modes and transition

To transition from Axial flight to Forward flight the back motor is turned on, moving the vehicle forward. As it gains speed and the wing generates lift, the 4 propellers reduce their speed, until the wing generates enough lift and they can be completely turned off. From Forward flight to Axial flight, the back motor is turned off to reduce speed, and the 4 rotors engaged to compensate for the reduction of lift from the wing.

The thrust control for Axial flight in this vehicle is the same as the Hybrid Quadrotor, presented previously in figure 2.3. For Forward flight, the possible configurations can be seen on figure 2.6, and a description of both in table 2.2.

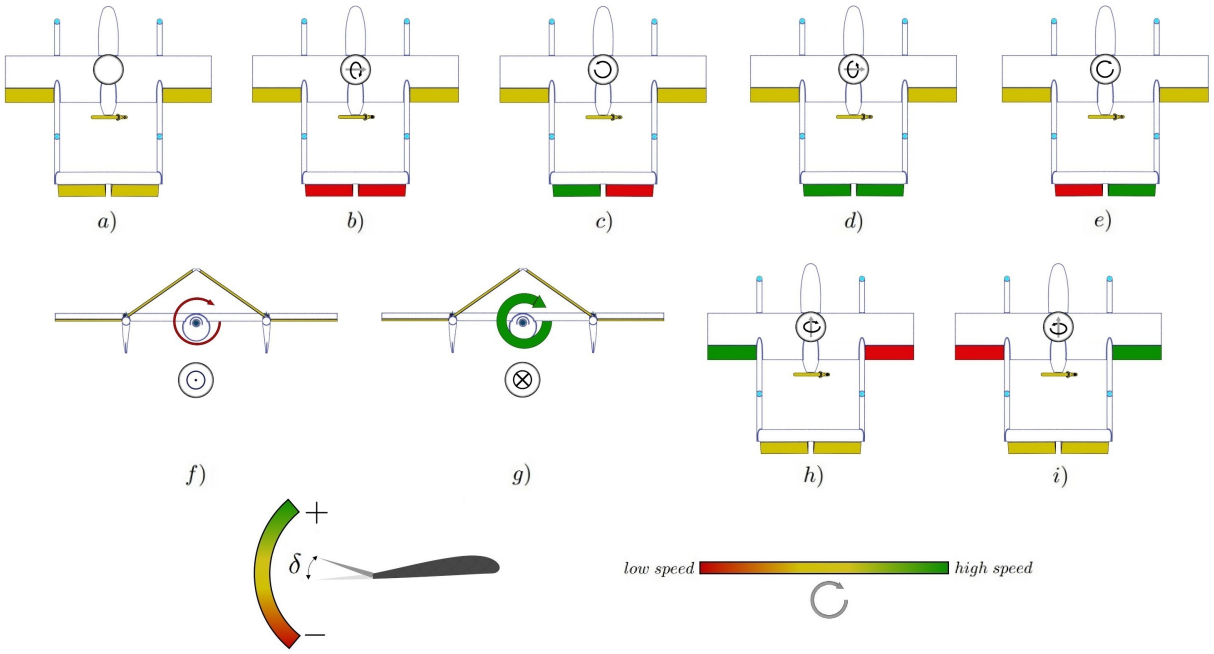

Figure 2.6: Flight movements

Axial flight	fig 2.3	fig 2.6	**Forward flight**
hover	$a)$	$a)$	average speed flight
tilt forward	$b)$	$b)$	pitch down
tilt left	$c)$	$c)$	yaw left
tilt backwards	$d)$	$d)$	pitch up
tilt right	$e)$	$e)$	yaw right
move down	$f)$	$f)$	decrease speed
move up	$g)$	$g)$	increase speed
rotate counterclockwise	$h)$	$h)$	negative roll
rotate clockwise	$i)$	$i)$	positive roll

Table 2.2: Flight movements description

Given the propeller configuration, it is possible to perform 2 other operations not mentioned above. In the case of moving forward in Axial flight, instead of providing differential thrust with the 4 propellers, the back propeller can also be engaged. And when transitioning from Forward flight to Axial flight, the 4 vertical propellers can also be used for a quicker deceleration, by slightly tilting the vehicle backwards.

2.2 Reference Frames

The base reference frame R_0 is defined as NED (North, East, Down), it is fixed on the ground and can be considered approximately inertial if the Earth rotation is disregard.

Three reference frames will be defined for each vehicle, identified as Body frame (R_b), Wing frame (R_w) and Aerodynamic Forces frame (R_f). The coordinate transformation between reference frames can by given by a rotation, represented using Euler angles or unit quaternions. Given the wide range of orientations the Hybrid Quadrotor can attain, unit quaternions is a more adequate choice as it gives us a unique representation, eliminating the problem of singularities present in the Euler angles representa-

tion.

The rotation matrix from reference frame R_b to reference frame R_0 will be identified as R_b^0. And in a similar fashion for the rotation matrices between other reference frames.

In terms of notation, the lower subscript will indicate in what frame a vector is considered. In the case of the base reference frame, the subscript is omitted. The component of a vector, by indicating it in the lower subscript after the reference frame.

- $\boldsymbol{F_g}$ = Gravity force vector in the base reference frame
- $\boldsymbol{F_{g_b}}$ = Gravity force vector in the body frame
- $\boldsymbol{F_{g_w}}$ = Gravity force vector in the wing frame
- $\boldsymbol{F_{g_{w,x}}}$ = Component x_w of the gravity force vector, in the wing frame.

Hybrid Quadrotor

The Body reference frame R_b for our first vehicle is defined with x_b aligned with the propeller axis of rotation, y_b aligned with the lateral direction of the wing, z_b normal to both, facing the front. The origin at the centre of gravity of the vehicle (fig. 2.7) .

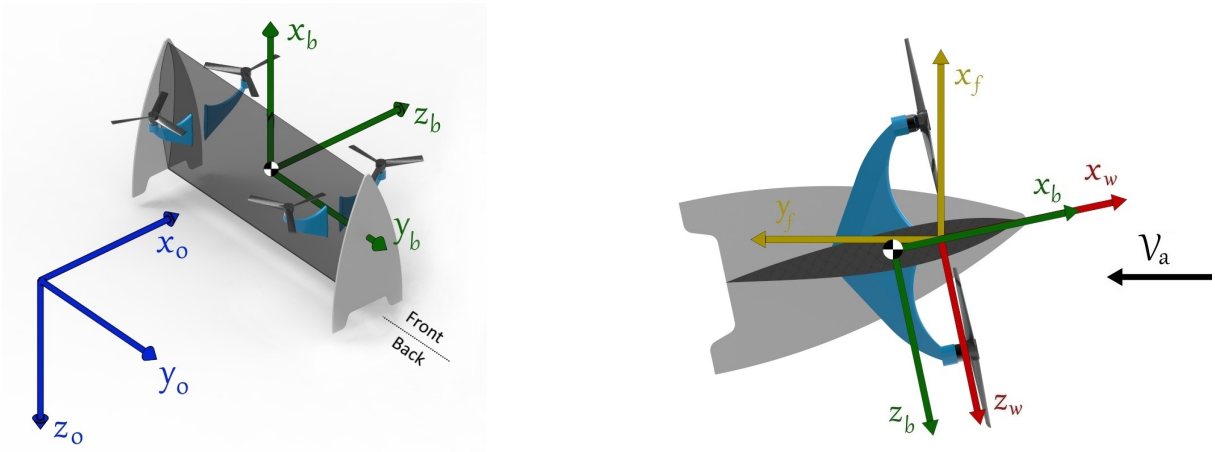

(a) Base and Body reference frames

(b) Wing and forces reference frames

Figure 2.7: Hybrid Quadrotor reference frames

The Wing reference frame R_w, with the origin at the wing aerodynamic centre, usually at 1/4 of the wing cord, and with its axes aligned with R_b.

And the third reference frame, R_f, with its origin also at the aerodynamic centre, x_f coincident with the Lift, y_f coincident with the Drag, and z_f oriented to complete the orthonormal frame.

Hybrid Plane

The body reference frame for the Hybrid Plane is defined with x_b aligned with the back propeller axis of rotation and booms, y_b along the wing lateral direction, z_b aligned with propellers vertical to the ground, and the origin at the centre of gravity (fig 2.8). The reference frame for the wing R_w, with the

origin at the wing aerodynamic centre. x_w and z_w rotated i_w in relation to x_b and z_b, and y_w aligned with y_b.

And R_f, with its origin at the wing aerodynamic centre, x_f coincident with the Lift, y_f coincident with Drag, and z_f to complete the orthonormal frame.

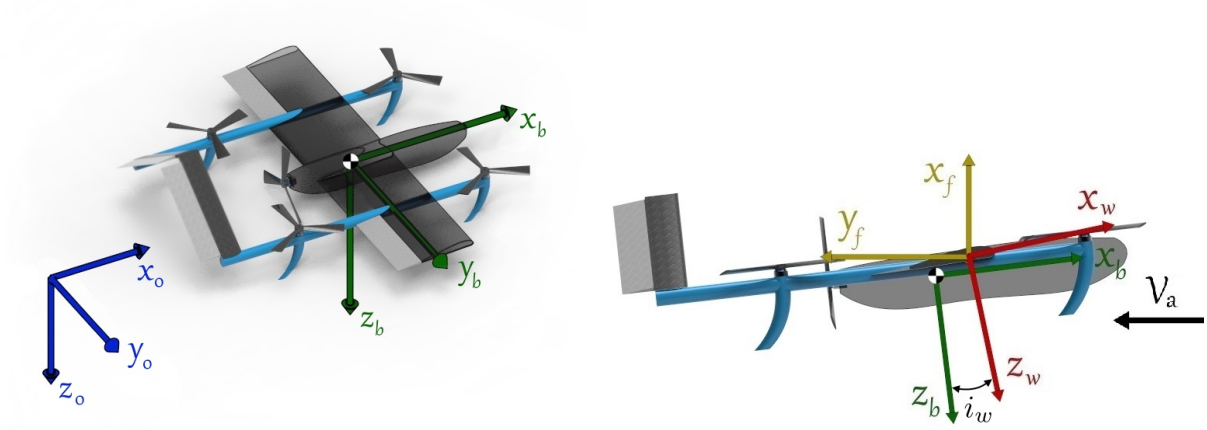

(a) Base and Body reference frames

(b) Wing and forces reference frames

Figure 2.8: Hybrid Plane reference frames

2.3 Vehicle Dynamics

The vehicle is subject to various forces, in this work the main ones will be addressed. These can be divided into 3 parts:

- Gravity: $\boldsymbol{F_g}$
- Propulsion system: $\boldsymbol{F_p}$, $\boldsymbol{M_p}$
- Aerodynamics: $\boldsymbol{F_a}$, $\boldsymbol{M_a}$

The vehicle dynamics, following a Newton-Euler approach [28], and assuming constant mass and inertia, may be expressed by the following equations :

$$\begin{aligned} m\dot{\boldsymbol{V}}_b &= -\boldsymbol{\omega}_b \times m\boldsymbol{V}_b + \boldsymbol{F}_{g_b} + \boldsymbol{F}_{p_b} + \boldsymbol{F}_{a_b} \\ \boldsymbol{J}_v\dot{\boldsymbol{\omega}}_b &= -\boldsymbol{\omega}_b \times \boldsymbol{J}_v\boldsymbol{\omega}_b + \boldsymbol{M}_{p_b} + \boldsymbol{M}_{a_b} \end{aligned} \tag{2.1}$$

where $\boldsymbol{V_b}$ is the vehicle linear speed, $\boldsymbol{\omega_b}$ the angular speed, and $\boldsymbol{J_v}$ the vehicle inertia matrix . $\boldsymbol{F_{g_b}}$ is the gravity force vector, $\boldsymbol{F_{p_b}}$ and $\boldsymbol{M_{p_b}}$ will be respectively the vectors of forces and moments generated by the propulsion system. And from the aerodynamics, $\boldsymbol{F_{a_b}}$ and $\boldsymbol{M_{a_b}}$ are the vectors of forces and moments from the aerodynamic interactions.

2.4 Vehicle Kinematics

As for the kinematic equations for our vehicle, they are given by:

$$\begin{aligned} \dot{\boldsymbol{p}} &= \boldsymbol{R}_{\boldsymbol{b}}^{\boldsymbol{0}} \boldsymbol{V}_{\boldsymbol{b}} \\ \dot{\boldsymbol{\eta}} &= -\frac{1}{2} \begin{bmatrix} 0 & \omega_{b,x} & \omega_{b,y} & \omega_{b,z} \\ -\omega_{b,x} & 0 & -\omega_{b,z} & \omega_{b,y} \\ -\omega_{b,y} & \omega_{b,z} & 0 & -\omega_{b,x} \\ -\omega_{b,z} & -\omega_{b,y} & \omega_{b,x} & 0 \end{bmatrix} \boldsymbol{\eta} \end{aligned} \tag{2.2}$$

With $\boldsymbol{p}$ the position vector in the base reference frame, and $\boldsymbol{\eta}$ the vehicle orientation relative to the base reference frame, expressed in unit quaternions.

2.5 Gravity

The gravity force vector in the body frame is simply given by :

$$\boldsymbol{F}_{\boldsymbol{g_b}} = \boldsymbol{R}_{\boldsymbol{0}}^{\boldsymbol{b}}\, m\, \boldsymbol{g}$$

where m is the vehicle mass, and $\boldsymbol{g}$ is the local earth gravity acceleration expressed in the base reference frame.

2.6 Propulsion

2.6.1 Propeller

Both vehicles will work in a variety scenarios, which will subject the propellers to very different working conditions. From external air speed purely axial to completely lateral, or no external air speed at all.

The simple models usually used do not account for these effects, and so a more comprehensive model is required. The formulation and analysis of the model obtained is presented in chapter 3, but a brief summary will be presented here.

Each propeller i rotates at angular speed Ω_i producing thrust T_i and torque Q_i. But given the presence of air flow in the lateral direction of the propeller, there will also be transverse moments M_{i_y} and M_{i_z}.

$$\begin{aligned} T_i &= \rho \pi {R_p}^2 (\Omega_i R_p)^2 C_T \\ Q_i &= \rho \pi {R_p}^3 (\Omega_i R_p)^2 C_P \\ \begin{bmatrix} M_{i_y} \\ M_{i_z} \end{bmatrix} &= \rho \pi {R_p}^3 (\Omega_i R_p)^2 \begin{bmatrix} cos(\beta) & -sin(\beta) \\ sin(\beta) & cos(\beta) \end{bmatrix} \begin{bmatrix} C_{M_y} \\ C_{M_z} \end{bmatrix} \end{aligned} \tag{2.3}$$

Where C_T is the thrust coefficient, C_P the power coefficient, and C_{M_x} and C_{M_y} moment coefficients.

In this formulation the moments obtained are oriented with the lateral air speed, and need to be rotated to the body reference frame. For the Hybrid Quadrotor and the back propeller of the Hybrid Plane, β is the angle between the incident lateral air flow and the axis y_b, obtained as $\beta = atan2\big(V_{a_{b,z}}, V_{a_{b,y}}\big)$. For the other 4 propellers of the Hybrid Plane, $\beta = atan2\big(V_{a_{b,x}}, V_{a_{b,y}}\big)$, where $atan2$ is the four quadrants arctangent function, available in Matlab™.

The thrust, power and moment coefficients are given as:

$$
\begin{aligned}
C_T = \frac{N_b c_p}{2\pi R_p}\Bigg(& 2C_{L_\alpha}\sqrt{C_{L_\Delta}}\Big[\theta_0\Big(\frac{1}{3}+\mu_y^2\frac{1-r_i}{2}\Big)+\theta_{tw}\Big(\frac{1}{4}+\mu_y^2\frac{1-r_i^2}{4}\Big)-\lambda\frac{1-r_i^2}{2}\Big] \\
&- C_{L_\alpha}^2\Big[\theta_0^2\Big(\frac{1}{3}+\mu_y^2\frac{1-r_i}{2}\Big)+\theta_{tw}^2\Big(\frac{1}{5}+\mu_y^2\frac{1}{6}\Big)+\theta_0\theta_{tw}\Big(\frac{1}{2}+\mu_y^2\frac{1-r_i^2}{2}\Big) \\
&+\lambda^2(1-r_i)-\lambda\theta_0(1-r_i^2)-\frac{2}{3}\lambda\theta_{tw}\Big]+(C_{L_M}-C_{L_\Delta})\Big(\frac{1}{3}+\mu_y^2\frac{1-r_i}{2}\Big)\Bigg) \\
C_P = \frac{N_b c_p}{2\pi R_p}\Bigg(& (C_{L_M}-C_{L_\Delta})\frac{\lambda}{3}-C_{L_\alpha}^2\lambda\Big[\theta_0^2\frac{1}{3}+\theta_{tw}^2\frac{1}{5}+\theta_0\theta_{tw}\frac{1}{2}-\lambda\theta_0-2\lambda\theta_{tw}\frac{1}{3} \\
&+\lambda^2\Big(\sqrt{1-\mu_y^2}-\sqrt{r_i^2}\Big)\Big]+C_{L_\alpha}\sqrt{C_{L_\Delta}}\lambda\Big[2\theta_0\frac{1}{3}+\theta_{tw}\frac{1-r_i^2}{2}-\lambda(1-r_i^2)\Big] \\
&+C_{D_\alpha}\Big[\theta_0^2\Big(\frac{1}{4}+\mu_y^2\frac{1-r_i^2}{4}\Big)+\theta_{tw}^2\Big(\frac{1}{6}+\mu_y^2\frac{1}{8}\Big)+\lambda^2\frac{1-r_i^2}{2}+ \\
&+\theta_0\theta_{tw}\Big(\frac{2}{5}+\mu_y^2\frac{1}{3}\Big)-2\lambda\Big(\theta_0\frac{1}{3}+\theta_{tw}\frac{1}{4}\Big)\Big]+C_{D_0}\Big[\frac{1}{4}+\mu_y\frac{1-r_i^2}{4}\Big]\Bigg) \\
C_{M_y} = \frac{N_b c_p}{2\pi R_p}\Bigg(& (C_{L_M}-C_{L_\Delta})\mu_y\frac{1}{3}+C_{L_\alpha}^2\Big[\lambda\theta_0\mu_y\frac{1-r_i^2}{2}-\theta_0^2\mu_y\frac{1}{3}+\lambda\theta_{tw}\mu_y\frac{1}{3} \\
&-\theta_0\theta_{tw}\mu_y\frac{1}{4}-\theta_{tw}^2\mu_y\frac{1}{5}\Big]-C_{L_\alpha}\sqrt{C_{L_\Delta}}\Big[\lambda\mu_y\frac{1-r_i^2}{2}-2\theta_0\mu_y\frac{1}{3}+\theta_{tw}\mu_y\frac{1}{4}\Big]\Bigg) \\
C_{M_z} = \frac{N_b c_p}{2\pi R_p}\Bigg(& C_{L_\alpha}\sqrt{C_{L_\Delta}}\lambda_0 k_x\frac{1}{4}+C_{L_\alpha}^2\Big[\lambda_0^2 k_x\frac{1}{3}-\lambda_0\theta_0 k_x\frac{1}{4}-\lambda_0\theta_{tw}k_x\frac{1}{5}+\lambda_0 k_x\mu_x\frac{1}{3}\Big]\Bigg)
\end{aligned}
\tag{2.4}
$$

As illustrated in figure 2.9, the blade has external radius R_p, inner radius R_i and constant chord c_p. With r_i the dimensionless inner radius, given as $\frac{R_i}{R_p}$. The blade is assumed to have a constant twisting rate, θ_{tw}, obtained as $\theta_{tw} = \frac{\theta_{R_p}-\theta_{R_i}}{R_p-R_i}$, and θ_0 would be the angle of the blade at the axis of the propeller, if R_i was equal to 0, and can be calculated as $\theta_0 = \theta_{R_i} - \theta_{tw}R_i$.

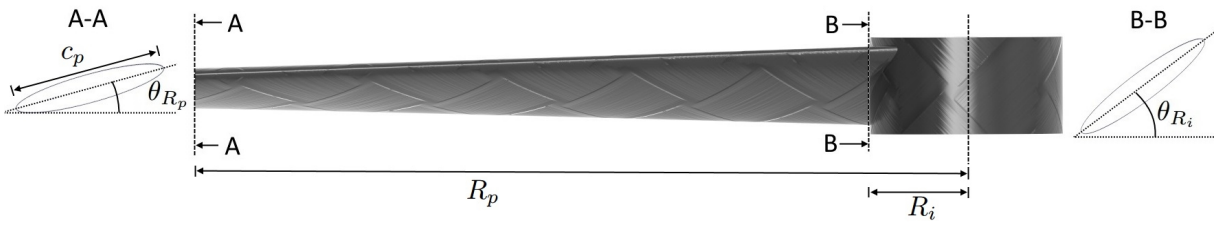

Figure 2.9: Propeller Blade twisting

The lift coefficient is approximated quadratically, in the form $C_L(\alpha) = C_{L_M} - (C_{L_\alpha}\alpha(R,\psi) - \sqrt{C_{L_\Delta}})^2$. C_{L_M} corresponds to the maximum value, $C_{L_M} - C_{L_\Delta}$ is the function value at α=0, and $2C_{L_\alpha}\sqrt{C_{L_\Delta}}$ is the slope at α=0. The drag coefficient is also approximated quadratically, as $C_D(\alpha) = C_{D_0} + C_{D_\alpha}\alpha^2(R,\psi)$, characterised with drag coefficient form C_{D_α}, and static drag coefficient C_{D_0}.

Both are illustrated in figure 2.10, using the data for the NACA 0012([29],[30]) as example of the approximation.

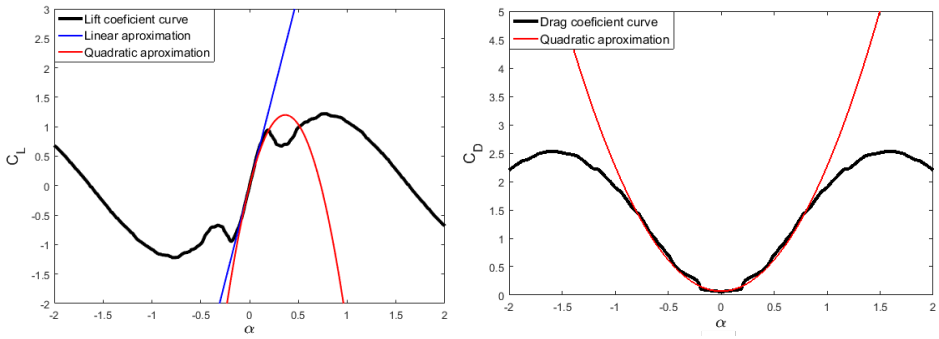

(a) Lift coefficient approximation (b) Drag coefficient approximation

Figure 2.10: Lift and Drag coefficients approximations

Relative to the air flow at the blades, μ_x is the dimensionless coefficient of the external axial flow, given as $\mu_x = \frac{V_{a_{b,x}}}{\Omega R_p}$, and μ_y is the dimensionless coefficient of the external lateral flow, given as $\mu_y = \frac{\sqrt{V_{a_{b,y}}^2 + V_{a_{b,z}}^2}}{\Omega R_p}$. The inflow [31] can be obtained as $\lambda_0 = \frac{C_T}{2\sqrt{\mu_y^2+\lambda^2}}$, and $\lambda = \mu_x + \lambda_0$. The variable k_x characterises the unbalance in the inflow, and is given as $k_x = tan(\frac{X}{2})$, with $X = tan^{-1}(\frac{\mu_y}{\mu_x+\lambda_0})$

Hybrid Quadrotor

As previously referred, the propulsion system is composed of 4 motor-propeller sets, in an X configuration. The numbering of the propellers and the respective directions of rotation are illustrated in figure 2.11.

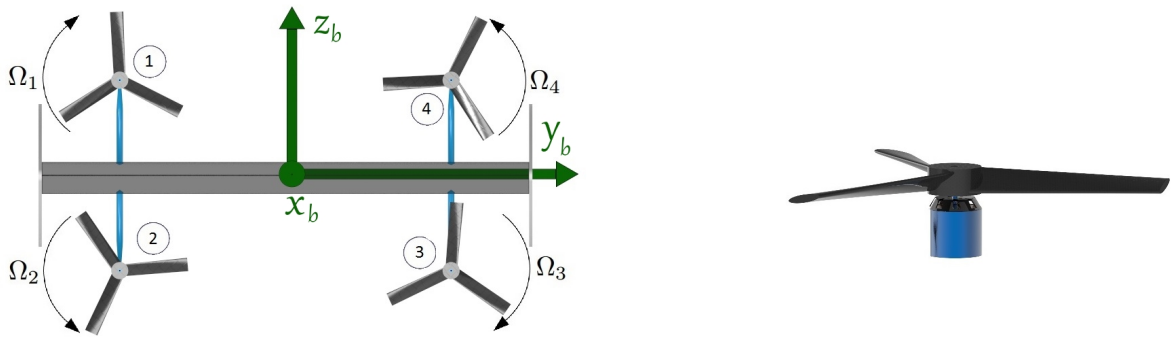

(a) Propeller configuration (b) Motor-propeller set

Figure 2.11: Hybrid Quadrotor Propulsion system

The resulting propulsion forces and moments are given by :

$$\boldsymbol{F_{p_b}} = \begin{bmatrix} \sum_{i=1}^{4} T_i \\ 0 \\ 0 \end{bmatrix} \qquad \boldsymbol{M_{p_b}} = \begin{bmatrix} -\sum_{i=1}^{4} Q_i(-1)^i \\ \sum_{i=1}^{4} T_i z_{i_b} - \sum_{i=1}^{4} M_{i_y}(-1)^i \\ -\sum_{i=1}^{4} T_i y_{i_b} - \sum_{i=1}^{4} M_{i_z} \end{bmatrix} \tag{2.5}$$

with z_{i_b} and y_{i_b} the propeller coordinates in the body reference frame.

Hybrid Plane

The Hybrid Plane has propulsion systems along 2 different axes. Four propellers, in an X configuration, aligned vertically in relation to the body, and a fifth propeller at the rear of the fuselage in a pusher configuration. The enumeration and directions of rotation are illustrated in figure 2.12.

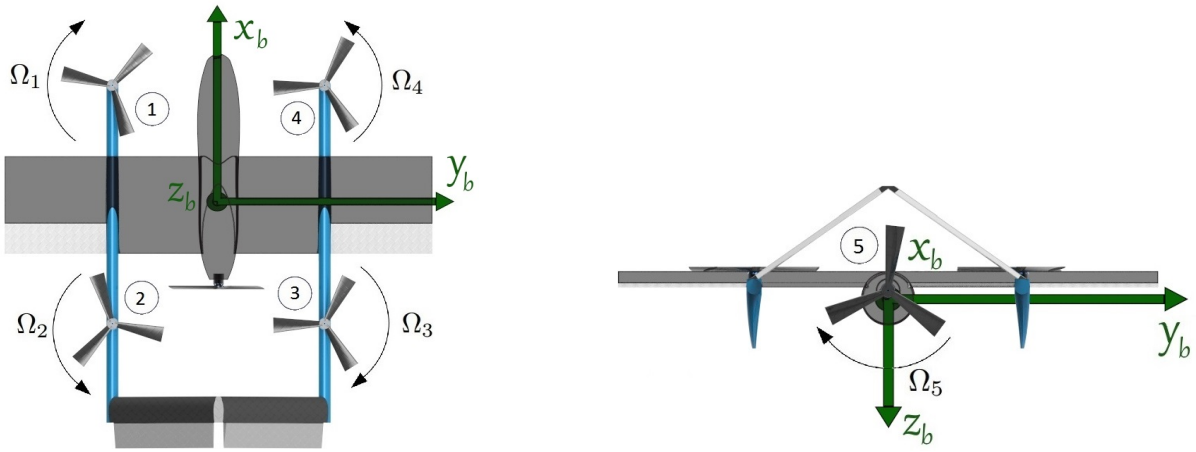

(a) Propeller configuration, top view

(b) Propeller configuration, back view

Figure 2.12: Hybrid Plane Propulsion system

These definitions result in the following force and moment vectors:

$$\boldsymbol{F_{p_b}} = \begin{bmatrix} T_5 \\ 0 \\ -\sum_{i=1}^{4} T_i \end{bmatrix} \quad , \quad \boldsymbol{M_{p_b}} = \begin{bmatrix} -\sum_{i=1}^{4} T_i y_{i_b} - Q_5 - \sum_{i=1}^{4} M_{i_x} \\ \sum_{i=1}^{4} T_i x_{i_b} + z_{5_b} T_5 - \sum_{i=1}^{4} M_{i_y}(-1)^i + M_{5_y} \\ \sum_{i=1}^{4} +y_{5_b} T_5 - M_{5_z} + Q_i(-1)^i \end{bmatrix} \tag{2.6}$$

2.6.2 Motor

This type of vehicles normally uses brushless DC motors, for their high efficiency and specific power. They will be modeled here as a simple DC motor, as follows [32]:

$$\begin{aligned}\frac{\mathrm{d}I_i}{\mathrm{d}t} &= \frac{V_{m_i} - R_m I_i - K_e \Omega_i}{L_m} \\ \frac{\mathrm{d}\Omega_i}{\mathrm{d}t} &= \frac{K_t I_i - Q_i - B_m \Omega_i}{J_m}\end{aligned} \tag{2.7}$$

where I_i is the current for each motor and V_{m_i} the control voltage. With the properties of the motor-propeller set as follows : circuit resistance R_m, circuit inductance L_m, counter-electromotive force constant K_e, rotor inertia J_m , torque constant K_t and friction constant B_m. These are illustrated in figure 2.13.

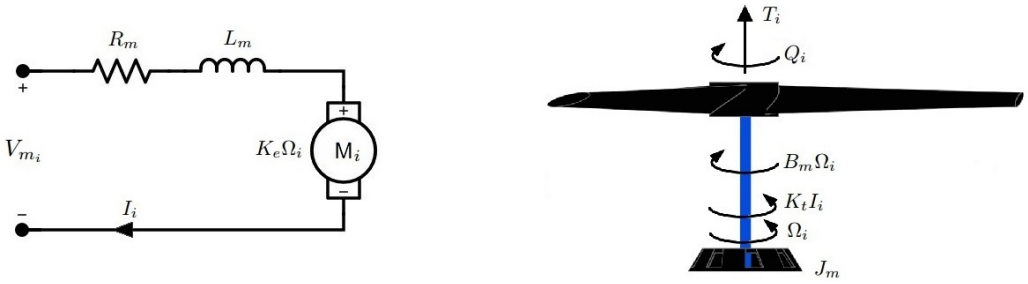

Figure 2.13: Motor equivalent circuit and physical characteristics

The servo motors considered to actuate the control surfaces in the Hybrid Plane will be considered as nearly instantaneous, and simply modeled as:

$$\frac{\mathrm{d}\delta_i}{\mathrm{d}t} = (\delta_i^c - \delta_i) K_\delta \tag{2.8}$$

with a high value of K_δ for a fast response. δ_i^c corresponds to the command input for each surface, and δ_i the surface deflection angle.

2.7 Aerodynamics

The aerodynamic forces and moments will be split in two terms, the wing ($\boldsymbol{F_{w_b}}$, $\boldsymbol{M_{w_b}}$) and the body ($\boldsymbol{F_{e_b}}$, $\boldsymbol{M_{e_b}}$).

$$\boldsymbol{F_{a_b}} = \boldsymbol{F_{w_b}} + \boldsymbol{F_{e_b}}$$
$$\boldsymbol{M_{a_b}} = \boldsymbol{M_{w_b}} + \boldsymbol{M_{e_b}}$$

2.7.1 Wing

For the wing the classical aerodynamic modelling will be considered, obtaining the lift and drag forces and the pitching moment at the aerodynamic centre (fig 2.14). The wing is considered as rigid, the effects of the airspeed along the span of the wing can be disregarded [31]:

$$L = \frac{1}{2}\rho V_a^2 A C_L(\alpha) \quad D = \frac{1}{2}\rho V_a^2 A C_D(\alpha) \quad M = \frac{1}{2}\rho V_a^2 A C_M(\alpha) \tag{2.9}$$

where A is the projected surface area, C_L and C_D the lift and drag coefficients, C_M the pitching moment

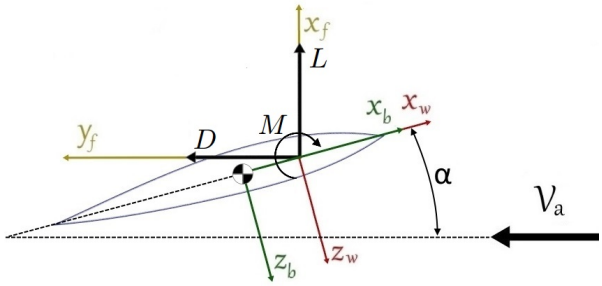

Figure 2.14: Aerodynamic forces and moment in the wing

coefficient, and α the angle of attack. But while in the propeller those coefficients could be considered as quadratic functions of α, the same is not possible here, as the angle of attack in the wing goes way beyond the range where those approximations are valid. In [29] and [30], lift, drag and pitching moment coefficient curves were obtained for some wing profiles. The results for the NACA 0012 airfoil were selected for the wings, and represented in figure 2.15.

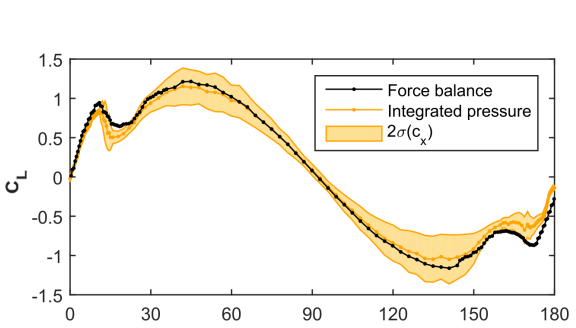

(a) Lift coefficient, [29]

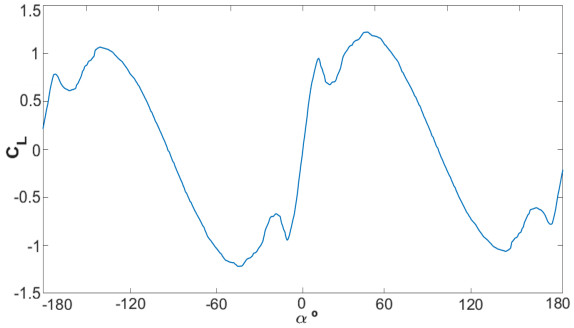

(b) Lift coefficient

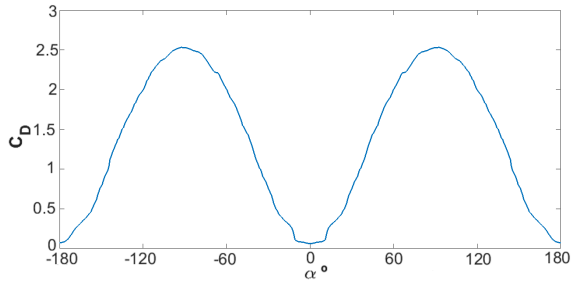

(c) Drag coefficient

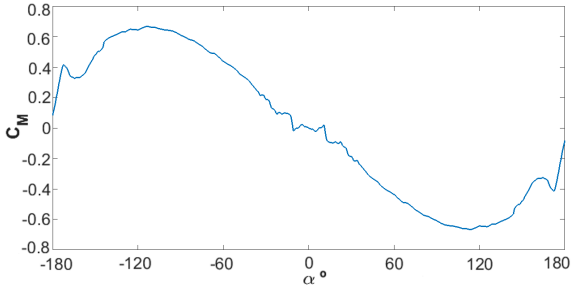

(d) Pitching Moment coefficient

Figure 2.15: NACA 0012 Lift, Drag and Pitching Moment

When the vehicle is rotating or turning, the effective air speed along the wing will vary, leading to variation in angle of attack, and in the corresponding aerodynamic forces generated. A way to consider the effects of the vehicle rotation is to break down the wing into sections. The effective air speed will be approximated as the speed at the aerodynamic centre of each section, α calculated from that speed, and A the projected surface area from each section.

Hybrid QuadRotor

The wing of the Hybrid Quadrotor is divided in 2 sections (fig. 2.16), as it is the minimum to take into account the vehicle rotation effects.

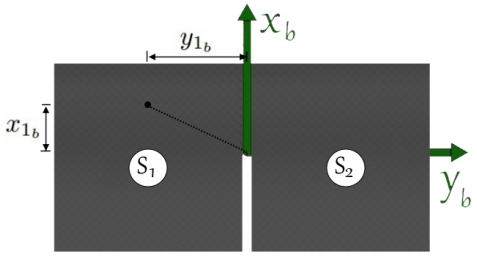

Figure 2.16: Wing sections

The effective airspeed in each surface S_i, in the body reference frame, $\boldsymbol{V_{ef,i_b}}$ is given as :

$$\boldsymbol{V_{ef,i_b}} = \boldsymbol{V_{a_b}} + \begin{bmatrix} 0 & z_{i_b} & -y_{i_b} \\ -z_{i_b} & 0 & x_{i_b} \\ y_{i_b} & -x_{i_b} & 0 \end{bmatrix} \boldsymbol{\omega_b} \tag{2.10}$$

The angle of attack given as $\alpha_i = atan2(V_{ef,i_{b,z}}, V_{ef,i_{b,x}})$, and the air speed as $V_{a,i} = \sqrt{{V_{ef,i_{b,x}}}^2 + {V_{ef,i_{b,z}}}^2}$. Replacing 2.9 we obtain :

$$L_i = \frac{1}{2}\rho V_{a,i}^2 A_i C_L(\alpha_i) \quad , \quad D_i = \frac{1}{2}\rho V_{a,i}^2 A_i C_D(\alpha_i) \quad , \quad M_i = \frac{1}{2}\rho V_{a,i}^2 A_i C_M(\alpha_i) \tag{2.11}$$

The air speed considered for each section is different, and the angle of attack will also be different for each surface, and the rotation matrix from the reference frame R_f to R_b. The resulting forces for each surface, in the body frame, can be obtained as:

$$\boldsymbol{R^b_{f,S_i}} = \begin{bmatrix} -sin(-\alpha_i) & -cos(-\alpha_i) & 0 \\ 0 & 0 & 1 \\ -cos(-\alpha_i) & sin(-\alpha_i) & 0 \end{bmatrix} \quad , \quad \boldsymbol{F_{i_b}} = \boldsymbol{R^b_{f,S_i}} \begin{bmatrix} L_i \\ D_i \\ 0 \end{bmatrix} \quad , \quad \boldsymbol{M_{i_b}} = \begin{bmatrix} 0 \\ -M_i \\ 0 \end{bmatrix} \tag{2.12}$$

The resulting forces and moments on the wing are then:

$$\boldsymbol{F_{w_b}} = \sum_{i=1}^{2} \boldsymbol{F_{i_b}} \quad , \quad \boldsymbol{M_{w_b}} = \sum_{i=1}^{2} \boldsymbol{M_{i_b}} + \sum_{i=1}^{2} \begin{bmatrix} 0 & -z_{i_b} & y_{i_b} \\ z_{i_b} & 0 & -x_{i_b} \\ -y_{i_b} & x_{i_b} & 0 \end{bmatrix} \boldsymbol{F_{i_b}} \tag{2.13}$$

Hybrid Plane

The aerodynamic surfaces of the Hybrid Plane will be divided in 6 sections, separating each section of the wing with control surfaces (fig. 2.17).

For the control surfaces, the approach presented in [33] will be adopted, considering the change in

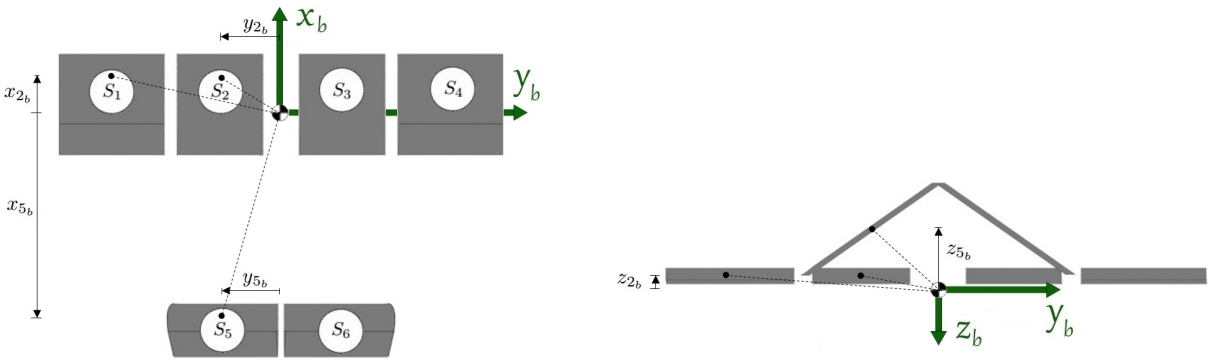

(a) Top view (b) Back view

Figure 2.17: Aerodynamic surfaces sections

angle of attack function of the change in the airfoil chamber.

$$\Delta\alpha_i = -2\frac{l_{\delta_i}}{c_{w_i}^2} l_{c_i}\ sin(\delta_i) \tag{2.14}$$

with l_δ as the control surface width, l_c is the distance of the aerodynamic centre from the leading edge, and c_w is the wing chord. These are illustrated in figure 5.15.

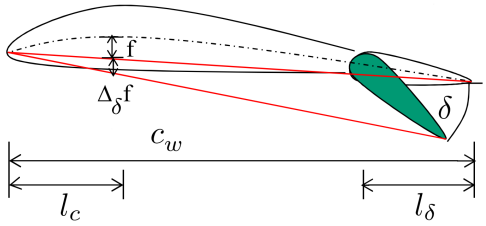

Figure 2.18: Control surface deflection [33]

Since the aerodynamic surfaces are not aligned with the body reference frame, the angle of attack and air speed are calculated as presented in 2.15, with the effective airspeed obtained in the local reference frame of each section V_{ef,i_w}:

$$\boldsymbol{R_{b_i}^w} = \begin{bmatrix} cos(i_w) & 0 & -sin(i_w) \\ 0 & 1 & 0 \\ sin(i_w) & 0 & cos(i_w) \end{bmatrix} \qquad \begin{aligned} &\boldsymbol{V_{ef,i_w}} = \boldsymbol{R_{b_i}^w}\ \boldsymbol{V_{ef,i_b}} \\ &\alpha_i = \Delta\alpha_i + atan2\Big(\big(V_{ef,i_{w,z}} cos(\zeta_i) + V_{ef,i_{w,y}} sin(\zeta_i)\big), V_{ef,i_{w,x}}\Big) \\ &V_{a,i} = \sqrt{\big(V_{ef,i_{w,z}} cos(\zeta_i) + V_{ef,i_{w,y}} sin(\zeta_i)\big)^2 + {V_{ef,i_{w,x}}}^2} \end{aligned} \tag{2.15}$$

The Lift, Drag and Pitching Moment are obtained as in 2.11. The resulting forces for each surface, in the body reference frame:

$$\boldsymbol{R_{f,S_i}^b} = \begin{bmatrix} 1 & 0 & 0 \\ 0 & cos(\zeta_i) & -sin(\zeta_i) \\ 0 & sin(\zeta_i) & cos(\zeta_i) \end{bmatrix} \begin{bmatrix} -sin(i_w - \alpha_i) & -cos(i_w - \alpha_i) & 0 \\ 0 & 0 & 1 \\ -cos(i_w - \alpha_i) & sin(i_w - \alpha_i) & 0 \end{bmatrix} \quad , \quad \boldsymbol{F_{i_b}} = \boldsymbol{R_{f,S_i}^b} \begin{bmatrix} L_i \\ D_i \\ 0 \end{bmatrix} \quad , \quad \boldsymbol{M_{i_b}} = \begin{bmatrix} 0 \\ -M_i \\ 0 \end{bmatrix} \tag{2.16}$$

with ζ_i as the inclination angle of the aerodynamic surface, illustrated in figure 2.7(a).

The resulting forces and moments on the wing are then:

$$\boldsymbol{F_{w_b}} = \sum_{i=1}^{6} \boldsymbol{F_{i_b}} \quad , \quad \boldsymbol{M_{w_b}} = \sum_{i=1}^{6} \boldsymbol{M_{i_b}} + \sum_{i=1}^{6} \begin{bmatrix} 0 & -z_{i_b} & y_{i_b} \\ z_{i_b} & 0 & -x_{i_b} \\ -y_{i_b} & x_{i_b} & 0 \end{bmatrix} \boldsymbol{F_{i_b}} \tag{2.17}$$

2.7.2 Body

Hybrid QuadRotor

The remaining body is composed of the supports for the motors and winglets (fig 2.19). The forces and moments acting there are proportional to the dynamic pressure $q = \frac{1}{2}\rho\, V|V|$, but the actual speed in each infinitesimal area is dependent on the vehicle angular speed and distance from each axis of rotation. The speed on any point p is given as:

$$\boldsymbol{V_{p_b}} = \boldsymbol{V_{a_b}} + \boldsymbol{D_p}\boldsymbol{\omega_b} \quad , \quad \boldsymbol{D_p} = \begin{bmatrix} 0 & z_p & -y_p \\ -z_p & 0 & x_p \\ y_p & -x_p & 0 \end{bmatrix}$$

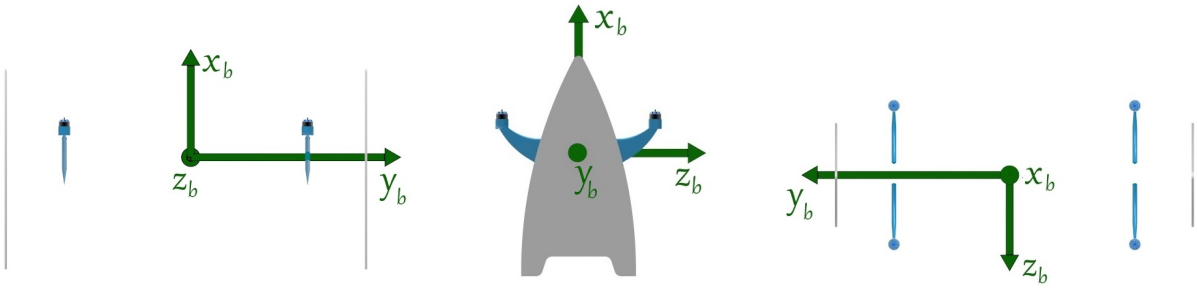

(a) x-y plane (b) x-z plane (c) y-z plane

Figure 2.19: Vehicle body

As a simplification, the speed components will be considered separately. It is not accurate but will give a qualitatively description of the forces involved, and it is a better approximation than of just considering V_{a_b}.

$$\begin{aligned} \boldsymbol{F_{e_b}} = -qAC_DV|V| &\approx -\frac{1}{2}\rho\big(C_D\ A\ \boldsymbol{V_{a_b}}|\boldsymbol{V_{a_b}}| + C_D\ A\ \boldsymbol{D_p}\ |\boldsymbol{D_p}|\ \boldsymbol{\omega_b}\ |\boldsymbol{\omega_b}|\big) \\ &\approx -\frac{1}{2}\rho\big(\boldsymbol{K_A}\ \boldsymbol{V_{a_b}}\ |\boldsymbol{V_{a_b}}| + \boldsymbol{K_D}\ \boldsymbol{\omega_b}\ |\boldsymbol{\omega_b}|\big) \end{aligned} \tag{2.18}$$

The most accurate way to obtain the matrices K_A and K_D would be using CFD or experimentally. In this work, those matrices will be calculated considering a simplified geometry and drag coefficient.

And the same for the moment generated, and respective constant matrices.

$$\boldsymbol{M_{e_b}} \approx -\frac{1}{2}\rho\big(\boldsymbol{K_{MA}}\ \boldsymbol{V_{a_b}}\ |\boldsymbol{V_{a_b}}| + \boldsymbol{K_{MD}}\ \boldsymbol{\omega_b}\ |\boldsymbol{\omega_b}|\big) \tag{2.19}$$

Hybrid Plane

The same approximations and considerations presented for the Hybrid Quadrotor will be taken on this vehicle as well. The force and moment vectors as:

$$\begin{aligned} \boldsymbol{F_{e_b}} &\approx -\frac{1}{2}\rho\big(\boldsymbol{K_A}\,\boldsymbol{V_{a_b}}|\boldsymbol{V_{a_b}}| + \boldsymbol{K_D}\boldsymbol{\omega_b}|\boldsymbol{\omega_b}|\big) \\ \boldsymbol{M_{e_b}} &\approx -\frac{1}{2}\rho\big(\boldsymbol{K_{MA}}\boldsymbol{V_{a_b}}|\boldsymbol{V_{a_b}}| + \boldsymbol{K_{MD}}\boldsymbol{\omega_b}|\boldsymbol{\omega_b}|\big) \end{aligned} \tag{2.20}$$

The body to be considered is composed of the fuselage and the booms, and illustrated in figure 2.20.

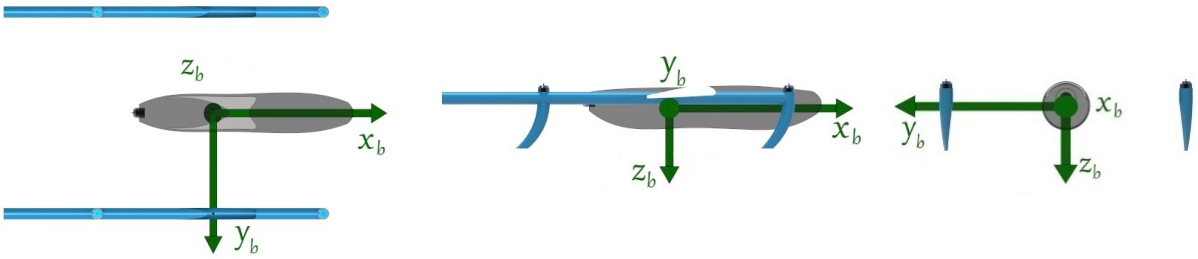

(a) x-y plane (b) x-z plane (c) y-z plane

Figure 2.20: Vehicle body

Chapter 3

Propellers aerodynamic modeling

The model for the propeller was derived using the Blade Element Theory (BET) and Momentum Theory, following the usual analysis for helicopters [31]. This approach disregards the effects of turbulence and compressibility, assumption that looses validity with high air speed.

In this work the effect of blade flapping will be disregarded, since the propellers are small and can be considered of high stiffness. The radial component of the air speed is disregarded, as in the case of lateral air speed in the wings .

An additional reference frame is defined for the propeller analysis (fig. 3.2), with x coincident with the propeller axis, y oriented with component of the external airspeed in the propeller plane, and z oriented normal to both to complete the frame; ξ is the external airspeed incidence angle on the propeller.

The blade is divided into infinitesimal sections along the radius and analysed similarly to the wing (fig 3.1). The relative airspeed between blade and airspeed generates lift, drag and a pitching moment, however that moment will be disregarded since, after a complete rotation, it will cancel out for the most part.

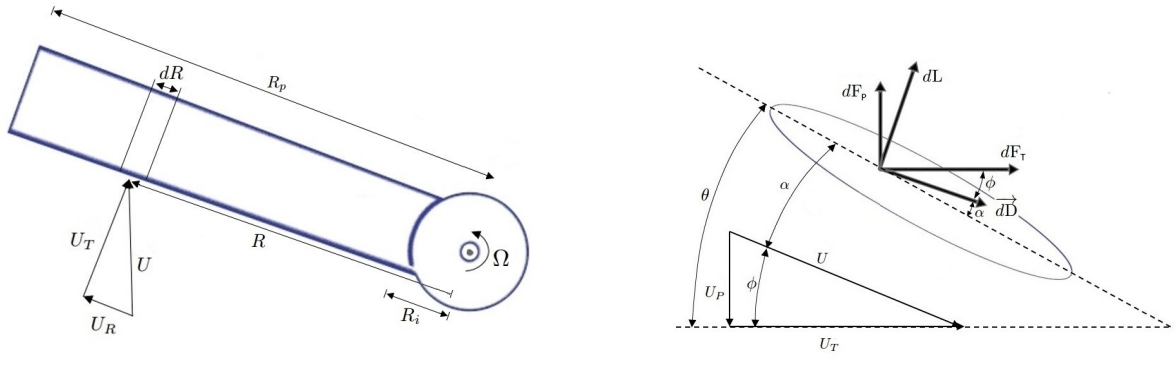

(a) (b)

Figure 3.1: Propeller Blade aerodynamics, [31]

The forces acting on the blade are considered over a complete rotation, considering the blade as an

actuator disc (fig. 3.2). The resulting differential equations are given as:

$$dL = \frac{1}{2}\rho c_p U^2(R,\psi) C_L(\alpha)\, d\psi dR \qquad dD = \frac{1}{2}\rho c_p U^2(R,\psi) C_D(\alpha)\, d\psi dR \tag{3.1}$$

with air density ρ, propeller chord c_p, and function of the radius R and azimuthal position ψ (ilustrated in fig. 3.2(b)). The air speed U is given as $U(R,\psi) = \sqrt{U_T^2(R,\psi) + U_P^2(R,\psi)}$. The tangential component will increase with the radius, and also be affected by the external airspeed V_y depending on the azimuthal position, resulting in $U_T(R,\psi) = \Omega R + V_y sin(\psi)$.

The external air speed is characterised of its incidence angle ξ. The component along the axis of the propeller is given as $U_P(R,\psi) = V_x + V_i(R,\psi)$, where V_i is the inflow. The thrust generated and the inflow are interdependent variables, the propeller generated thrust by increasing the axial speed of V_i, affecting the airspeed and angle of attack, affecting the thrust generated. The problem is solved iteratively.

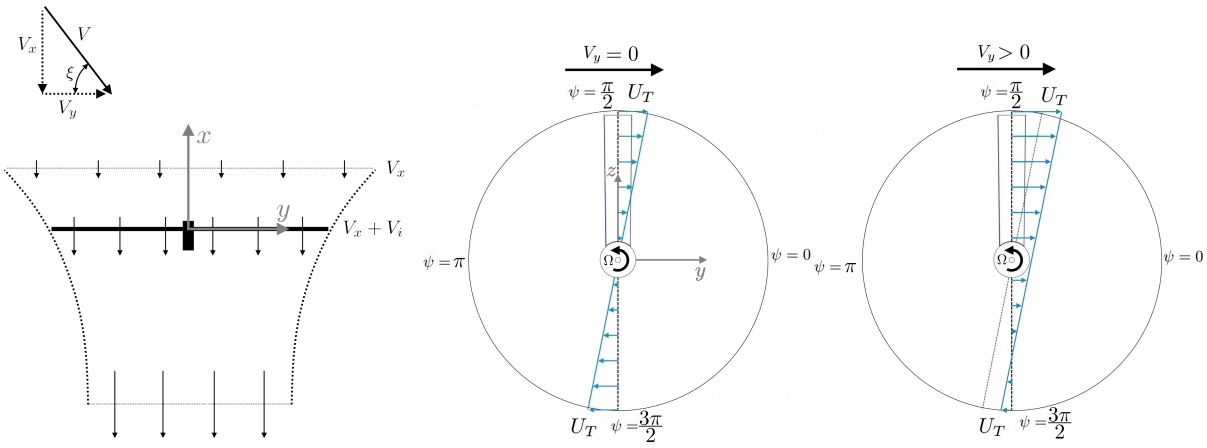

(a) Inflow

(b) Air speed asymmetry

Figure 3.2: Propeller airflow

The lift coefficient, $C_L(\alpha)$, initially was assumed as linear, but later it was found that approximation to be too inaccurate for high pitch propellers, and replaced with a quadratic approximation. For the drag coefficient a quadratic approximation is also used. Both are illustrated in figure 2.10.

$$\begin{aligned} Linear: \quad & C_L(\alpha) = 2C_{L_\alpha}\sqrt{C_{L_\Delta}}\alpha(R,\psi) \\ Quadratic: \quad & C_L(\alpha) = C_{L_M} - (C_{L_\alpha}\,\alpha(R,\psi) - \sqrt{C_{L_\Delta}})^2 \qquad C_D(\alpha) = C_{D_0} + C_{D_\alpha}\alpha^2(R,\psi) \end{aligned} \tag{3.2}$$

The quadratic parameterization is obtained with C_{L_M} as the maximum value, $C_{L_M} - C_{L_\Delta}$ is the function value at zero, and $2C_{L_\alpha}\sqrt{C_{L_\Delta}}$ is the slope at zero. These approximations are illustrated in figure 2.10.

The angle of attack if defined as $\alpha(R,\psi) = \theta(R) - \phi(R,\psi)$, and with the angle of the propeller at a given radius is obtained as $\theta(R) = \theta_0 + \frac{R}{R_p}\theta_{tw}$, as illustrated previously in figure 2.9.

The expressions for the thrust and torque are the result of the integration of the lift and drag forces

along the radius ($R_i < R < R_p$) and in a complete rotation ($0 < \psi < 2\pi$), obtained as:

$$\begin{aligned} T &= \int\int N_b \; dF_P \; d\psi dR = \int_{R_i}^{R_p} \frac{1}{2\pi} \int_0^{2\pi} N_b \big[dL \; cos(\phi(R,\psi)) - dD \; sin(\phi(R,\psi)) \big] \; d\psi dR \\ Q &= \int\int N_b \; dF_T R \; d\psi dR = \int_{R_i}^{R_p} \frac{1}{2\pi} \int_0^{2\pi} N_b \big[dL \; sin(\phi(R,\psi)) + dD \; cos(\phi(R,\psi)) \big] R \; d\psi dR \end{aligned} \tag{3.3}$$

with N_b as the number of blades in the propeller.

But in the presence of air speed in the propeller plane there will be an asymmetry in the forces generated across the disc. On the advancing side ($0 < \psi < \pi$) there will be an increase of thrust, and, in opposition, a reduction of thrust in the retreating side ($\pi < \psi < 2\pi$), causing transverse moments.

$$\begin{aligned} M_y &= \int\int N_b dF_P R sin(\psi) \; d\psi dR = \int_{R_i}^{R_p} \frac{1}{2\pi} \int_0^{2\pi} N_b \big[dL cos(\phi(R,\psi)) - dD sin(\phi(R,\psi)) \big] R sin(\psi) \; d\psi dR \\ M_z &= \int\int -N_b dF_P R cos(\psi) \; d\psi dR = -\int_{R_i}^{R_p} \frac{1}{2\pi} \int_0^{2\pi} N_b \big[dL cos(\phi(R,\psi)) - dD sin(\phi(R,\psi)) \big] R cos(\psi) \; d\psi dR \end{aligned} \tag{3.4}$$

In the analysis of the propeller, the following dimensionless coefficients are defined: Thrust coefficient C_T , Power coefficient C_P, and Transverse Moment coefficients C_{M_y} and C_{M_z}.

$$C_T = \frac{T}{\rho \pi R_p^2 (\Omega R_p)^2} \quad C_P = \frac{P}{\rho \pi R_p^2 (\Omega R_p)^3} \quad C_{M_y} = \frac{M_y}{\rho \pi R_p^3 (\Omega R_p)^2} \quad C_{M_z} = \frac{M_z}{\rho \pi R_p^3 (\Omega R_p)^2}$$

with the Power given as $P = \Omega Q$.

In order to perform the integration of equations 3.3 and 3.4, some simplifications need to be made if an analytic model is desired. In order to evaluate the error associated with these simplifications various models are compared, and a numerical integration of the equations is also used for comparison in a few test cases.

Dimensionless coefficients for the radial coordinate, external airspeed and inflow are also defined:

$$r = \frac{R}{R_p} \quad \mu_x = \frac{V_x}{\Omega R_p} \quad \mu_y = \frac{V_y}{\Omega R_p} \quad \lambda_i(R,\psi) = \frac{V_i(R,\psi)}{\Omega R_p}$$

The models will be numbered according to their complexity, with the simplest being Model 1, and Model 7 the most complex. A summary of the simplifications taken in the various models is presented in the following table:

	Model 1	Model 2	Model 3	Model 4	Model 5	Model 6	Model 7
c_p	+	+	+	+	+	+	+
$C_D(\alpha)$	+	+	+	+	+	+	+
$\theta(R)$	+	+	+	+	+	+	+
$cos(\phi)$	+	+	+	+	•	+	•
$sin(\phi)$	+	+	+	+	•	+	•
$dDsin(\phi)$	+	+	+	+	•	+	•
$U_T(R,\psi)$	+	•	•	•	•	•	•
ϕ	++	++	+	+	•	+	•
$C_L(\alpha)$	++	++	++	++	++	+	+
$\lambda(R,\psi)$	+++	+++	+++	++	+	++	+
exact(•)	small approximation (+)		medium approximation (++)		large approximation (+++)		

3.0.1 Model 1

Model 1 is the simplest model, and the one traditionally used, it disregards the presence of lateral external flow (V_y). This results in a symmetric disc loading, and no generation of transverse moments.

$$U(R,\psi) = \sqrt{U_T^2(R,\psi) + U_P^2(R,\psi)} \approx U_T(R,\psi) \qquad cos(\phi(R,\psi)) \approx 1$$
$$U_T(R,\psi) = \Omega R + V_y sin(\psi) \approx \Omega R \qquad sin(\phi(R,\psi)) \approx \phi(R,\psi)$$
$$\phi(R,\psi) = tan^{-1}\left(\frac{U_P}{U_T}\right) \approx \frac{U_P}{U_T} = \frac{\lambda}{r} \qquad dD\ \phi(R,\psi) \approx 0$$
$$C_L(\alpha) = 2C_{L_\alpha}\sqrt{C_{L_\Delta}}\alpha(R,\psi) \qquad \lambda = \mu_x + \lambda_i \approx \mu_x + \lambda_0$$

For small angles of ϕ the relative air speed can be approximated to the tangential component U_T, $cos(\phi)$ and $sin(\phi)$ can be approximated to 1 and ϕ respectively, and ϕ approximated to U_P/U_T.

Also, since C_D is usually more than one order of magnitude smaller than C_L, and ϕ is small, $dD\phi$ will be much smaller than dL, and so it can be neglected.

This is valid on the outer section of the blade, but as we get close to the centre of the propeller, ϕ reaches high values, and this simplification incurs in a significant error. However, since most of the forces involved are developed predominantly in the outer radius, the error committed is small. These simplifications will also be adopted for models 2 to 4 and model 6.

For this model, and up to model 5, the lift coefficient was considered as linear.

In this model the dimensionless inflow is considered constant across the propeller, equal to λ_0.

3.0.2 Model 2

Moving on to Model 2, U_T was considered as a function of the lateral external flow, but ignored for the calculation of ϕ. Meaning, it would affect the relative air speed at the blade, but not the angle of attack. The analysis of this model, as it will be detailed ahead, shows that it does represents C_T and C_P quite well, but is does not represent C_M even qualitatively, meaning the angle ϕ cannot be ignored

$$
\begin{aligned}
&U(R,\psi) = \sqrt{U_T^2(R,\psi) + U_P^2(R,\psi)} \approx U_T(R,\psi) && cos(\phi(R,\psi)) \approx 1\\
&U_T(R,\psi) = \Omega R + V_y sin(\psi) && sin(\phi(R,\psi)) \approx \phi(R,\psi)\\
&\phi(R,\psi) = tan^{-1}\left(\frac{U_P}{U_T}\right) \approx \frac{U_P}{U_T} \approx \frac{\lambda}{r} && dD\ \phi(R,\psi) \approx 0\\
&C_L(\alpha) = 2C_{L_\alpha}\sqrt{C_{L_\Delta}}\alpha(R,\psi) && \lambda = \mu_x + \lambda_i \approx \mu_x + \lambda_0
\end{aligned}
$$

in the angle of attack, and a more detailed model is necessary.

3.0.3 Model 3

In model 3, V_y is also accounted for the calculation of ϕ, and consequently affecting the angle of attack.

$$
\begin{aligned}
&U(R,\psi) = \sqrt{U_T^2(R,\psi) + U_P^2(R,\psi)} \approx U_T(R,\psi) && cos(\phi(R,\psi)) \approx 1\\
&U_T(R,\psi) = \Omega R + V_y sin(\psi) && sin(\phi(R,\psi)) \approx \phi(R,\psi)\\
&\phi(R,\psi) = tan^{-1}\left(\frac{U_P}{U_T}\right) \approx \frac{U_P}{U_T} = \frac{\lambda}{r + \mu_y sin(\psi)} && dD\ \phi(R,\psi) \approx 0\\
&C_L(\alpha) = 2C_{L_\alpha}\sqrt{C_{L_\Delta}}\alpha(R,\psi) && \lambda = \mu_x + \lambda_i \approx \mu_x + \lambda_0
\end{aligned}
$$

3.0.4 Model 4

In Model 4 a simple model for the inflow is implemented, to assess if there is a visible difference over considering it constant. It was proposed by Coleman et al. [31], and is based on experimental data.

$$
\begin{aligned}
&U(R,\psi) = \sqrt{U_T^2(R,\psi) + U_P^2(R,\psi)} \approx U_T(R,\psi) && cos(\phi(R,\psi)) \approx 1\\
&U_T(R,\psi) = \Omega R + V_y sin(\psi) && sin(\phi(R,\psi)) \approx \phi(R,\psi)\\
&\phi(R,\psi) = tan^{-1}\left(\frac{U_P}{U_T}\right) \approx \frac{U_P}{U_T} = \frac{\lambda}{r + \mu_y sin(\psi)} && dD\ \phi(R,\psi) \approx 0\\
&\lambda_i(R,\psi) = \lambda_0(1 + k_x r cos(\psi)\ ) && \lambda = \mu_x + \lambda_i\\
&C_L(\alpha) = 2C_{L_\alpha}\sqrt{C_{L_\Delta}}\alpha(R,\psi)\\
&k_x = tan\left(\frac{X}{2}\right) && X = tan^{-1}\left(\frac{\mu_y}{\mu_x + \lambda_0}\right)
\end{aligned}
$$

3.0.5 Model 5

Model 5 contains all the equations without approximations, but still considering the linear approximation for the lift coefficient.

The model for the dimensionless inflow λ_i was proposed by Drees [31], and is considered to give a good approximation for the propeller inflow.

$$U(R,\psi) = \sqrt{U_T^2(R,\psi) + U_P^2(R,\psi)} \qquad cos(\phi(R,\psi))$$
$$U_T(R,\psi) = \Omega R + V_y sin(\psi) \qquad sin(\phi(R,\psi))$$
$$\phi(R,\psi) = tan^{-1}\left(\frac{U_P}{U_T}\right) \qquad dDsin(\phi(R,\psi))$$
$$\lambda_i(R,\psi) = \lambda_0(1 + k_x r cos(\psi) + k_y r sin(\psi)\ ) \qquad \lambda(R,\psi) = \mu_x + \lambda_i(R,\psi)$$
$$C_L(\alpha) = 2C_{L_\alpha}\sqrt{C_{L_\Delta}}\alpha(R,\psi) \qquad k_y = -2\mu_y$$
$$k_x = \frac{4}{3}\left(\frac{1 - cos(X) - 1.8\mu_y^2}{sin(X)}\right) \qquad X = tan^{-1}\left(\frac{\mu_y}{\mu_x + \lambda_0}\right)$$

3.0.6 Models 6 and 7

Models 6 and 7 are similar to models 4 and 5 respectively, with the difference of using the quadratic approximation for the lift coefficient.

$$U(R,\psi) = \sqrt{U_T^2(R,\psi) + U_P^2(R,\psi)} \approx U_T(R,\psi) \qquad cos(\phi(R,\psi)) \approx 1$$
$$U_T(R,\psi) = \Omega R + V_y sin(\psi) \qquad sin(\phi(R,\psi)) \approx \phi(R,\psi)$$
$$\phi(R,\psi) = tan^{-1}\left(\frac{U_P}{U_T}\right) \approx \frac{U_P}{U_T} = \frac{\lambda}{r + \mu_y sin(\psi)} \qquad dD\ \phi(R,\psi) \approx 0$$
$$\lambda_i(R,\psi) = \lambda_0(1 + k_x r cos(\psi)\ ) \qquad \lambda = \mu_x + \lambda_i$$
$$C_L(\alpha) = C_{L_M} - (C_{L_\alpha}\alpha(R,\psi) - \sqrt{C_{L_\Delta}})^2$$
$$k_x = tan\left(\frac{X}{2}\right) \qquad X = tan^{-1}\left(\frac{\mu_y}{\mu_x + \lambda_0}\right)$$

$$U(R,\psi) = \sqrt{U_T^2(R,\psi) + U_P^2(R,\psi)} \qquad cos(\phi(R,\psi))$$
$$U_T(R,\psi) = \Omega R + V_y sin(\psi) \qquad sin(\phi(R,\psi))$$
$$\phi(R,\psi) = tan^{-1}\left(\frac{U_P}{U_T}\right) \qquad dDsin(\phi(R,\psi))$$
$$\lambda_i(R,\psi) = \lambda_0(1 + k_x r cos(\psi) + k_y r sin(\psi)\ ) \qquad \lambda(R,\psi) = \mu_x + \lambda_i(R,\psi)$$
$$C_L(\alpha) = C_{L_M} - (C_{L_\alpha}\alpha(R,\psi) - \sqrt{C_{L_\Delta}})^2 \qquad k_y = -2\mu_y$$
$$k_x = \frac{4}{3}\left(\frac{1 - cos(X) - 1.8\mu_y^2}{sin(X)}\right) \qquad X = tan^{-1}\left(\frac{\mu_y}{\mu_x + \lambda_0}\right)$$

3.1 Analysis

The models were analysed by comparing the four dimensionless coefficients ($C_T, C_P, C_{M_y}, C_{M_z}$), in respect to the advance ratio J, with $J = \frac{V_x}{2\Omega R_p}$, in different scenarios of propeller angular speed and incidence angle.

- $2000rpm$, with incidence angle of $90°$, $60°$ and $30°$.
- $5000rpm$, with incidence angle of $90°$, $60°$ and $30°$.

For the propellers, one low pitch propeller (14x6) and one high pitch propeller (14x13) were considered. APC Propellers provides performance data for all their propellers, which was used for comparison with the model results. That data was obtained with CFD analysis, considering Vortex Theory. A more detailed explanation of the methodology can be found on their website [34]. Those propellers have a varying chord, and the blades do not have a constant twisting rate as it is considered in all the models presented here. The specifications considered to represent those propellers are presented in table 3.1.

APC	Model										
	N_p	$R_p(m)$	r_0	$c_p(m)$	$\theta_0(^\circ)$	$\theta_{tw}(^\circ)$	C_{L_α}	C_{L_M}	C_{L_Δ}	C_{D_α}	C_{D_0}
14×6	2	0.1778	0.1	0.027	31°	-27°	3.4	1.0	0.4	1.5	0.02
14×13	2	0.1778	0.1	0.027	45°	-32°	2.8	1.0	0.4	1.5	0.025

Table 3.1: Propeller specifications

The values of θ_0 and θ_{tw} are presented in degrees for an easier representation, but in the calculations radians are used. The absolute values of C_T, C_P,C_{M_y} or C_{M_z} do not have particular significance, the interest is in comparing them between models and scenarios. Given some curves overlap, they were also identified in each figure by their number. The distribution of thrust coefficient and angle of attack were also analysed in some test cases, with lateral external flow from left to right and counterclockwise rotation of the propeller, as illustrated in figure 3.2.

3.1.1 Axial flow ($\xi = 90^\circ$)

As expected, with incidence angle of 90°, both moment coefficients C_{M_y} and C_{M_z} are equal to 0 in all models.

In C_T and C_P, for the case of the low pitch propeller, models 1 to 4 (fig. 3.3 and 3.4) produce equal results, which was predictable as most of the differences relate to terms depending on the external lateral air flow (V_y).

Model 5 provides results slightly different with increased value of J. A larger advance ratio means a higher external axial air speed, and consequently a higher ratio between the axial and tangential air speeds. This leads to a large value of ψ, causing a significant error in the simplifications involving ψ, taken in models 1 to 4.

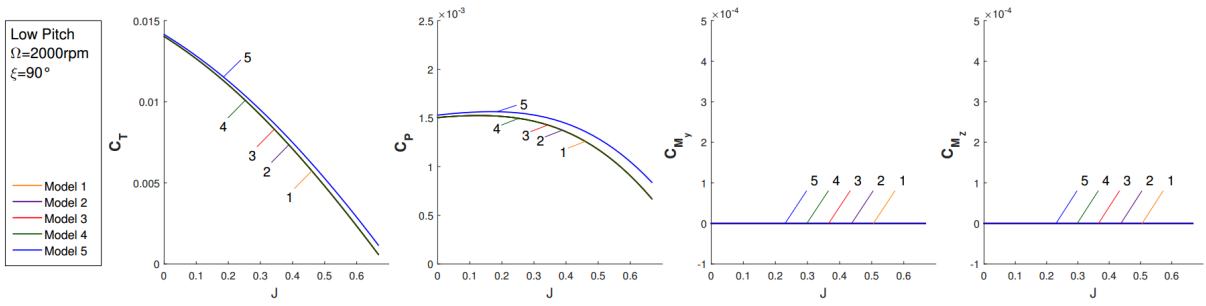

Figure 3.3: Dimensionless coefficients, $\Omega = 2000$rpm, $\xi = 90^\circ$, low pitch, models 1 to 5

This is most visible in the power coefficient, because the component related to the lift, which is the major component of the power, is affected twice by this error. The lift itself is function of ψ, introducing error in the lift, but it is then multiplied by ψ, increasing that error quadratically.

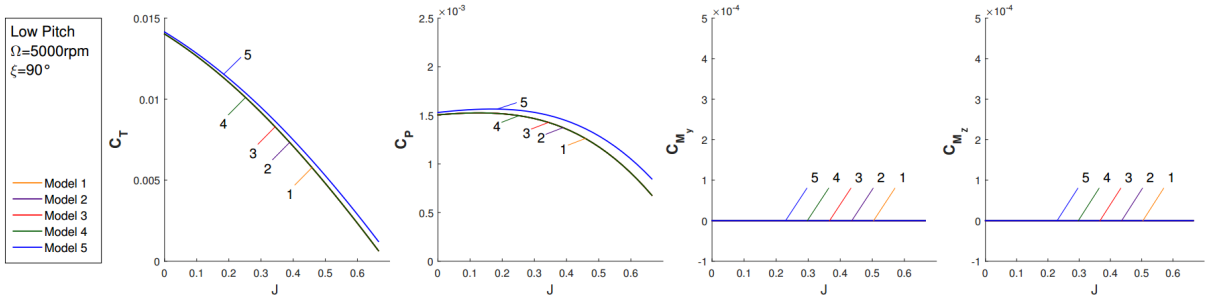

Figure 3.4: Dimensionless coefficients,$\Omega = 5000$rpm, $\xi = 90°$, low pitch, models 1 to 5

Models 6 and 7 (fig. 3.5 and 3.6) provide results significantly different, and closer to the data provided by APC, showing that even for a low pitch propeller the approximation used has some impact.

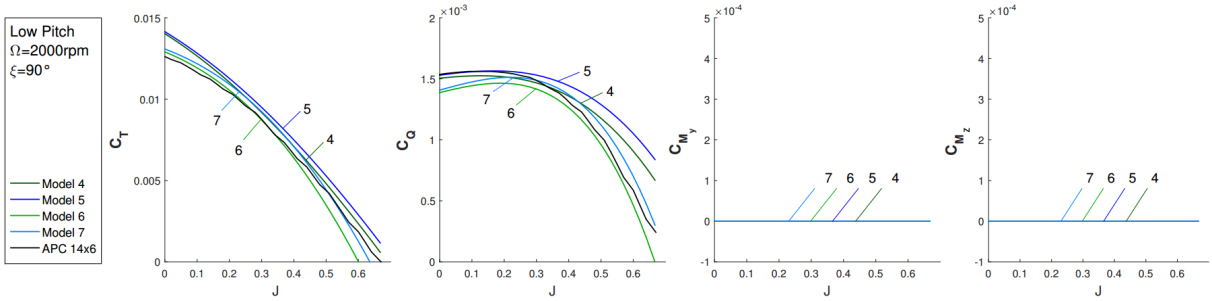

Figure 3.5: Dimensionless coefficients, Ω =2000rpm, $\xi = 90°$, low pitch, models 4 to 7

Again, this is most visible in the power coefficient, as the angle of attack is a function of the angle ψ, the approximation used for the angle of attack will also make a significant difference in increasing that error.

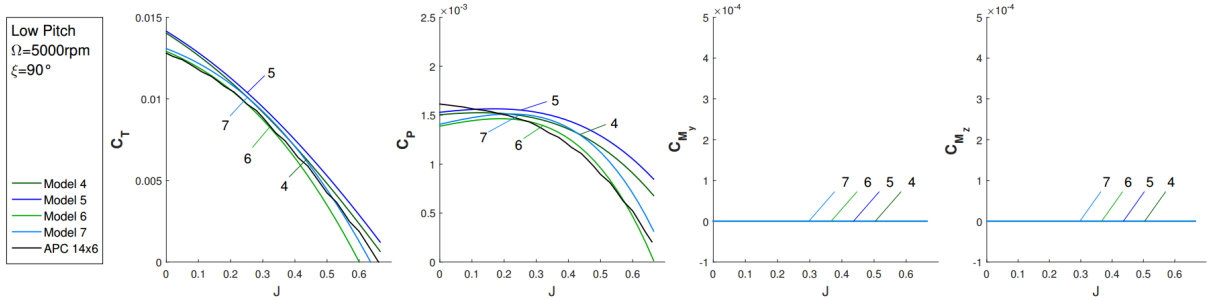

Figure 3.6: Dimensionless coefficients, $\Omega = 5000$rpm, $\xi = 90°$, low pitch, models 4 to 7

With angular speed $\Omega = 5000rpm$, at low advance ratio, it is visible a slight increase in the power coefficient in the data from APC relatively to $\Omega = 2000rpm$. At high angular speed and low J the angle ϕ will be minimum, and in opposition α will be greater. Also, a high angular speed means the outer region of the blade will be moving at a high speed, and reaching a higher Reynolds Number. The conjugation of a high angle of attack with a high Reynolds number will lead to a turbulent air flow, and possible separation of the boundary layer (fig 3.7). These effects will significantly increase the drag of the blades, and the power coefficient. Since the models do not take those effects into account, they will incur in a significant error.

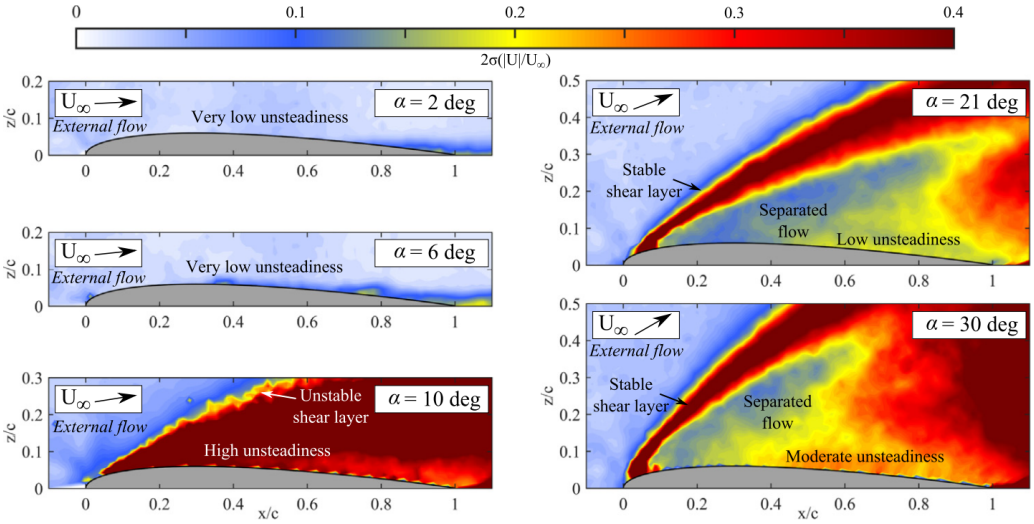

Figure 3.7: Airflow in high angles of attack [29]

For the case of the high pitch propeller (fig 3.8), models 1 to 5 behave similarly to the case of the low pitch propeller, with an increase in the difference between model 5 and the remaining 4. Also, they achieve higher advance ratios and higher values of thrust and power coefficient.

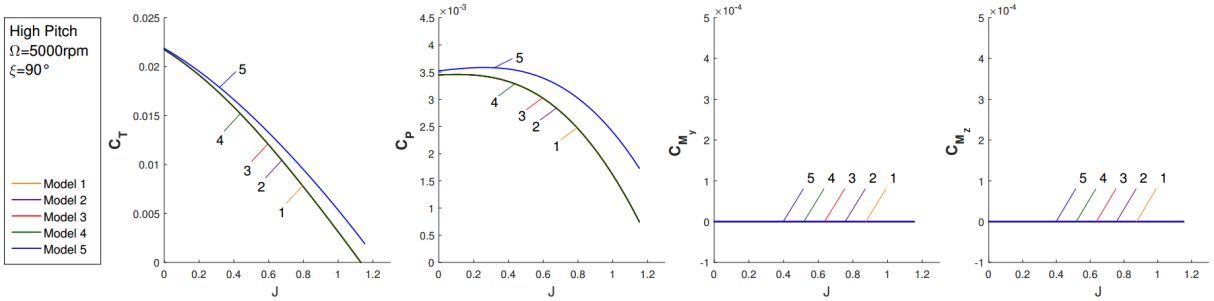

Figure 3.8: Dimensionless coefficients, $\Omega = 5000$rpm, $\xi = 90°$, high pitch, models 1 to 5

But both models 6 and 7 (fig 3.9 and 3.10) show a behaviour much different from models 1 to 5, and close to the results obtained from APC, and what would be expected from the literature (fig 3.11). The average high angle of the propeller blades results in a high angle of attack at low advance ratios, and part of the blade reaching stall, keeping the thrust coefficient nearly constant with $J < 0.6$.

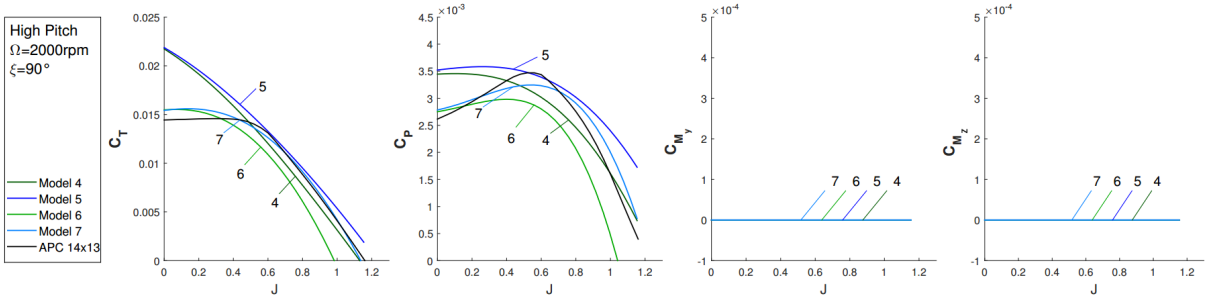

Figure 3.9: Dimensionless coefficients, $\Omega = 2000$rpm, $\xi = 90°$, high pitch, models 4 to 7

The linear approximation for the lift coefficient, used in models 1 to 5, leads to an unrealistic continu-

ous increase of thrust coefficient, which would provide a better efficiency at low advance ratios than low pitch propellers.

In the power coefficient, with $\Omega = 2000rpm$, models 6 and 7 display a similar behaviour to the data from APC, with a maximum at $J \approx 0.6$ and a decline at lower values of J. Models 4 and 5 have a significantly higher power coefficient at low values of J.

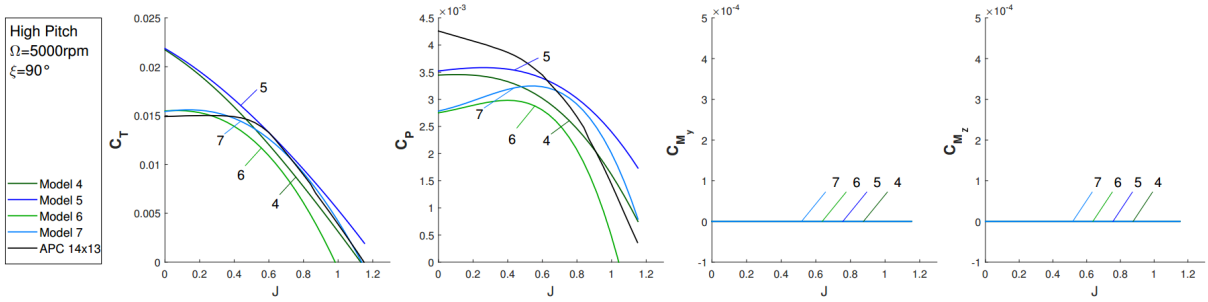

Figure 3.10: Dimensionless coefficients, $\Omega = 5000$rpm, $\xi = 90°$, high pitch, models 4 to 7

However, with $\Omega = 5000rpm$, there is a significant increase in C_p at lower values of J. The propeller blade has a higher angle, increasing the effects of the turbulent flow, and affecting higher values of advance ratio.

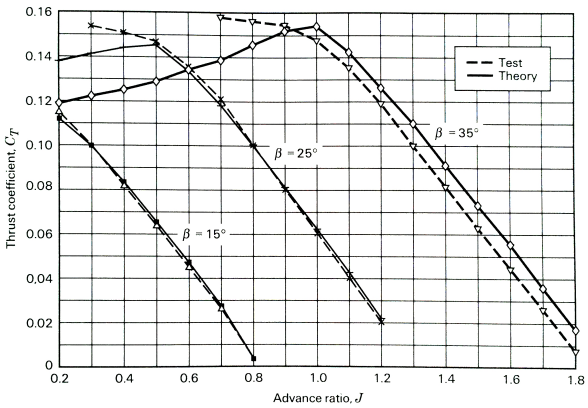

Figure 3.11: Thrust coefficient for various blade angles [35]

In figure 3.12(a), the thrust coefficient distribution across the propeller disc, for the various models, is presented. Areas in red are areas with a higher thrust coefficient, per unit area. In centre of the propeller, with $R < R_i$, there is no thrust generated.

In figure 3.12(b), it is indicated the angle of attack of the propeller, at any point during a rotation.

Both distribution graphics are very similar across the models, for the case of the low pitch propellers. Near the inner radius, in models 1 to 4 and model 6, all reach negative values for the angle of attack, and thus negative thrust, while models 5 and 7 do not reach negative values. Although the blade angle at that radius is not small, near $30°$, due to the approximation used for ϕ in those models, it will reach values above the real one, and above the blade angle. Because of this, in the graphics, the angle of attack was limited to a minimum of $-60°$. Otherwise, in the cases with external lateral air flow and high advance

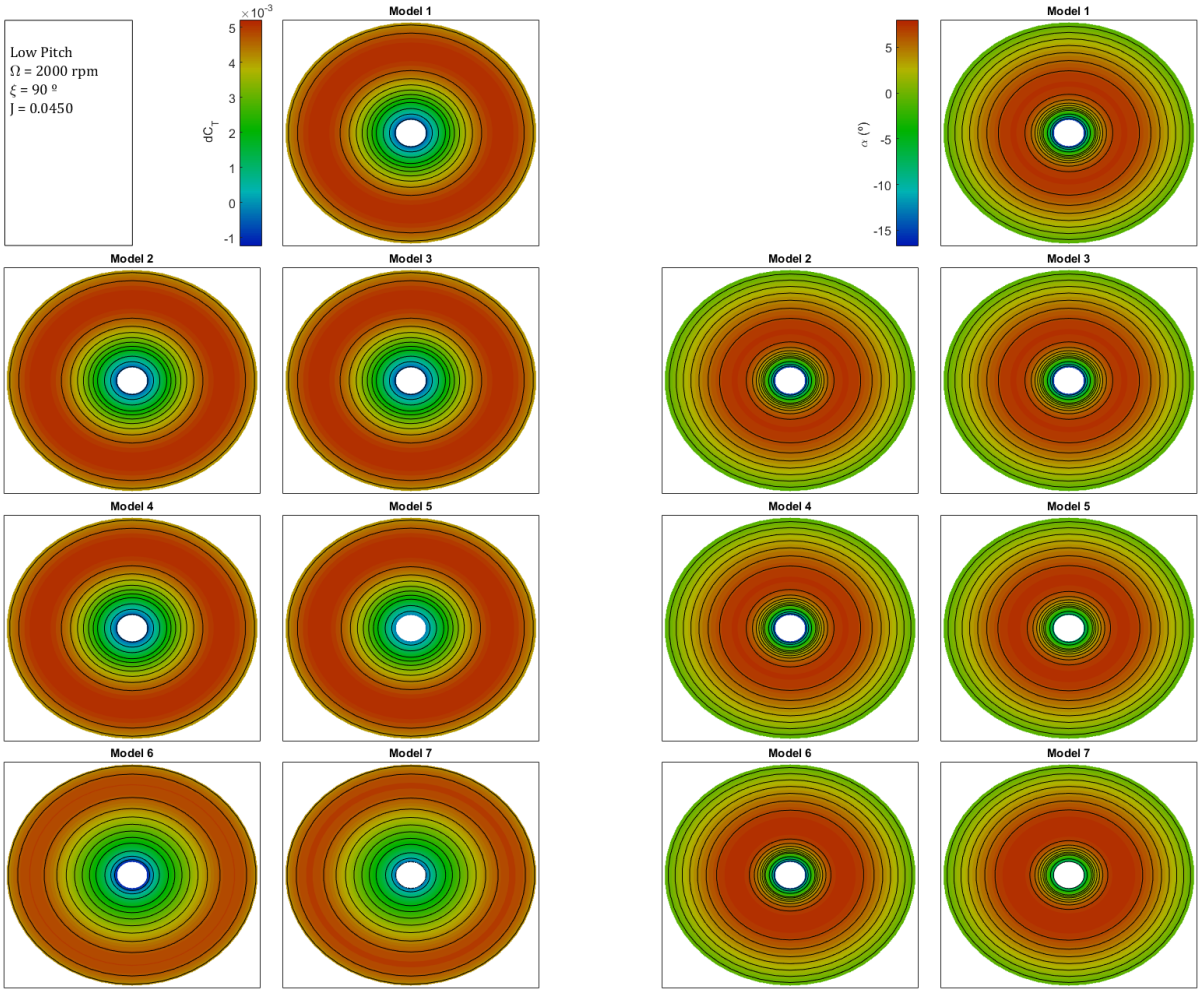

(a) Thrust coefficient distribution

(b) Angle of attack

Figure 3.12: Disc distribution analysis of dC_T and α, depending on the models

ratio, it would reach values towards $-\infty$, and make the graphics completely imperceptible. That error does not significantly affect the results as it occurs near the inner radius, which does not significantly contribute to the result, due to the low local speed.

It is also visible that, for models 1 to 5, the region between approximately 50% and 85% of the radius is where most of the thrust is generated. While the angle of attack is maximum up to around 60%, the relative air speed increases with the radius, and is maximum at the blade tip. That area of maximum thrust is where the product of the angle of attack and relative air speed square are maximum.

For models 6 and 7 the area of maximum thrust is smaller, and with a smaller maximum value, but there is a larger area with high angle of attack. The decrease in thrust reduces the inflow, and subsequently the angle ϕ, increasing the angle of attack.

In the high pitch propeller (fig 3.13), as it was seen for the dimensionless coefficients, there is a significant difference between models 6 and 7 and the remaining 5. In models 6 and 7 the thrust is significantly smaller, and it is maximum at the tip, while for the remaining models it covers a wider area. The angle of attack is also higher in models 6 and 7 as a result of the lower thrust.

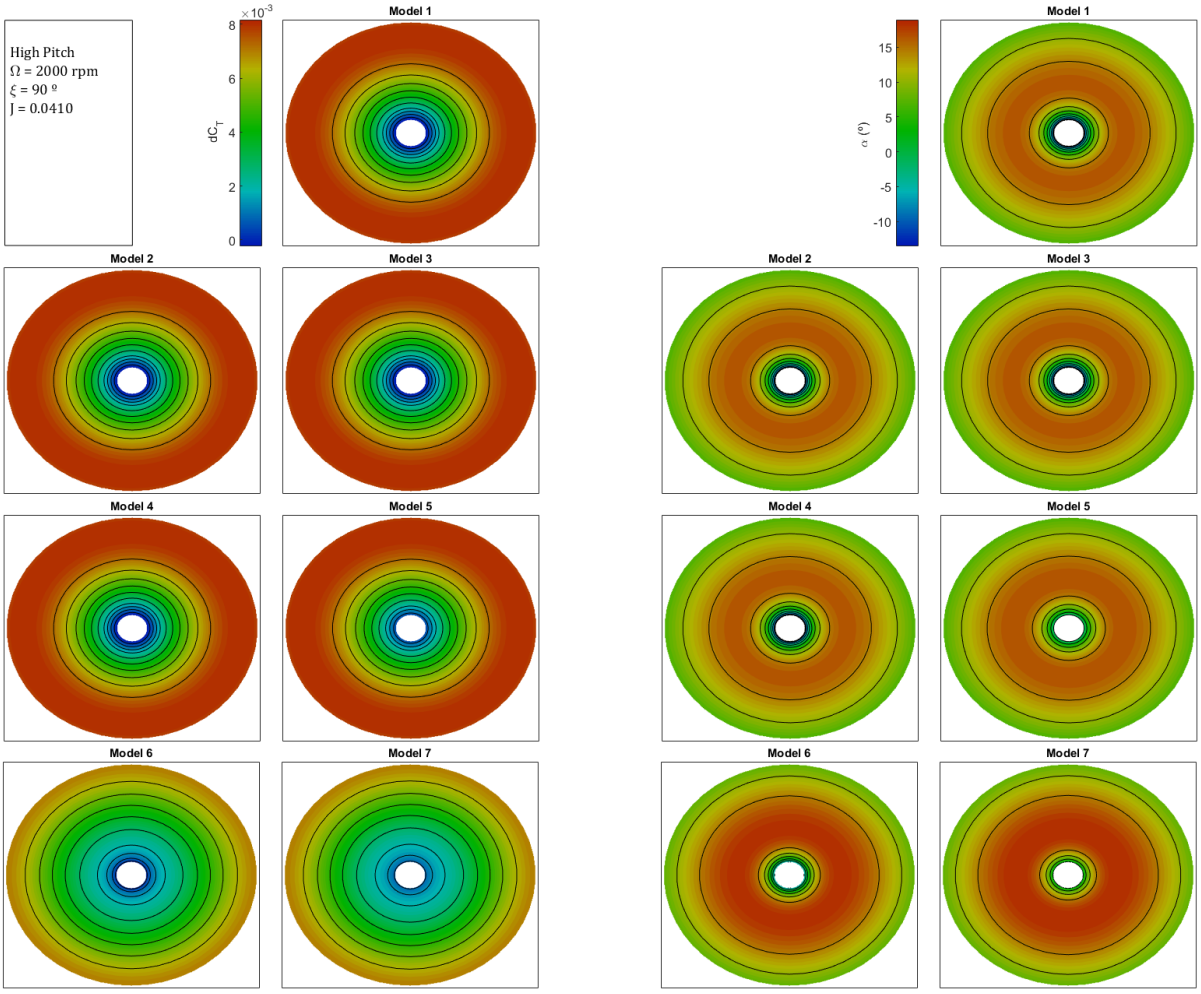

(a) Thrust coefficient distribution

(b) Angle of attack

Figure 3.13: Disc distribution analysis of dC_T and α, depending on the models

3.1.2 Flow with Incidence ($\xi = 60°$)

When introducing external lateral flow V_y (fig. 3.14 and 3.15) bigger differences between the models start to appear, the most obvious is in moment coefficients. Regarding C_{M_y}, in Model 1 it remains equal to zero, since the formulation disregards the external lateral air flow entirely.

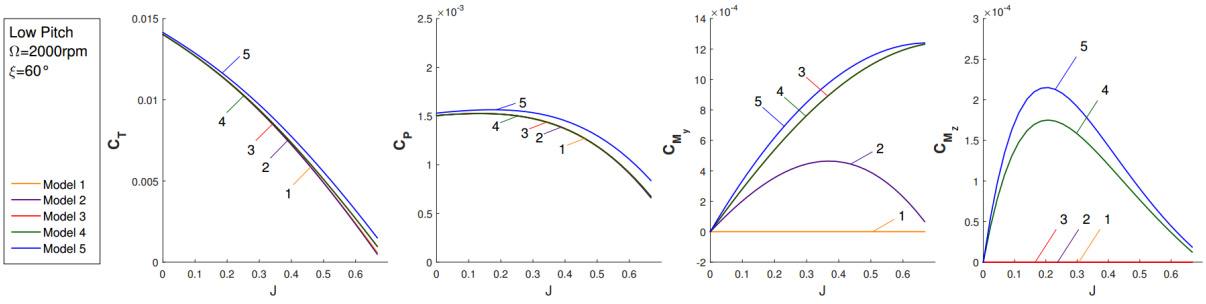

Figure 3.14: Dimensionless coefficients, $\Omega = 2000$rpm, $\xi = 60°$, low pitch, models 1 to 5

Model 2 only takes it into account for the relative air speed, and while at low values of J it gets close

to the more complex models, with higher values it strays away from those. The cause is the angle ϕ, it is increasingly important with the increase of J, and not accounting the external lateral air speed in its calculation results in a significant error.

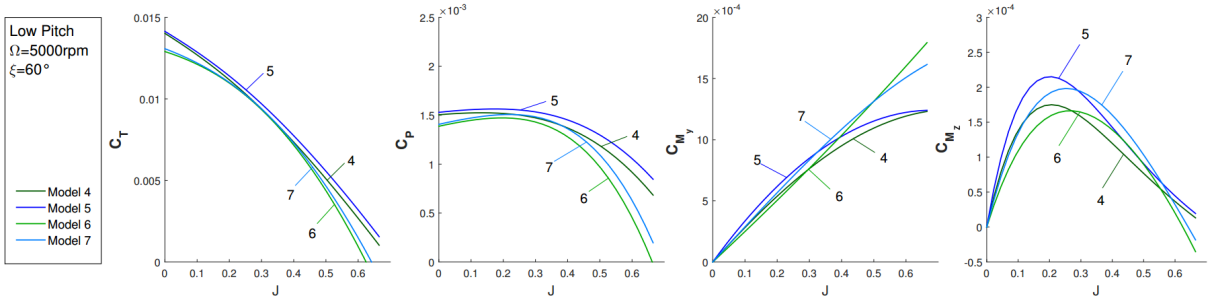

Figure 3.15: Dimensionless coefficients, $\Omega = 5000$rpm, $\xi = 60°$, low pitch, models 4 to 7

Models 3 and 4 are coincident and follow model 5 closely, with a small error for higher values of J. In the case of low pitch propeller, comparing to models 6 and 7, there is a significant error but only at high values of J. But with the high pitch propeller (fig. 3.16) the difference between the models is greater, as expected, and it is occurring at lower values of advance ratio.

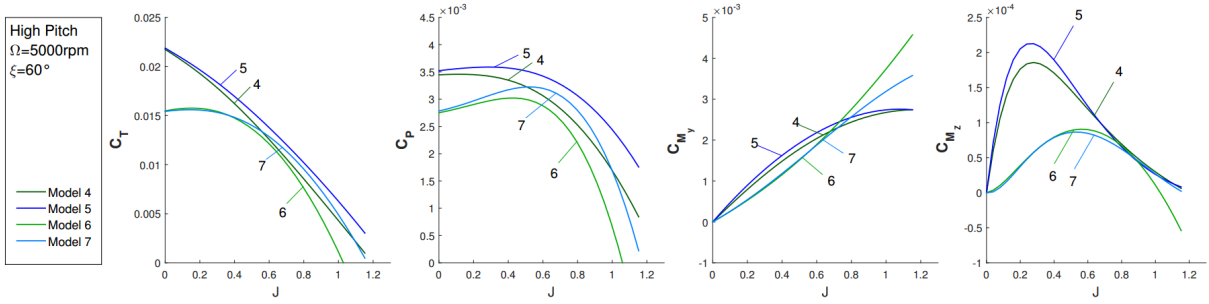

Figure 3.16: Dimensionless coefficients,$\Omega = 5000$rpm, $\xi = 60°$, high pitch, models 4 to 7

The inflow is not constant across the disc, and that effect creates C_{M_z}. Models 1 to 3, by considering the inflow constant, have a null value for that moment. Models 5 to 7 show a similar behaviour in the low pitch propeller, but with some error between models. Model 5 has results closer to 7 and model 4 closer to 6, meaning the approximations for ϕ have a bigger impact than the difference between the inflow models. And the difference in the lift coefficient approximations causes a small shift to the right of the maximum value. In the high pitch propeller, models 6 and 7 have results much smaller than models 4 and 5, as the difference of thrust coefficient has a major impact in the angle of attack and inflow.

The thrust and power coefficient curves are similar to the case of $\xi = 90°$, with a small increase in the error between models 4 and 5 relative to models 6 and 7. It is also visible a small increase in the thrust coefficient and high advance ratio.

In the distribution graphics (fig 3.17) the effect of the various approximations can be seen clearly. In models 2 to 7 there is a shift in the maximum dC_T towards the advancing side, but only in models 3 to 7, the same happens to the angle of attack, as a result of not including ϕ in the angle of attack for model 2.

And in Models 4 to 7, both $d_C T$ and the angle of attack will also have some bias towards the front ($\psi = \pi$), as result of the linear models used for the inflow. At the front the inflow will be smaller, increasing

the angle of attack on that area, and lower at the back, generating M_x.

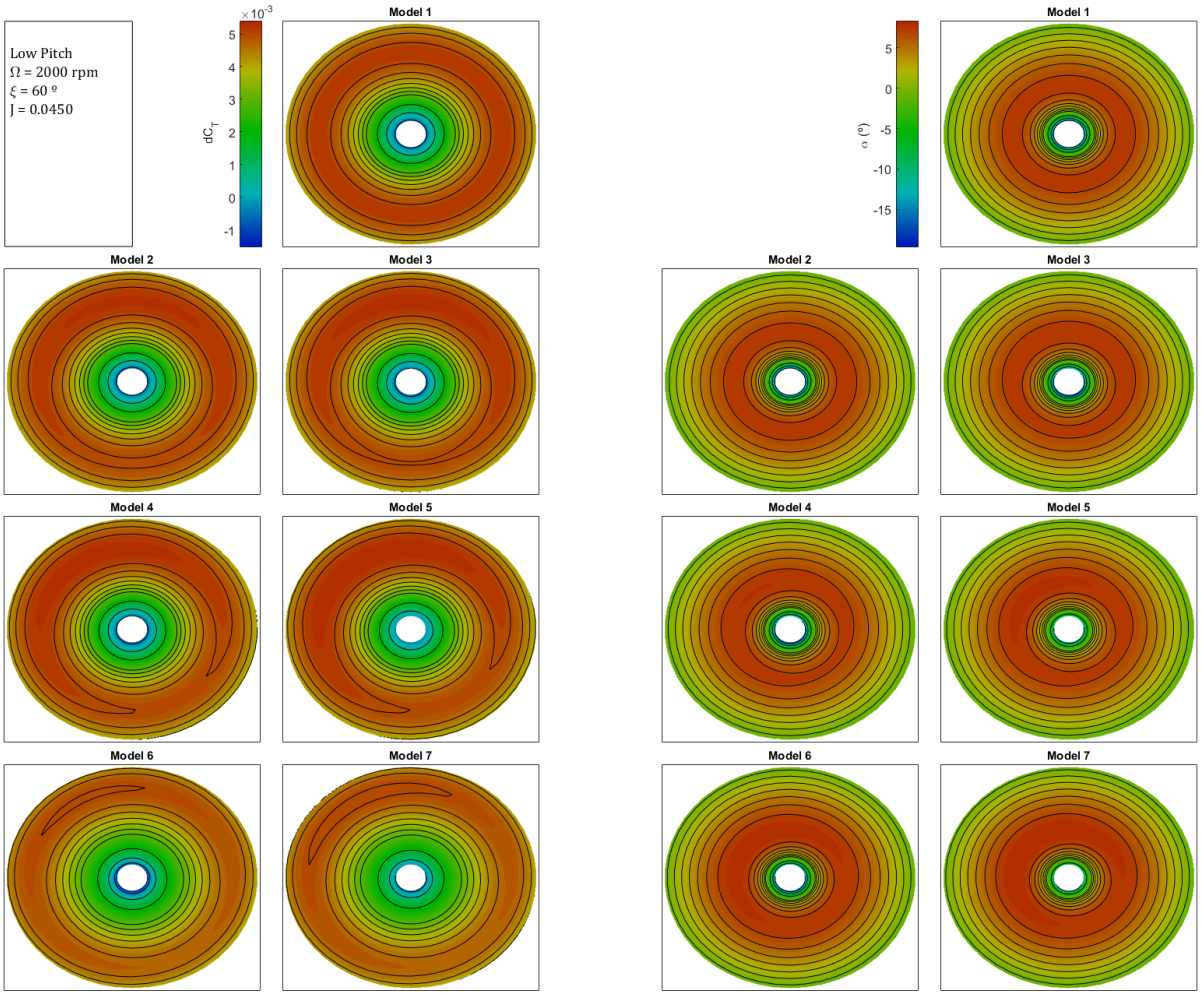

(a) Thrust coefficient distribution

(b) Angle of attack

Figure 3.17: Disc distribution analysis of dC_T and α, depending on the models

These results are similar to what can be seen in the literature [31], as illustrated in figure 3.18. Using a uniform inflow model the angle of attack is relatively symmetric, and using a linear inflow model a bias towards the front appears.

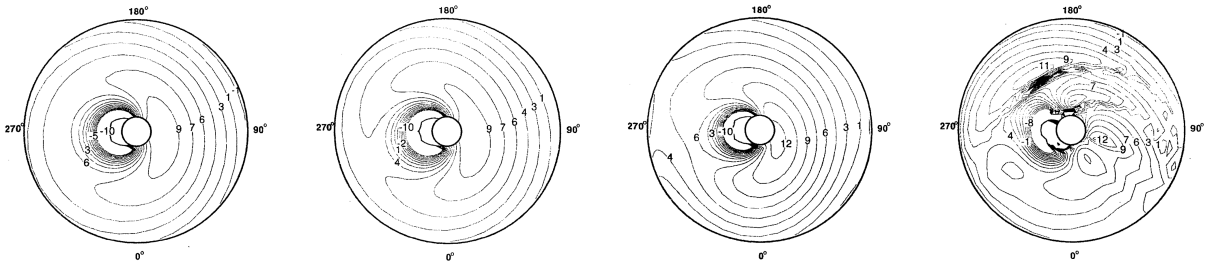

(a) Uniform Inflow

(b) Linear Inflow

(c) Mangler & Squire

(d) Free-vortex wake

Figure 3.18: Angle of attack for 4 inflow models [31]

In the high pitch propeller, (fig. 3.19) model 6 and 7 display very different results from the other models, with lower values for thrust coefficient, higher angles of attack, and highest thrust contribution

at the blade tip. The same bias toward the advancing side and front is visible in all models.

In the high pitch propeller (3.20) model 6 and 7 display very different results from the other models, with lower values for thrust coefficient, higher angles of attack, and highest thrust contribution at the blade tip. The same bias toward the advancing side and front is visible in all models.

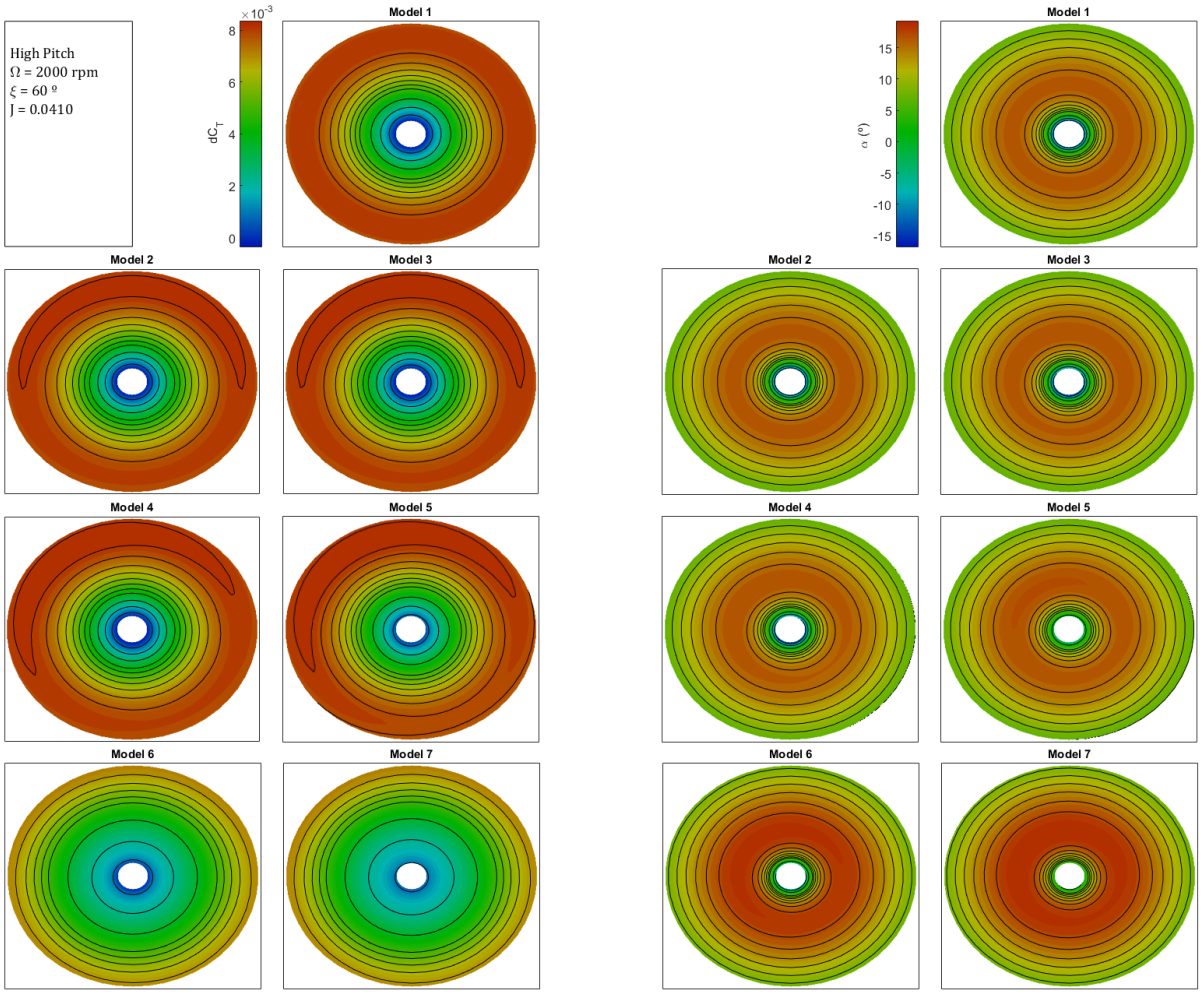

(a) Thrust coefficient distribution

(b) Angle of attack

Figure 3.19: Disc distribution analysis of dC_T and α, depending on the models

Considering a higher value of advance ratio (fig 3.20) the unbalance in the disc loading is much greater, as both V_x and V_y are significantly higher. V_x causes a generalised decrease in the angle of attack, leading to a large area of reverse flow. Note the colour scale is not the same as in the other graphics, as it reaches much lower values of C_T and α.

It is also curious to note that in model 2, the negative thrust is not concentrated on the inner radius of the retreating side, but rather on advancing side. The angle of attack is negative all around the inner radius, as the angle ϕ is not used in its calculation. But the air speed does, and at this value of advance ratio V_y will match the blade speed at the inner radius. On the retreating side the resulting airspeed will be close to 0, as they cancel out, and the resulting thrust is close to 0. But on the advancing side they will add up, and multiplied by the negative α results in a large negative value of thrust. This should be the main reason why the moment coefficient C_{M_y}, in model 2, decreases at high values of advance ratio.

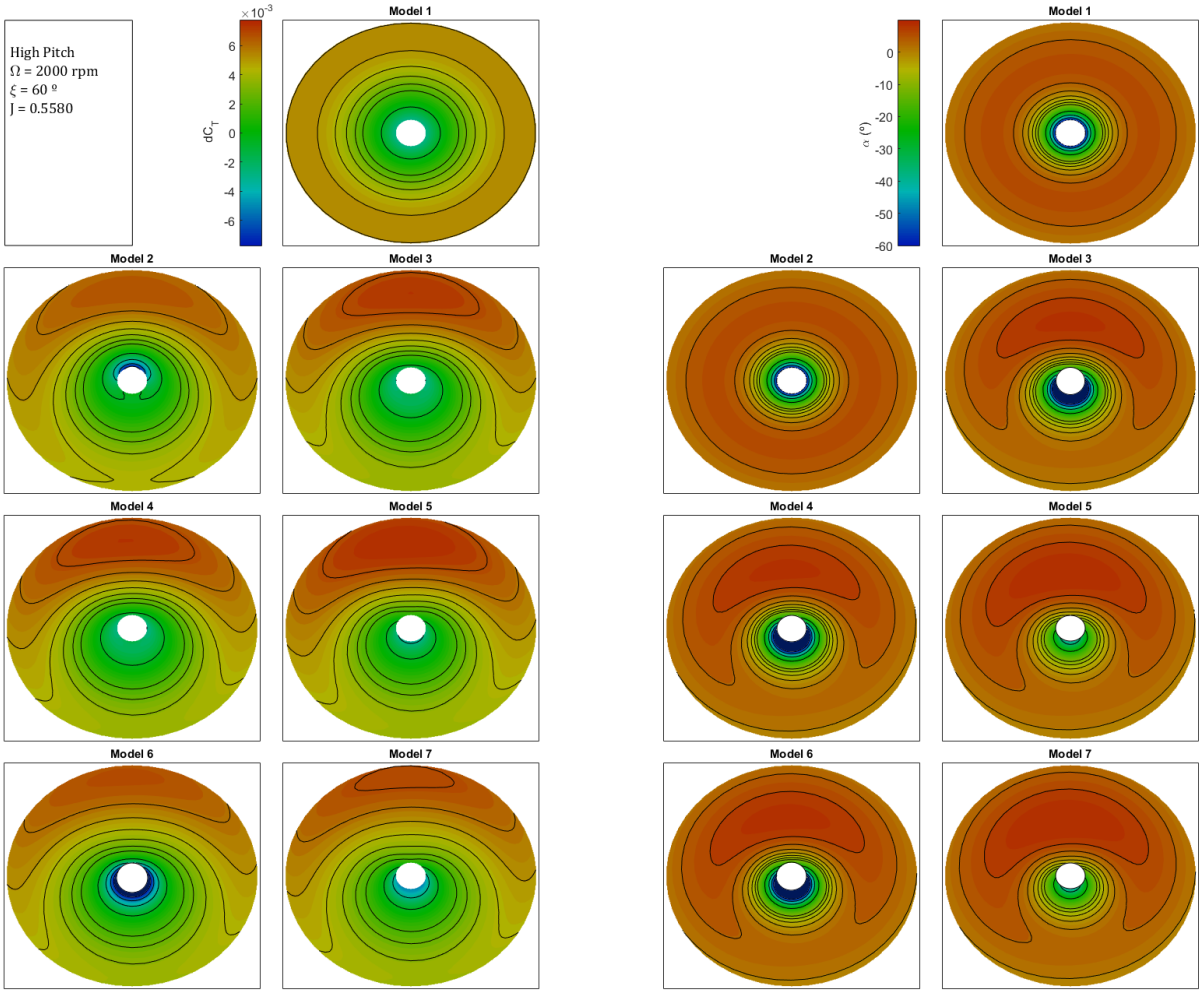

(a) Thrust coefficient distribution

(b) Angle of attack

Figure 3.20: Disc distribution analysis of dC_T and α, depending on the models

3.1.3 Flow with Incidence ($\xi = 30°$)

With $\xi = 30°$, the effects previously referred are simply amplified (fig 3.21). The thrust coefficient has a slight increase at high advance ratio, and both moment coefficients reach higher values as a result of the higher lateral air speed. The error between models 4 and 5, relative to models 6 and 7, also increase, further evidencing the importance of the approximation used for the lift coefficient.

The unbalance in the thrust coefficient distribution and angle of attack are also amplified (fig 3.22).

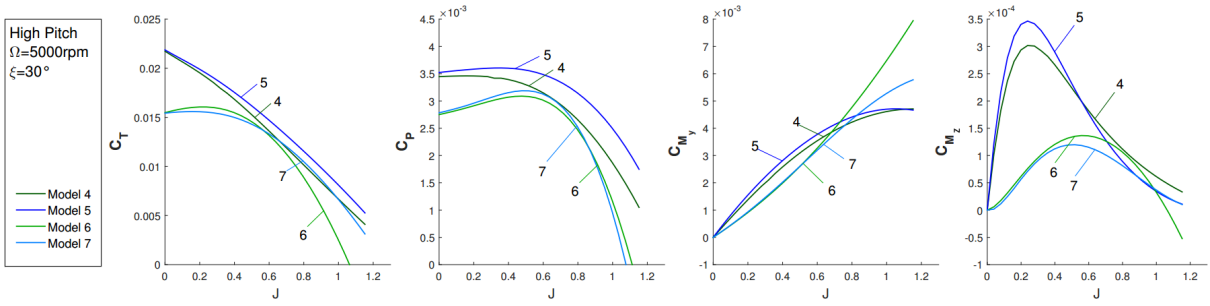

Figure 3.21: Dimensionless coefficients, $\Omega = 5000$rpm, $\xi = 30°$, high pitch, models 4 to 7

Although the differences in the thrust distribution between models 6 and 7 are quite significant, the resulting thrust, power and moment coefficients are not severely affected.

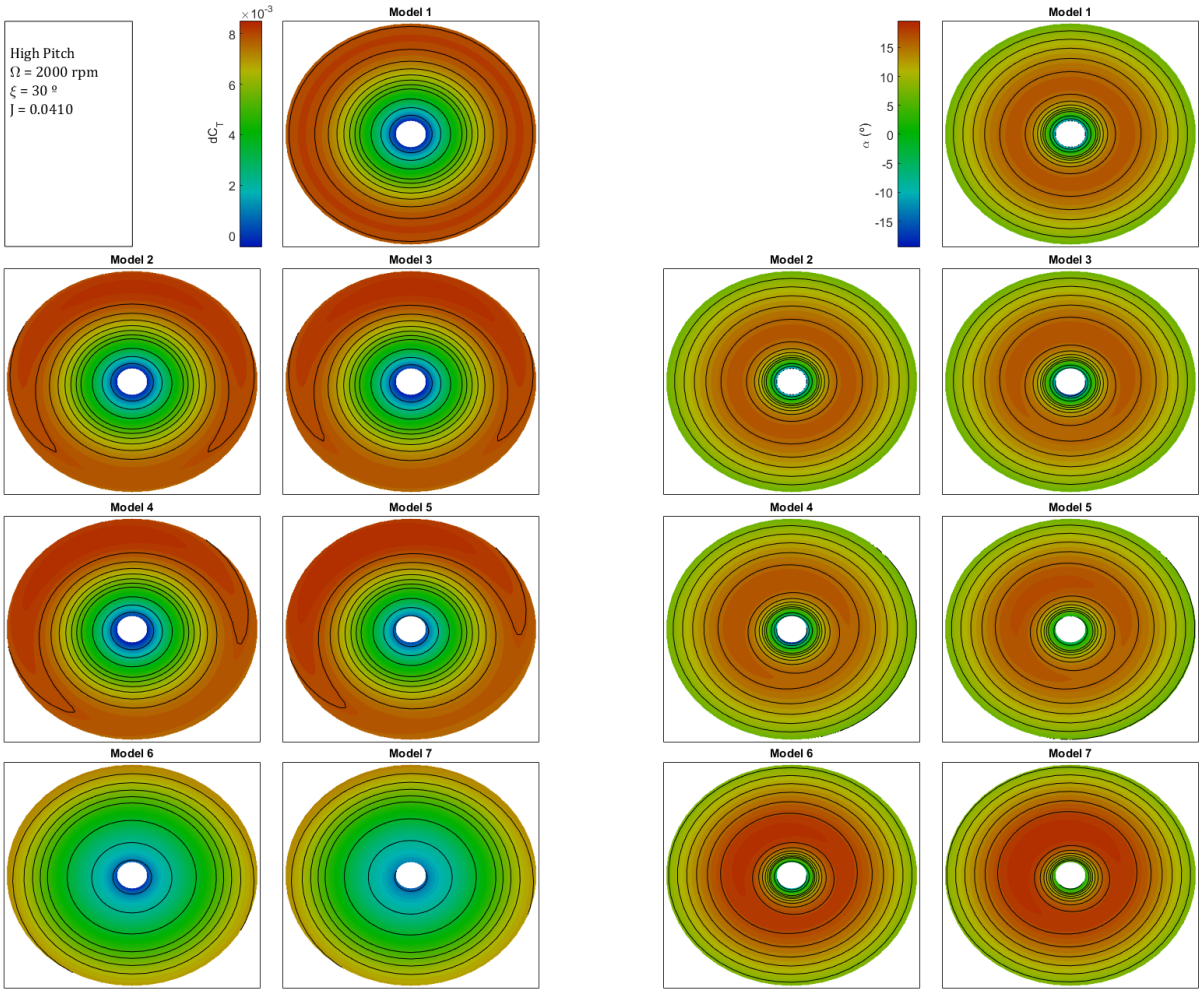

(a) Thrust coefficient distribution

(b) Angle of attack

Figure 3.22: Disc distribution analysis of dC_T and α, depending on the models

3.1.4 Model 6 altered

Most of those differences relate to the approximation used for ϕ, the closer to the inner radius the larger will be the over estimation of ϕ. It is possible to reduce the result difference between models 6 and 7 by increasing the values of blade angle and twisting rate. That way, the angle of attack calculated will be closer to the real one, and obtain results of the coefficients closer to model 7.

In table are presented the parameters considered initially for all models, and with the changes to the blade angle and twisting rate.

APC	Model										
	N_p	$R_p(m)$	r_0	$c_p(m)$	$\theta_0(^\circ)$	$\theta_{tw}(^\circ)$	C_{L_α}	C_{L_M}	C_{L_Δ}	C_{D_α}	C_{D_0}
14×13	2	0.1778	0.1	0.027	$45°$	$-32°$	2.8	1.0	0.4	1.5	0.025
14×13 *altered*	2	0.1778	0.1	0.027	$55°$	$-42°$	2.8	1.0	0.4	1.5	0.025

Table 3.2: Model 6 parameters

Comparing model 6, with the altered parameters, to model 7, with the original parameters (fig 3.23), it shows a significant reduction of the error in the thrust and moment coefficients, specially at high advance ratios, where ϕ reaches higher values. However, the power coefficient suffers a slight increase in the error.

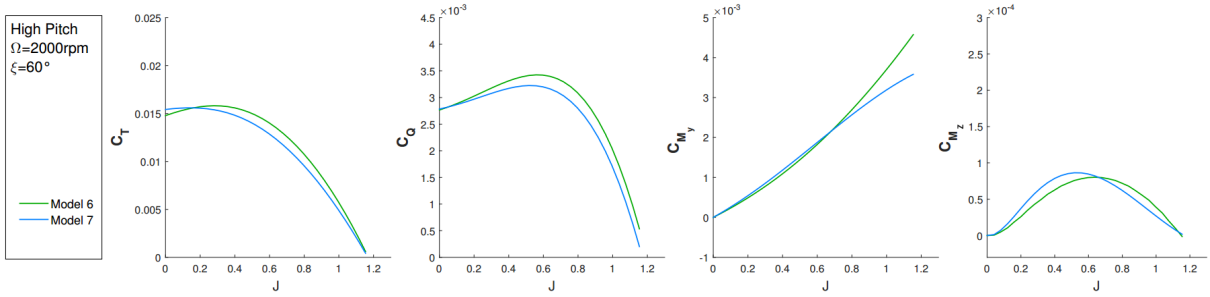

Figure 3.23: Dimensionless coefficients, Ω =2000rpm, $\xi = 60°$, high pitch, models 6 and 7

3.1.5 Error due to turbulent flow

The increase in the power coefficient previously identified at high angular speeds, specially in the high pitch propeller, was also further studied. A total of 12 propellers were analysed, varying in size and pitch, and compared the error between the data provided by APC and the results obtained using model 6, with advance ratio $J = 0$, as it presents the worse case scenario. The model parameters are presented in table A.4.

Assuming that the increase in power is due to turbulence, the blade angular speed and angle of attack would be the major contributors to that effect. After analysing those factors, the following error function was obtained, as better correlating them to the error.

$$e_F = \sqrt{\Omega \; 0.5R_p \; \alpha_{0.5R_p}} \tag{3.5}$$

with $\alpha_{0.5R_p}$ as the angle of attack at half the propeller radius.

Traditionally, propeller specifications are considered at $0.75\ R_p$, as better correlating to the propeller performance. But since the angle of attack is maximum near $0.5\ R_p$, it correlates better to the error.

In figure 3.24 the error between the models and the data from APC is presented, as function of e_F. For values of e_F lower than 7 all the propellers tested have error below the 25% mark, and above 8 show significant error.

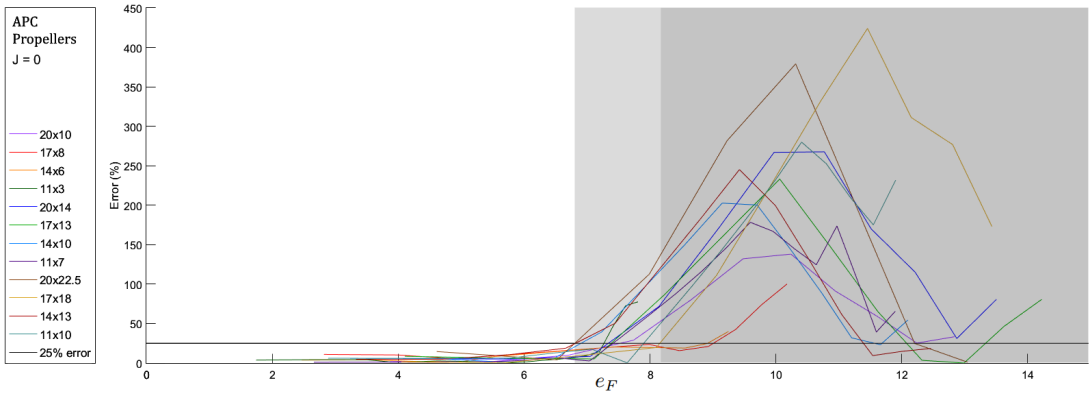

Figure 3.24: Model error for various propellers

That value of 7 will be used as a simple rule to indicate the validity of the results being obtained using the model proposed. If the error function is below the 7, the result will be considered valid (green), but otherwise those results can have significant error.

This is exemplified in figure 3.25, with one of the tests performed. At any speed, the value of the function error remains below 7, meaning the results from that test were valid.

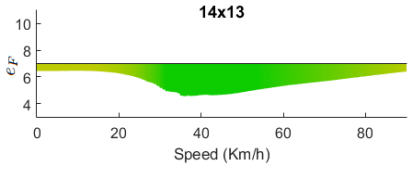

Figure 3.25: Error example for propeller 14×13

3.2 Conclusion

From the simplest model to the most complex analysed, there is a big difference in how the external air flow is considered to behave, how it interacts with the propeller blades, and in the resulting forces and moments. And while even the most complex model analysed disregards some aerodynamic phenomena, it represents a good part of the propeller aerodynamics, resulting in model capable of closely following the results obtained in computational analisys analysis using Vortex theory.

The approximations used for the angle ϕ and relative air speed U have a major influence in the results, and the model used for the inflow is the responsible for the moment M_z.

The analytical model used in simulation of the UAVs dynamics is based in Model 6. The analytic integration of that model results in in the following equations :

$$
\begin{aligned}
C_T = \frac{N_b c_p}{2\pi R_p}\Bigg(& 2C_{L_\alpha}\sqrt{C_{L_\Delta}}\Big[\theta_0\Big(\frac{1-r_i^3}{3}+\mu_y^2\frac{1-r_i}{2}\Big)+\theta_{tw}\Big(\frac{1-r_i^4}{4}+\mu_y^2\frac{1-r_i^2}{4}\Big)-\lambda\frac{1-r_i^2}{2}\Big] \\
& - C_{L_\alpha}^2\Big[\theta_0^2\Big(\frac{1-r_i^3}{3}+\mu_y^2\frac{1-r_i}{2}\Big)+\theta_{tw}^2\Big(\frac{1-r_i^5}{5}+\mu_y^2\frac{1-r_i^3}{6}\Big)+\theta_0\theta_{tw}\Big(\frac{1-r_i^4}{2}+\mu_y^2\frac{1-r_i^2}{2}\Big) \\
& + \lambda^2(1-r_i)-\lambda\theta_0(1-r_i^2)-\frac{2}{3}\lambda\theta_{tw}\Big]+(C_{L_M}-C_{L_\Delta})\Big(\frac{1-r_i^3}{3}+\mu_y^2\frac{1-r_i}{2}\Big)\Bigg) \\
C_P = \frac{N_b c_p}{2\pi R_p}\Bigg(& (C_{L_M}-C_{L_\Delta})\frac{\lambda}{3}-C_{L_\alpha}^2\lambda\Big[\theta_0^2\frac{1-r_i^3}{3}+\theta_{tw}^2\frac{1-r_i^5}{5}+\theta_0\theta_{tw}\frac{1-r_i^4}{2}-\lambda\theta_0(1-r_i^2)-2\lambda\theta_{tw}\frac{1-r_i^3}{3} \\
& + \lambda^2\Big(\sqrt{1-\mu_y^2}-\sqrt{r_i^2}\Big)\Big]+C_{L_\alpha}\sqrt{C_{L_\Delta}}\lambda\Big[2\theta_0\frac{1-r_i^3}{3}+\theta_{tw}\frac{1-r_i^2}{2}-\lambda(1-r_i^2)\Big] \\
& + C_{D_\alpha}\Big[\theta_0^2\Big(\frac{1-r_i^4}{4}+\mu_y^2\frac{1-r_i^2}{4}\Big)+\theta_{tw}^2\Big(\frac{1-r_i^6}{6}+\mu_y^2\frac{1-r_i^4}{8}\Big)+\lambda^2\frac{1-r_i^2}{2}+ \\
& + \theta_0\theta_{tw}\Big(2\frac{1-r_i^5}{5}+\mu_y^2\frac{1-r_i^3}{3}\Big)-2\lambda\Big(\theta_0\frac{1-r_i^3}{3}+\theta_{tw}\frac{1-r_i^4}{4}\Big)\Big]+C_{D_0}\Big[\frac{1-r_i^4}{4}+\mu_y\frac{1-r_i^2}{4}\Big]\Bigg) \\
C_{M_x} = \frac{N_b c_p}{2\pi R_p}\Bigg(& (C_{L_M}-C_{L_\Delta})\mu_y\frac{1-ri^3}{3}+C_{L_\alpha}^2\Big[\lambda\theta_0\mu_y\frac{1-r_i^2}{2}-\theta_0^2\mu_y\frac{1-r_i^3}{3}+\lambda\theta_{tw}\mu_y\frac{1-r_i^3}{3} \\
& - \theta_0\theta_{tw}\mu_y\frac{1-r_i^4}{4}-\theta_{tw}^2\mu_y\frac{1-r_i^5}{5}\Big]-C_{L_\alpha}\sqrt{C_{L_\Delta}}\Big[\lambda\mu_y\frac{1-r_i^2}{2}-2\theta_0\mu_y\frac{1-r_i^3}{3}+\theta_{tw}\mu_y\frac{1-r_i^4}{4}\Big)\Bigg) \\
C_{M_y} = \frac{N_b c_p}{2\pi R_p}\Bigg(& C_{L_\alpha}\sqrt{C_{L_\Delta}}\lambda_0 k_x\frac{1-r_i^4}{4}+C_{L_\alpha}^2\Big[\lambda_0^2 k_x\frac{1-r_i^3}{3}-\lambda_0\theta_0 k_x\frac{1-r_i^4}{4}-\lambda_0\theta_{tw}k_x\frac{1-r_i^5}{5}+\lambda_0 k_x\mu_x\frac{1-r_i^3}{3}\Big]\Bigg)
\end{aligned}
\tag{3.6}
$$

Since r_i is small, equal to 0.1 (table A.4), terms of order higher than 2 can be disregarded, resulting in the equations presented in eq. (2.4).

Chapter 4

Trim of the UAVs dynamics for varying airspeed

With the vehicle modeling finalised, was performed an analysis regarding range, flight time and vehicle orientation. The objective was to test how the vehicles would behave during their operation, and which propellers would be most adequate for each vehicle.

It would also be interesting to test with different motors, but it would significantly increase the size of this analysis. Also, the complete information about motor specifications is not widely available.

For a given flight speed the equilibrium conditions are computed, i.e., the vehicle attitude, propellers rotation and control surfaces deflection necessary to keep the vehicle moving forward at that speed with no change in heading, attitude, or lateral position.

A total of 12 propeller were tested, with varying radius and pitch. The propellers have a major impact in the vehicle power efficiency, this analysis will also help choose the most adequate one for each vehicle. The model characteristics for those propellers are presence in table A.4.

4.1 Hybrid Quadrotor

The Hybrid Quadrotor, given its propulsion and operation characteristics, has one unique equilibrium condition for any given speed. The vehicle pitch angle curve will be the same, independently of the propeller.

The low pitch propellers (fig. 4.1) provide the highest efficiency at Axial flight, with almost twice the flight time of high pitch propellers (fig. 4.4). However, the maximum range and maximum speed will be inferior, as expected. The difference between the propellers is still significant, with the 14×6 and 17×8 obtaining very similar results of flight time at low speeds. At peak efficiency, around $37km/h$ the propeller 20×10 also has equivalent performance to those 2. That peak efficiency occurs at that speed because is when the the vehicle, and consequently the wing, reach an angle around 12° . At that angle the wing drag is significantly reduced, decreasing the necessary propeller angular speed, and leading to a large spike in range.

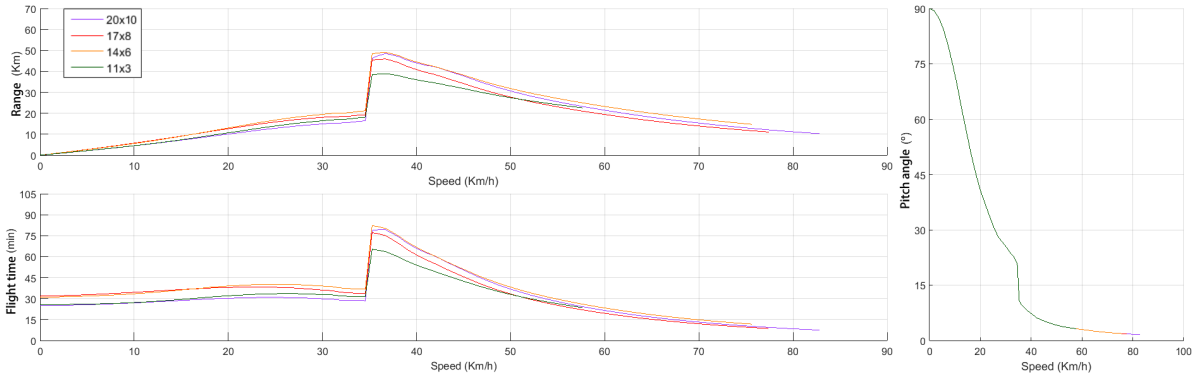

Figure 4.1: Quadrotor trim vs airspeed, with low pitch propellers

The Hybrid Quardrotor has 4 equal propellers, but each will be subject to slightly different conditions. For the analysis of the error function e_F, presented in eq. 3.5, will be selected the propeller of the vehicle with the highest error value.

Only the propeller 20×10 reaches a value of e_F higher than 7, at high speeds. All other propellers are on the green for the entire speed range.

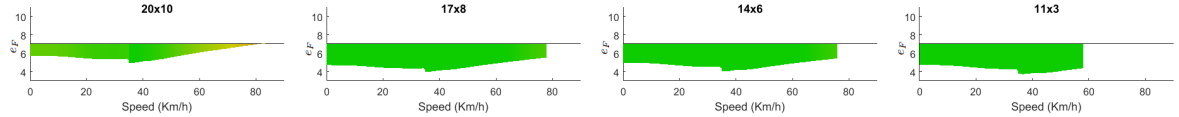

Figure 4.2: Error results for low pitch propellers

The medium pitch propellers (fig. 4.3) give an intermediary result, with the propeller 14×10 reaching around 75% of the flight time at low speeds of the best low pitch propeller, and near 95% of the range of the best high pitch propeller.

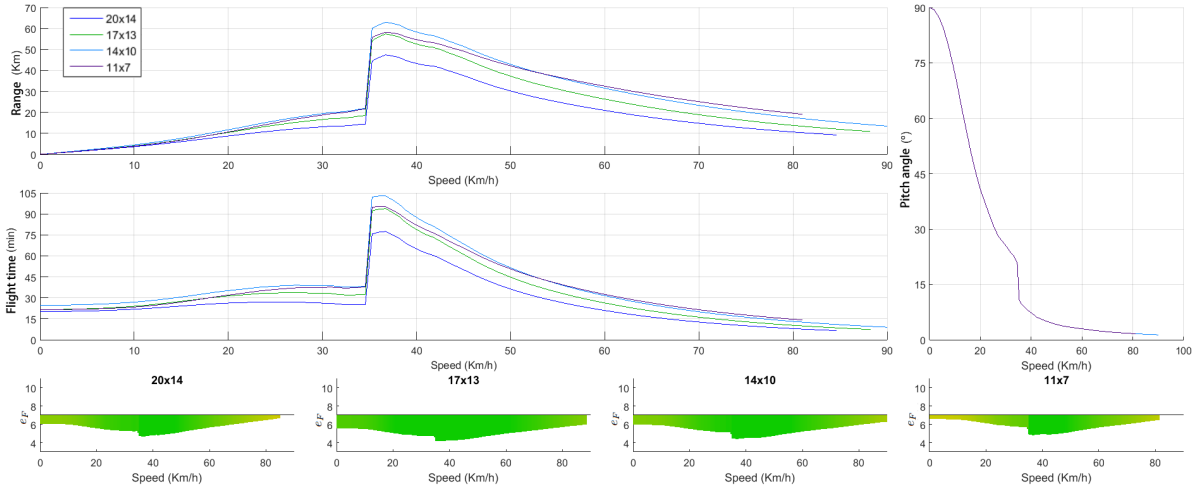

Figure 4.3: Hybrid Quadrotor trim vs airspeed, with medium pitch propellers

Propellers 20×14 and 11×7 reach values of e_F close to 7, but never surpassing it. The other 2 propeller have values further away from the limit.

The high pitch propellers (fig 4.4) do provide the highest range and maximum speed, but only for a

small difference, and the reduction in flight time at low speed is very significant.

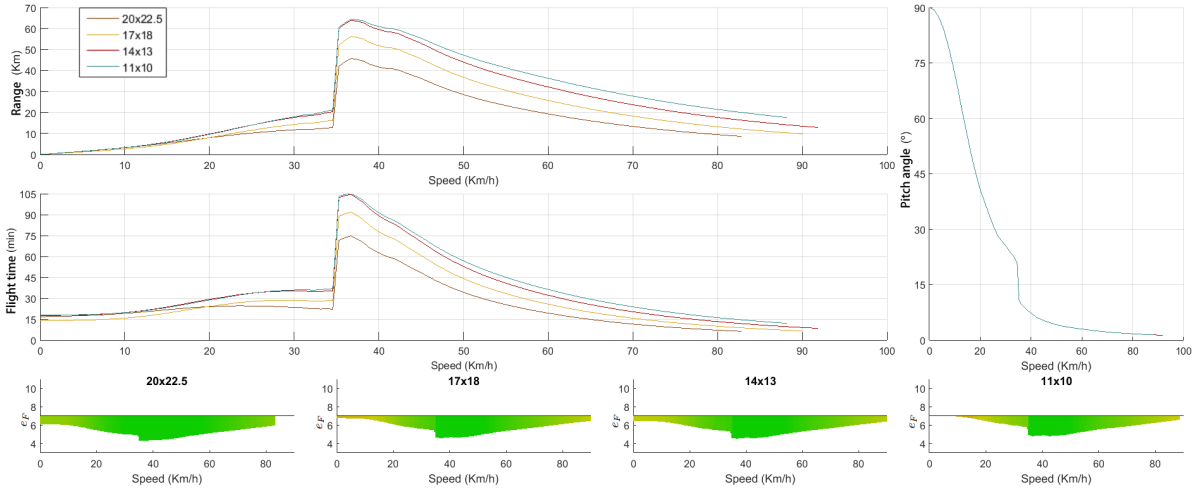

Figure 4.4: Hybrid Quadroto trim vs airspeed, with high pitch propellers

Also, all propellers reach values close to $e_F = 7$, not only at high speeds but also as low speeds. This will significantly affect the efficiency of the vehicle, as during its operation the propellers will reach angular speeds higher than these, in order to accelerate. And at those higher speeds the real torque will be much higher, significantly reducing the flight time.

It is also curious to note that with increased pitch, the smaller the propeller radius the higher the efficiency. In the case of low pitch propellers, the 3 largest propellers have performance significantly better than the smallest one. From the medium pitch propellers, the 14×10 gets the best efficiency. And in the high pitch propellers, the smallest one 11×10 has the best results. At low pitch having a higher rotational speed is more costly than having a larger radius, while with higher pitch having a higher rotational speed produces less torque than a large radius. For a given thrust there is a relation between radius and pitch that provides higher efficiency.

4.2 Hybrid Plane

The Hybrid Plane has redundancy in its propulsion and control system, there is more than one possible set of equilibrium conditions for a given flight speed. The desired flight corresponds to having the vehicle as close as possible to the horizontal position. As seen in the previous section, having an angle of attack higher than $12°$ dramatically increases the drag, and reduces the efficiency. The wing is already at $8°$ relative to the fuselage pitch angle, the pitch of the vehicle was limited to a maximum of $3°$. The vehicle will be kept at that attitude to maximise the lift from the wing, reducing the propeller angular speed.

In Axial flight, the control surfaces will not be actuated, and during Forward flight the propellers 1 to 4 will be turned off. During the transition, those propellers will grant part of the lift, and the control surfaces providing the control. The 5th propeller is responsible for moving the vehicle forward.

The low pitch propellers (fig. 4.5) do provide significantly higher flight time at Axial flight, but the actual decrease in maximum range is very small, compared to the medium and high pitch propellers.

The maximum flight speed is also considerably smaller than with the Hybrid Quadrotor. The Hybrid Plane has only one propeller to propel the vehicle in Forward flight, and its motor will reach its maximum at a lower speed. This could be circumvented by using 2 motor-propellers in the back, or using a more powerful motor.

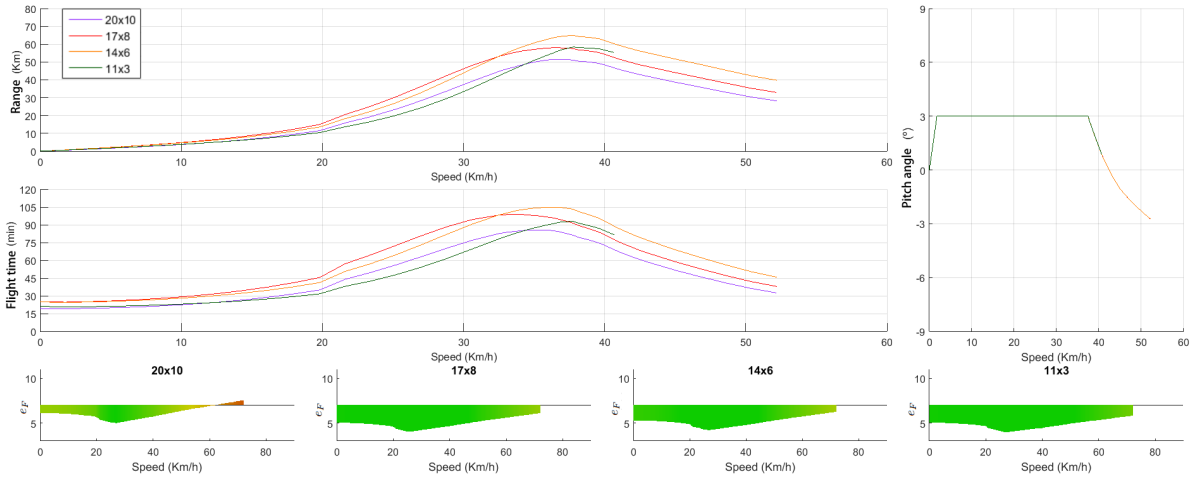

Figure 4.5: Hybrid Plane trim vs airspeed, with high pitch propellers

All the propellers are working in conditions within the accepted range of validity.

The propellers 11×7 and 14×10 have very similar results (fig. 4.6), and have the highest range, along with propeller 11×10 (4.7).

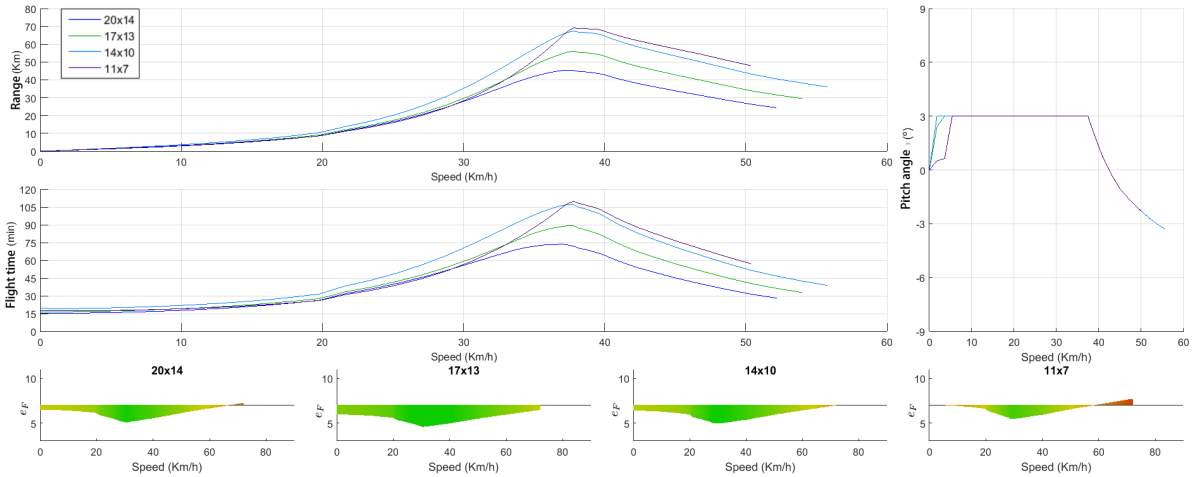

Figure 4.6: Hybrid Plane trim vs airspeed, with low pitch propellers

It has only 1 propeller, requiring a high angular speed to provide enough trust, resulting in a lower advance ratio. The medium pitch propellers will have similar efficiency as high pitch propellers.

The 11×7 reaches error values around 7 at low speeds, but that result comes from propellers 1 to 4, the back propeller at those speeds has a low value of e_F.

From the high pitch propellers, only the smallest presents results as high as the medium pitch pro-

pellers. The high angular speed makes those high radius propellers less efficient.

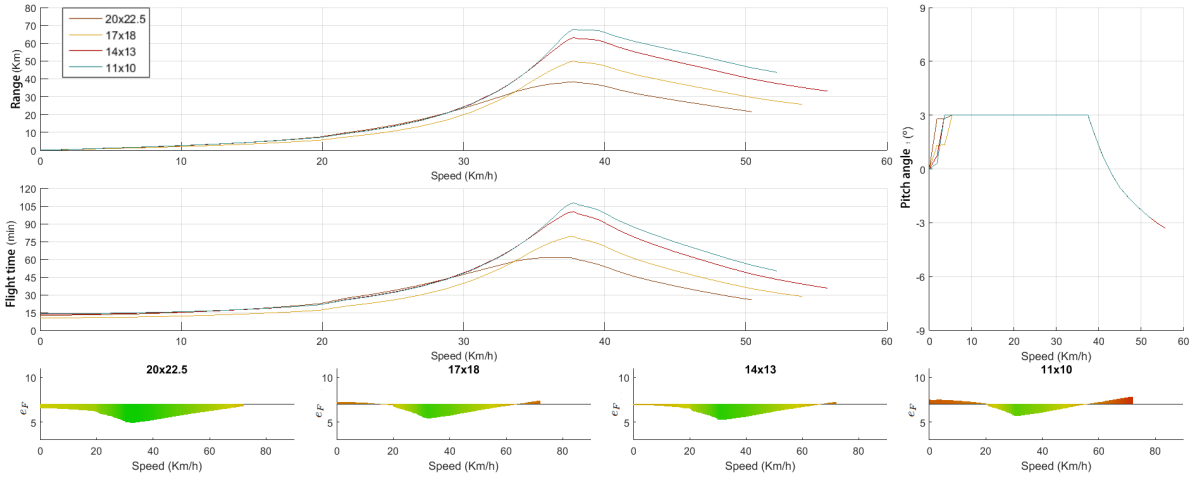

Figure 4.7: Hybrid Plane trim vs airspeed, with medium pitch propellers

The flight time values at Axial flight are also the smallest. And 3 of the propellers are reaching values of e_F higher than 7, the actual flight time in those conditions can be even smaller.

4.3 Conclusion

For the Hybrid Quadrotor, the propellers selected will be the 14×10. They provide range close to the best high pitch propellers, with only a reduction of 25% in flight time at low speeds. And although these vehicles are intended to spend most of the time at high speeds, the time necessary for take-off and landing, and for the transition, will consume a significant part of the battery, so the efficiency at low speeds can not be disregarded. Using the the propeller 14×6 would guarantee the higher efficiency for those operation, but with a reduction of 20% in range.

For the Hybrid Plane, the propellers selected will be the 17×8 for propellers 1 to 4, as it provides the highest efficiency for Axial flight and for the transition. For the 5th propeller, the 14×10. The propeller 11×7 provides best efficiency at high speeds, but 14×10 provide better results for the speeds experienced during the transition. At the point of maximum range the difference between the 2 is negligible.

From these results the conclusion would be that the Hybrid Plane has a higher range than the Hybrid Quadrotor. However, the specifications presented for these vehicles, such as the weight and aerodynamic resistance, while substantiated, are not completely accurate. The maximum ranges differ only around 10%, the difference between real world vehicles and the specifications assumed could be higher than that.

Chapter 5

Control Design

In a quadrotor a simple linear controller, like a PID controller, would be sufficient to govern the vehicle reasonably well, but in these hybrid vehicles the same is not possible. The difference in the vehicle behaviour between Axial flight and Forward flight is too great to use the same control for both. And the transition itself, specially in the case of the Hybrid Quadrotor, moves the vehicle through a very unstable and non-linear regime. As such, a more complex control strategy needs to be adopted.

The solution proposed in this work is not optimised, it was developed to illustrate the feasibility of control.

5.1 Linearization

The linearized system will be presented in State-state representation, as follows:

$$\dot{\boldsymbol{x}} = \boldsymbol{A}\boldsymbol{x} + \boldsymbol{B}\boldsymbol{u} \tag{5.1}$$

where $\boldsymbol{x}$ is state vector, $\boldsymbol{u}$ is the input vector, $\boldsymbol{A}$ the system dynamic matrix, and $\boldsymbol{B}$ the control matrix. For the control, it is assumed there is access to all the states of the vehicles, uncorrupted by noise or sensor errors.

By analysing the vehicle attitude in the trim analysis, we can identify 3 approximately linear regions (fig. 5.1). These will be considered as descriptive of our 3 modes: Axial flight, transition, and Forward flight.

One usual option when using an optimal control design is to start with the Linear-Quadratic Regulator (LQR) controller. The LQR can be used with Multiple Input Multiple Output (MIMO) systems, which is the case, and provides the best performance with respect to a given performance index, with cost J_{cost} equal to:

$$J_{cost}(t) = \int_0^\infty \boldsymbol{x}^{\boldsymbol{T}}\boldsymbol{Q}\boldsymbol{x} + \boldsymbol{u}^{\boldsymbol{T}}\boldsymbol{R}\boldsymbol{u}\ dt \tag{5.2}$$

Where $\boldsymbol{Q}$ and $\boldsymbol{R}$ are positive-definite matrices that determine the importance of the error of each state

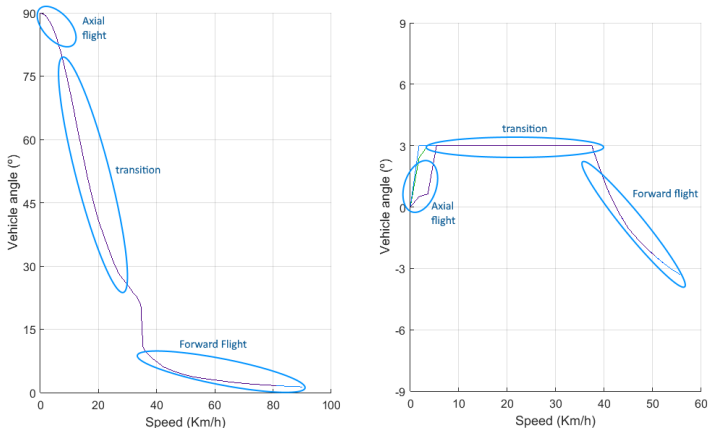

(a) Hybrid Quadrotor (b) Hybrid Plane

Figure 5.1: Pitch Angle for varying airspeed

variable and importance of the inputs.

The matrix gain $\boldsymbol{K}$ results of the minimisation process with the state feedback, obtained as:

$$J_{cost}(t) = \int_0^\infty \boldsymbol{x^T Q x} + \boldsymbol{x^T K^T R K x}\, dt \tag{5.3}$$

By considering a point in each of those regions and its respective trim conditions, an LQR controller may be computed for each region.

But when in a transition between flight modes, the vehicles have to be taken far away from those equilibrium points, specially in the case of the Hybrid Quadrotor. The LQR controller will partially be an obstacle to that end, as it will try to take the system towards the equilibrium conditions. Another problem arises from the fact of using discrete equilibrium points. The reference point for the orientation is considered only with the vehicle oriented with the x_0 direction (fig. 5.2), and not considering all the possible orientations of the vehicle for the same inclination, i.e., with those orientation rotated along z_0. And in the case of the Hybrid Plane, the equilibrium conditions and attitude at start and stopping are very different, even though in both cases the vehicle moves in the same speed ranges.

These problems need to be addressed in the control strategy implemented.

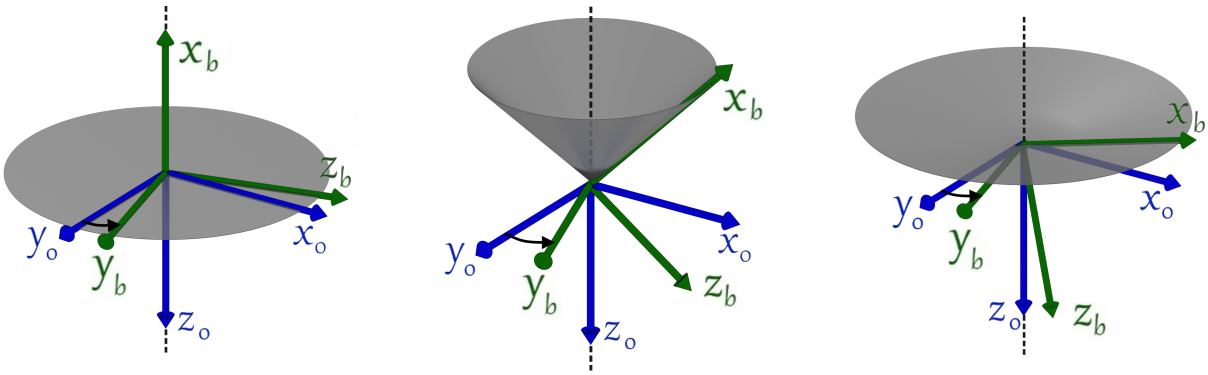

(a) Hybrid Quadrotor Axial flight (b) Hybrid Quadrotor Transition (c) Hybrid Quadrotor Forward flight

Figure 5.2: Possible orientations for the same incidence

5.2 System dynamic and control matrices

Given the complexity of some equations, and the use of look-up tables, the matrices $\boldsymbol{A}$ and $\boldsymbol{B}$ are obtained numerically. To obtain the $\boldsymbol{A}$ matrix, the difference of the output of our system with state variables corresponding to the equilibrium point, $\boldsymbol{x_0}$ and $\boldsymbol{u_0}$, and with the addition a small value in each state variable, $\boldsymbol{x_o} + \boldsymbol{x_i}$ is calculated. That difference, divided by the value added, corresponds to each column of the $\boldsymbol{A}$ matrix (eq. 5.4). In a similar fashion for the $\boldsymbol{B}$ Matrix, by varying the inputs (eq. 5.5).

$$\begin{aligned} \boldsymbol{x_i} =& [0 \quad \underset{1}{\ldots} \quad 0 \quad \underset{i-1}{0.001} \quad \underset{i}{0} \quad \underset{i+1}{\ldots} \quad \underset{n}{0}]^T \\ \boldsymbol{A_{ss}}(:,i) =& \frac{system(\boldsymbol{x_0} + \boldsymbol{x_i}, \boldsymbol{u_0}) - system(\boldsymbol{x_0}, \boldsymbol{u_0})}{0.001} \end{aligned} \tag{5.4}$$

where n is the total number of state variables.

$$\begin{aligned} \boldsymbol{u_i} =& [0 \quad \underset{1}{\ldots} \quad 0 \quad \underset{i-1}{0.001} \quad \underset{i}{0} \quad \underset{i+1}{\ldots} \quad \underset{l}{0}]^T \\ \boldsymbol{B_{ss}}(:,i) =& \frac{system(\boldsymbol{x_0}, \boldsymbol{u_0} + \boldsymbol{u_i},) - system(\boldsymbol{x_0}, \boldsymbol{u_0})}{0.001} \end{aligned} \tag{5.5}$$

where l is the total number of inputs.

For the Hybrid Quardotor three sets of system and control matrices are obtained, one for each mode. For the Hybrid plane we obtain four, two for the Axial flight mode, one for the transition, and one for the Forward flight. The equilibrium conditions, that result in those 2 system matrices for Axial flight, differ in respect to the 5th propeller. For start, it considers the 5th propeller at a high speed, to propel the vehicle forward, while the remaining propellers only provide the lift to keep the vehicle at constant height and orientation. And to stop the vehicle the 5th propeller is stopped, and the movement is totally controlled by the 4 propellers.

As an example, the system and control matrices for the hybrid quadrotor, for Axial flight, are presented in equation 5.6. And for the Hybrid Plane, for Axial flight at start, presented in 5.7. As this is a numerical procedure, it is bound to have numerical errors. Values considered insignificant, 6 orders of magnitude smaller than the maximum for each state variable, were considered as numerical errors, and removed.

A look at those matrices shows for the most part what would be expected. The propellers angular speed affecting the speed in the direction they are aligned with, the relation between the vehicle angular speed and the orientation. It also evidences the influence of the vehicle speeds in the propellers angular acceleration, as a result of the model implemented.

The input for the motors v_{m_i} corresponds to the dimensionless voltage $v_{m_i} = \frac{V_{m_i}}{14.8}$, and is limited between 0.05, to account for the static friction, and 1. The input for the control surfaces is limited between $-0.6\ radians$ and $0.6\ radians$.

$$
\begin{bmatrix} \dot{\boldsymbol{V}}_{\boldsymbol{b}} \\ \hline \dot{\boldsymbol{\omega}}_{\boldsymbol{b}} \\ \hline \dot{\boldsymbol{p}} \\ \hline \dot{\boldsymbol{\eta}} \\ \hline \dot{\Omega}_1 \\ \dot{\Omega}_2 \\ \dot{\Omega}_3 \\ \dot{\Omega}_4 \\ \hline \dot{I}_1 \\ \dot{I}_2 \\ \dot{I}_3 \\ \dot{I}_4 \end{bmatrix} =
\left[\begin{array}{ccc|ccc|ccc|cccc|cccc|cccc}
-0.018 & 0.123 & 0.123 & 0 & 0 & 0 & 0 & 0 & 0 & -13.9 & 0 & -13.9 & 0 & 0.013 & 0.013 & 0.013 & 0.013 & 0 & 0 & 0 & 0 \\
0 & -2.8e^{-4} & 0 & 0 & 0 & 0 & 0 & 0 & 0 & 0 & 13.9 & 0 & 13.9 & 0 & 0 & 0 & 0 & 0 & 0 & 0 & 0 \\
0 & 0 & -0.004 & 0 & 0 & 0 & 0 & 0 & 0 & 0 & -0.2 & -27.9 & 0 & 0 & 0 & 0 & 0 & 0 & 0 & 0 & 0 \\
\hline
0 & 3.9e^{-5} & 0 & -6.4e^{-4} & 0 & -2.6e^{-5} & 0 & 0 & 0 & 0 & 0 & 0 & 0 & 2e^{-3} & -2e^{-3} & 2e^{-3} & -2e^{-3} & 0 & 0 & 0 & 0 \\
0 & 0 & 0.125 & 1e^{-4} & -5.8e^{-5} & -3.3e^{-5} & 0 & 0 & 0 & 0 & 0 & 0 & 0 & 0.2 & -0.2 & -0.2 & 0.2 & 0 & 0 & 0 & 0 \\
0 & -0.024 & 0 & 1e^{-6} & 0 & 0 & 0 & 0 & 0 & 0 & 0 & 0 & 0 & 0.03 & 0.03 & -0.03 & -0.03 & 0 & 0 & 0 & 0 \\
\hline
0 & 0 & 1 & 0 & 0 & 0 & 0 & 0 & 0 & 0 & 0 & 0 & 0 & 0 & 0 & 0 & 0 & 0 & 0 & 0 & 0 \\
0 & 1 & 0 & 0 & 0 & 0 & 0 & 0 & 0 & 0 & 0 & 0 & 0 & 0 & 0 & 0 & 0 & 0 & 0 & 0 & 0 \\
-1 & 0 & 0 & 0 & 0 & 0 & 0 & 0 & 0 & 0 & 0 & 0 & 0 & 0 & 0 & 0 & 0 & 0 & 0 & 0 & 0 \\
\hline
0 & 0 & 0 & 0 & -0.354 & 0 & 0 & 0 & 0 & -1.02 & -7e^{-3} & -1 & -7e^{-3} & 0 & 0 & 0 & 0 & 0 & 0 & 0 & 0 \\
0 & 0 & 0 & 0.354 & 0 & 0.354 & 0 & 0 & 0 & 0 & -1e^{-4} & 0 & 0 & 0 & 0 & 0 & 0 & 0 & 0 & 0 & 0 \\
0 & 0 & 0 & 0 & 0.354 & 0 & 0 & 0 & 0 & -1 & -7e^{-3} & -1.02 & -7e^{-3} & 0 & 0 & 0 & 0 & 0 & 0 & 0 & 0 \\
0 & 0 & 0 & -0.354 & 0 & 0.354 & 0 & 0 & 0 & 0 & 0 & 0 & -1e^{-4} & 0 & 0 & 0 & 0 & 0 & 0 & 0 & 0 \\
\hline
-549 & -85.5 & -85.5 & 0 & 0 & 0 & 0 & 0 & 0 & 0 & 0 & 0 & 0 & -119 & 0 & 0 & 0 & 1060 & 0 & 0 & 0 \\
-549 & -85.5 & -85.5 & 0 & 0 & 0 & 0 & 0 & 0 & 0 & 0 & 0 & 0 & 0 & -119 & 0 & 0 & 0 & 1060 & 0 & 0 \\
-549 & -85.5 & -85.5 & 0 & 0 & 0 & 0 & 0 & 0 & 0 & 0 & 0 & 0 & 0 & 0 & -119 & 0 & 0 & 0 & 1060 & 0 \\
-549 & -85.5 & -85.5 & 0 & 0 & 0 & 0 & 0 & 0 & 0 & 0 & 0 & 0 & 0 & 0 & 0 & -119 & 0 & 0 & 0 & 1060 \\
\hline
0 & 0 & 0 & 0 & 0 & 0 & 0 & 0 & 0 & 0 & 0 & 0 & 0 & -11.4 & 0 & 0 & 0 & -153 & 0 & 0 & 0 \\
0 & 0 & 0 & 0 & 0 & 0 & 0 & 0 & 0 & 0 & 0 & 0 & 0 & 0 & -11.4 & 0 & 0 & 0 & -153 & 0 & 0 \\
0 & 0 & 0 & 0 & 0 & 0 & 0 & 0 & 0 & 0 & 0 & 0 & 0 & 0 & 0 & -11.4 & 0 & 0 & 0 & -153 & 0 \\
0 & 0 & 0 & 0 & 0 & 0 & 0 & 0 & 0 & 0 & 0 & 0 & 0 & 0 & 0 & 0 & -11.4 & 0 & 0 & 0 & -153
\end{array}\right]
\begin{bmatrix} \boldsymbol{V_b} \\ \hline \boldsymbol{\omega_b} \\ \hline \boldsymbol{p} \\ \hline \boldsymbol{\eta} \\ \hline \Omega_1 \\ \Omega_2 \\ \Omega_3 \\ \Omega_4 \\ \hline I_1 \\ I_2 \\ I_3 \\ I_4 \end{bmatrix} +
\left[\begin{array}{cccc}
0 & 0 & 0 & 0 \\ 0 & 0 & 0 & 0 \\ 0 & 0 & 0 & 0 \\ \hline
0 & 0 & 0 & 0 \\ 0 & 0 & 0 & 0 \\ 0 & 0 & 0 & 0 \\ \hline
0 & 0 & 0 & 0 \\ 0 & 0 & 0 & 0 \\ 0 & 0 & 0 & 0 \\ \hline
0 & 0 & 0 & 0 \\ 0 & 0 & 0 & 0 \\ 0 & 0 & 0 & 0 \\ 0 & 0 & 0 & 0 \\ \hline
0 & 0 & 0 & 0 \\ 0 & 0 & 0 & 0 \\ 0 & 0 & 0 & 0 \\ 0 & 0 & 0 & 0 \\ \hline
1345 & 0 & 0 & 0 \\ 0 & 1345 & 0 & 0 \\ 0 & 0 & 1345 & 0 \\ 0 & 0 & 0 & 1345
\end{array}\right]
\begin{bmatrix} v_{m_1} \\ v_{m_2} \\ v_{m_3} \\ v_{m_4} \end{bmatrix}
\qquad (5.6)
$$

$$
\begin{bmatrix} \dot{\boldsymbol{V}}_{\boldsymbol{b}} \\ \hline \dot{\boldsymbol{\omega}}_{\boldsymbol{b}} \\ \hline \dot{\boldsymbol{p}} \\ \hline \dot{\boldsymbol{\eta}} \\ \hline \dot{\Omega}_1 \\ \dot{\Omega}_2 \\ \dot{\Omega}_3 \\ \dot{\Omega}_4 \\ \dot{\Omega}_5 \\ \hline \dot{I}_1 \\ \dot{I}_2 \\ \dot{I}_3 \\ \dot{I}_4 \\ \dot{I}_5 \\ \hline \dot{\delta}_1 \\ \dot{\delta}_4 \\ \dot{\delta}_5 \\ \dot{\delta}_6 \end{bmatrix} =
\left[\begin{array}{ccc|ccc|ccc|cccc|cccc|cccc}
-0.046 & 0.03 & 0.03 & 0 & 0 & 0 & 0\,0\,0 & 0 & 0 & -19.6 & 0 & 0 & 0 & 0 & 0 & 0.013 & 0 & 0 & 0 & 0 & 0 & 0 & 0 & 0 & 0 \\
0 & 0 & 0 & 0 & 0 & 0 & 0\,0\,0 & 0 & 19.6 & 0 & 0 & 0 & 0 & 0 & 0 & 0 & 0 & 0 & 0 & 0 & 0 & 0 & 0 & 0 & 0 \\
-0.113 & -0.113 & -0.263 & 0 & 0 & 0 & 0\,0\,0 & 0 & -0.02 & -0.02 & 0 & -0.015 & -0.015 & -0.015 & -0.015 & 0 & 0 & 0 & 0 & 0 & 0 & 0 & 0 & 0 & 0 \\
\hline
-0.018 & -0.21 & -3e^{-3} & 0 & 0 & 0 & 0\,0\,0 & 0 & 0 & 0 & 0 & 0.06 & 0.062 & -0.06 & -0.062 & -3e^{-3} & 0 & 0 & 0 & 0 & 0 & 0 & 0 & 0 & 0 \\
0.225 & -0.072 & 4e^{-3} & 0 & 0 & 0 & 0\,0\,0 & 0 & 0 & 0 & 0 & 0.082 & -0.084 & -0.082 & 0.082 & 0 & 0 & 0 & 0 & 0 & 0 & 0 & 0 & 0 & 0 \\
-5.6e^{-3} & -4e^{-3} & -3.6e^{-3} & 0 & 0 & 0 & 0\,0\,0 & 0 & 0 & 0 & 0 & -4e^{-3} & 4e^{-3} & 0 & 0 & 0 & 0 & 0 & 0 & 0 & 0 & 0 & 0 & 0 & 0 \\
\hline
1 & 0 & 0 & 0 & 0 & 0 & 0\,0\,0 & 0 & 0 & 0 & 0 & 0 & 0 & 1 & 0 & 0 & 0 & 0 & 0 & 0 & 0 & 0 & 0 & 0 & 0 \\
0 & 1 & 0 & 0 & 0 & 0 & 0\,0\,0 & 0 & 0 & 0 & 0 & 0 & 0 & 0 & 0 & 0 & 0 & 0 & 0 & 0 & 0 & 0 & 0 & 0 & 0 \\
0 & 0 & 1 & 0 & 0 & 0 & 0\,0\,0 & 0 & 0 & 0 & 0 & 0 & 0 & 0 & 0 & 0 & 0 & 0 & 0 & 0 & 0 & 0 & 0 & 0 & 0 \\
\hline
0 & 0 & 0 & 0 & 0 & 0 & 0\,0\,0 & -2 & -1e^{-3} & -1e^{-3} & -1e^{-3} & 0 & 0 & 0 & 0 & 0 & 0 & 0 & 0 & 0 & 0 & 0 & 0 & 0 & 0 \\
0 & 0 & 0 & 0.5 & 0 & 0 & 0\,0\,0 & 0 & -1e^{-6} & 0 & 0 & 0 & 0 & 0 & 0 & 0 & 0 & 0 & 0 & 0 & 0 & 0 & 0 & 0 & 0 \\
0 & 0 & 0 & 0 & 0.5 & 0 & 0\,0\,0 & 0 & 0 & -1e^{-6} & & 0 & 0 & 0 & 0 & 0 & 0 & 0 & 0 & 0 & 0 & 0 & 0 & 0 & 0 \\
0 & 0 & 0 & 0 & 0 & 0.5 & 0\,0\,0 & 0 & 0 & 0 & -1e^{-6} & 0 & 0 & 0 & 0 & 0 & 0 & 0 & 0 & 0 & 0 & 0 & 0 & 0 & 0 \\
\hline
-120 & -120 & 600 & 0 & 0 & 0 & 0\,0\,0 & 0 & 0 & 0 & 0 & -168 & 0 & 0 & 0 & 0 & 1060 & 0 & 0 & 0 & 0 & 0 & 0 & 0 & 0 \\
-120 & -120 & 600 & 0 & 0 & 0 & 0\,0\,0 & 0 & 0 & 0 & 0 & 0 & -168 & 0 & 0 & 0 & 0 & 1060 & 0 & 0 & 0 & 0 & 0 & 0 & 0 \\
-120 & -120 & 600 & 0 & 0 & 0 & 0\,0\,0 & 0 & 0 & 0 & 0 & 0 & 0 & -168 & 0 & 0 & 0 & 0 & 1060 & 0 & 0 & 0 & 0 & 0 & 0 \\
-120 & -120 & 600 & 0 & 0 & 0 & 0\,0\,0 & 0 & 0 & 0 & 0 & 0 & 0 & 0 & -168 & 0 & 0 & 0 & 0 & 1060 & 0 & 0 & 0 & 0 & 0 \\
-695 & -109 & -109 & 0 & 0 & 0 & 0\,0\,0 & 0 & 0 & 0 & 0 & 0 & 0 & 0 & 0 & -148 & 0 & 0 & 0 & 0 & 1060 & 0 & 0 & 0 & 0 \\
\hline
0 & 0 & 0 & 0 & 0 & 0 & 0\,0\,0 & 0 & 0 & 0 & 0 & -11.4 & 0 & 0 & 0 & 0 & -153 & 0 & 0 & 0 & 0 & 0 & 0 & 0 & 0 \\
0 & 0 & 0 & 0 & 0 & 0 & 0\,0\,0 & 0 & 0 & 0 & 0 & 0 & -11.4 & 0 & 0 & 0 & 0 & -153 & 0 & 0 & 0 & 0 & 0 & 0 & 0 \\
0 & 0 & 0 & 0 & 0 & 0 & 0\,0\,0 & 0 & 0 & 0 & 0 & 0 & 0 & -11.4 & 0 & 0 & 0 & 0 & -153 & 0 & 0 & 0 & 0 & 0 & 0 \\
0 & 0 & 0 & 0 & 0 & 0 & 0\,0\,0 & 0 & 0 & 0 & 0 & 0 & 0 & 0 & -11.4 & 0 & 0 & 0 & 0 & -153 & 0 & 0 & 0 & 0 & 0 \\
0 & 0 & 0 & 0 & 0 & 0 & 0\,0\,0 & 0 & 0 & 0 & 0 & 0 & 0 & 0 & 0 & -11.4 & 0 & 0 & 0 & 0 & -153 & 0 & 0 & 0 & 0 \\
\hline
0 & 0 & 0 & 0 & 0 & 0 & 0\,0\,0 & 0 & 0 & 0 & 0 & 0 & 0 & 0 & 0 & 0 & 0 & 0 & 0 & 0 & 0 & -1000 & 0 & 0 & 0 \\
0 & 0 & 0 & 0 & 0 & 0 & 0\,0\,0 & 0 & 0 & 0 & 0 & 0 & 0 & 0 & 0 & 0 & 0 & 0 & 0 & 0 & 0 & 0 & -1000 & 0 & 0 \\
0 & 0 & 0 & 0 & 0 & 0 & 0\,0\,0 & 0 & 0 & 0 & 0 & 0 & 0 & 0 & 0 & 0 & 0 & 0 & 0 & 0 & 0 & 0 & 0 & -1000 & 0 \\
0 & 0 & 0 & 0 & 0 & 0 & 0\,0\,0 & 0 & 0 & 0 & 0 & 0 & 0 & 0 & 0 & 0 & 0 & 0 & 0 & 0 & 0 & 0 & 0 & 0 & -1000
\end{array}\right]
\begin{bmatrix} \boldsymbol{V_b} \\ \hline \boldsymbol{\omega_b} \\ \hline \boldsymbol{p} \\ \hline \boldsymbol{\eta} \\ \hline \Omega_1 \\ \Omega_2 \\ \Omega_3 \\ \Omega_4 \\ \Omega_5 \\ \hline I_1 \\ I_2 \\ I_3 \\ I_4 \\ I_5 \\ \hline \delta_1 \\ \delta_4 \\ \delta_5 \\ \delta_6 \end{bmatrix} +
\left[\begin{array}{ccccc}
0 & 0 & 0 & 0 & 0 \\ 0 & 0 & 0 & 0 & 0 \\ 0 & 0 & 0 & 0 & 0 \\ \hline
0 & 0 & 0 & 0 & 0 \\ 0 & 0 & 0 & 0 & 0 \\ 0 & 0 & 0 & 0 & 0 \\ \hline
0 & 0 & 0 & 0 & 0 \\ 0 & 0 & 0 & 0 & 0 \\ 0 & 0 & 0 & 0 & 0 \\ \hline
0 & 0 & 0 & 0 & 0 \\ 0 & 0 & 0 & 0 & 0 \\ 0 & 0 & 0 & 0 & 0 \\ 0 & 0 & 0 & 0 & 0 \\ \hline
0 & 0 & 0 & 0 & 0 \\ 0 & 0 & 0 & 0 & 0 \\ 0 & 0 & 0 & 0 & 0 \\ 0 & 0 & 0 & 0 & 0 \\ \hline
1345 & 0 & 0 & 0 & 0 \\ 0 & 1345 & 0 & 0 & 0 \\ 0 & 0 & 1345 & 0 & 0 \\ 0 & 0 & 0 & 1345 & 0 \\ 0 & 0 & 0 & 0 & 1345 \\ \hline
0 & 0 & 0 & 0 & 0 \\ 0 & 0 & 0 & 0 & 0 \\ 0 & 0 & 0 & 0 & 0 \\ 0 & 0 & 0 & 0 & 0
\end{array}\right]
\begin{bmatrix} Vm_1 \\ Vm_2 \\ Vm_3 \\ Vm_4 \\ Vm_5 \\ \hline \delta_{r_1} \\ \delta_{r_4} \\ \delta_{r_5} \\ \delta_{r_6} \end{bmatrix}
$$

(5.7)

With the system dynamic and control matrices, we obtain the control matrices using the *lqr* function from Matlab^{TM}. For the Hybrid Quadrotor, two matrices from the Axial flight system matrix are obtained, by using two different Q matrices. One for the start, to enable an easy transition between modes, and other to stop, to guarantee a more stable stop. From the transition and Forward flight system matrices one control matrix is obtained for each. In the case of the Hybrid Plane one control matrix is obtained from each of the four system matrices.

Those matrices however, as they are purely a mathematical result, do not take into consideration more practical considerations, such as how an aircraft is controlled through control surfaces. As an example, to roll an airplane, only the ailerons are actuated, but the controller obtained would provide actuation from all control surfaces, as it minimises the actuation of the inputs.

The study area of control allocation addresses that problem [36]. With more and more complex aircrafts, with redundant actuation systems for manoeuvrability and reliability, there is increased studies on that subject. Recurring to optimisation strategies such as linear programing and meta-heuristics, it is possible to optimise the use of the control surfaces available. However, in this work, the control allocation will be performed recurring to expert knowledge, and the control matrices will be simply modified manually to obtain the desired actuation response as used in traditional airplanes.

Also, as a result of the numerical procedure, small errors occur in the system matrices, resulting in uneven control actions. As an example, to rotate the Hybrid Quadrotor, the best actuation would be to provide a symmetric actuation to the propellers, but the control matrix obtained gives an uneven actuation for the propellers. Those errors are corrected manually.

5.3 Control block diagram

The control strategy proposed in this work is composed of 3 levels (fig. 5.3).

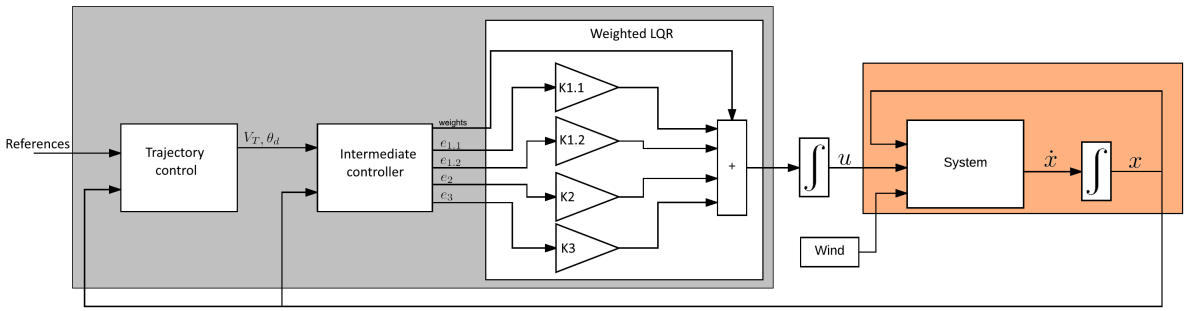

Figure 5.3: Control strategy plant

In the inner loop, Weighted LQR, there are four LQR matrices (**K1.1, K1.2**, **K2**, **K3**), pondered by coefficients depending on the air speed and distance to target, presented in figure 5.4.

In the controller for both vehicles, a distance of 20 meters was set as the limit from target to change the type of flight. If the vehicle is located further than that distance from the target it will transition to Forward flight, and use **K1.1** for Axial flight control. As it reaches that distance it will start to transition to

axial flight, and when reaching the speed threshold for Axial flight, use matrix **K1.2**. If the vehicle starts already at less than 20m it will never transition to Forward flight, using control matrix **K1.2**.

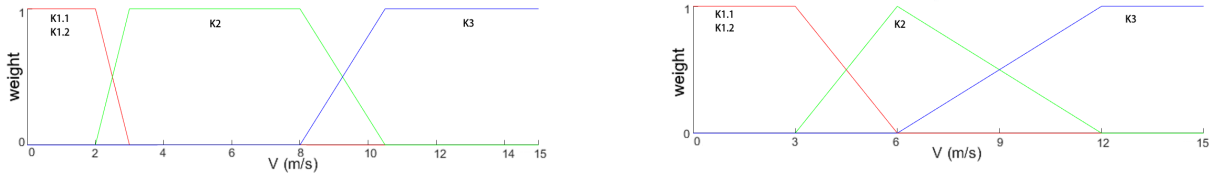

(a) Hybrid Quadrotor Axial flight

(b) Hybrid Quadrotor transition

Figure 5.4: Control Weights

In the outer loop, the controller takes the desired position and calculates the desired speed V_T and orientation. The maximum desired speed is considered $13m/s$ for both vehicles, to keep them working not far from the maximum efficiency. The demanded attitude is limited to a maximum offset of $\frac{\pi}{16}\ radians$ from the current attitude. Due to the unitary nature of quaternions, with a big difference in one of the entries, the others will also be affected in value, leading to a false actuation.

In the intermediate controller level, the state is subtracted to the references obtaining the feedback error:

$$\boldsymbol{e_i} = \boldsymbol{x_{ref_i}} - \boldsymbol{x} \quad , \quad i = [1.1 \;\; 1.2 \;\; 2 \;\; 3] \tag{5.8}$$

Where $\boldsymbol{e_i}$ is the state space reference vector for each controller, and $\boldsymbol{x_{ref_i}}$ the state space reference vector for each control matrix (**K1.1**, **K1.2**, **K2**, **K3**) .

But some corrections are made to respond to the problems identified.

The terms related to the speed error are altered, to help the vehicle change controllers, and provide a smother transition.

$$\begin{aligned} e_{1.1}(3) &= V_b(3) - Vref_i(3) + min(max(V_T - V_b(3), -3), 3) \\ e_2(1) &= V_b(1) - Vref_i(1) + min(max(V_T - V_b(1), -3), 3) \\ e_3(1) &= V_b(1) - Vref_i(1) + min(max(V_T - V_b(1), -3), 3) \end{aligned} \tag{5.9}$$

To obtain the correct quaternion reference, for the case the vehicle is not oriented with the x_0 direction, the current angle θ_a is obtained, and the reference quaternion rotated of that angle. To give reference of the desired orientation, the angle between the reference direction and the current orientation θ_d. It is also considered that the vehicles will only rotate after entering Forward flight, as such, only the orientation reference for the Forward flight orientation will be altered with that angle.

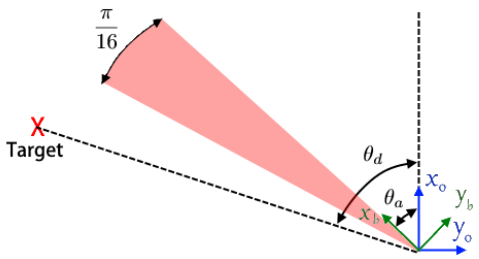

Figure 5.5: Orientation transformation

$$a_{r_i} = \theta_a \quad , i = [1.1 \;\; 1.2 \;\; 2] \quad , \qquad a_{r_3} = \theta_a + min\left(max\left(\theta_d - \theta_a, -\frac{\pi}{16}\right), \frac{\pi}{16}\right)$$

$$\boldsymbol{q} = \begin{bmatrix} \sqrt{1 - sin(\frac{a_{r_i}}{2})^2} \\ 0 \\ 0 \\ sin(\frac{a_{r_i}}{2})^2 \end{bmatrix} \quad , \quad \boldsymbol{\eta_{ref\ i}} = \begin{bmatrix} q_0 & -q_1 & -q_2 & -q_3 \\ q_1 & q_0 & -q_3 & q_2 \\ q_2 & q_3 & q_0 & -q_1 \\ q_3 & -q_2 & q_1 & q_0 \end{bmatrix} \boldsymbol{\eta_{ref\ i}} \tag{5.10}$$

5.4 Hybrid Quadrotor Results

5.4.1 Axial flight

Testing the control strategy implemented in conditions of wind shows good results in stability, with some stationary error.

Wind with speed of $1m/s$ was introduced in all three directions, by stages, as illustrated in figure 5.6(a).

Wind in the x_0 direction, corresponding to the vehicle z_b direction, affects the vehicle the most. That direction is normal to the wing, and offers the most aerodynamic resistance, requiring the most input action (fig. 5.6(b)) to compensate the drag caused.

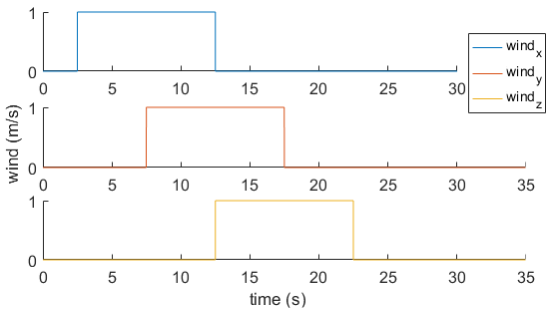

(a) Wind input

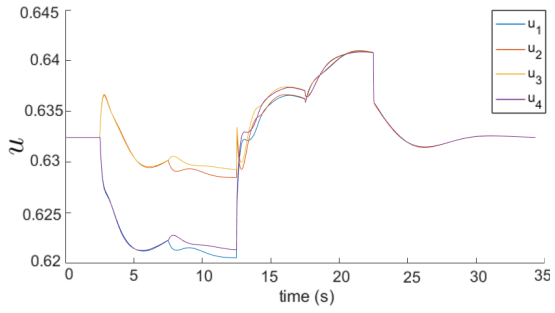

(b) Motor input actuation

Figure 5.6: Axial flight response wind disturbance

The wind speed along y_b causes only a small disturbance, after 7.5s there is a small separation between inputs 1 and 4, and 2 and 3, that is responsible for that compensation.

This is also visible in the vehicle speed (fig. 5.7(a)) and position(fig. 5.7(b)).

The wind along x_0 not only causes a speed in V_z, and consequently a change in position x_0, but also a speed in V_x due to the wing. To compensate the movement in x_0 the vehicle will tilt, in the direction of the wind, and the wing at that angle of attack will generate lift, pushing the vehicle upwards. There is also some movement in y_b, as a result of small unbalances in the moments generated by the propellers, small changes in the control matrices values, and other numerical errors.

The wind speed in z_0 pushes the vehicle downwards, and the controller responds by increasing the rotation of all propellers. It can also be seen that, after the wind in y_0 is removed, there is an increase in the vehicle speed in V_{b_x} and corresponding actuation. As noted before, airspeed lateral to the propeller increases slightly the thrust generated, and as that component of the wind is removed the thrust generated by the propellers is reduced.

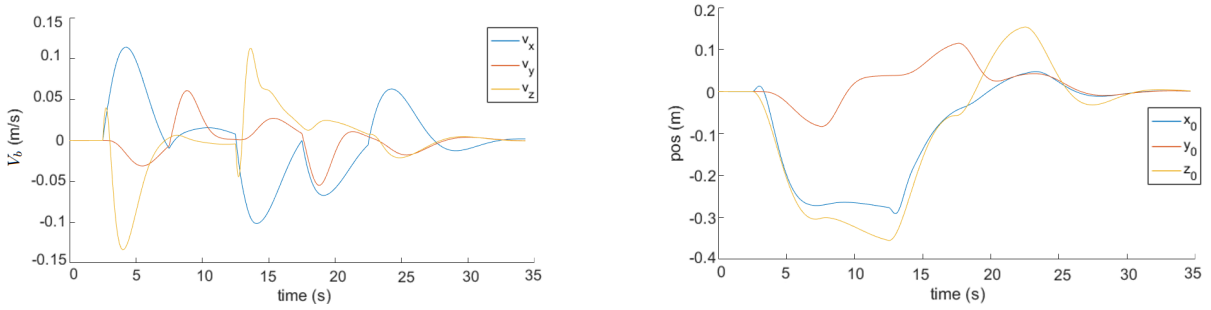

(a) Vehicle speed

(b) Vehicle position

Figure 5.7: Hybrid Quadrotor speed and position

The change in the vehicle orientation is rather small, the major variation in angular speed (fig. 5.8(a)) is along the axis y_b. The vehicle also rotates along z_b, specially when wind is introduced in y_0. The orientation (fig. 5.8(b)) also shows a major change in the 3rd term, related to the rotation along y_b.

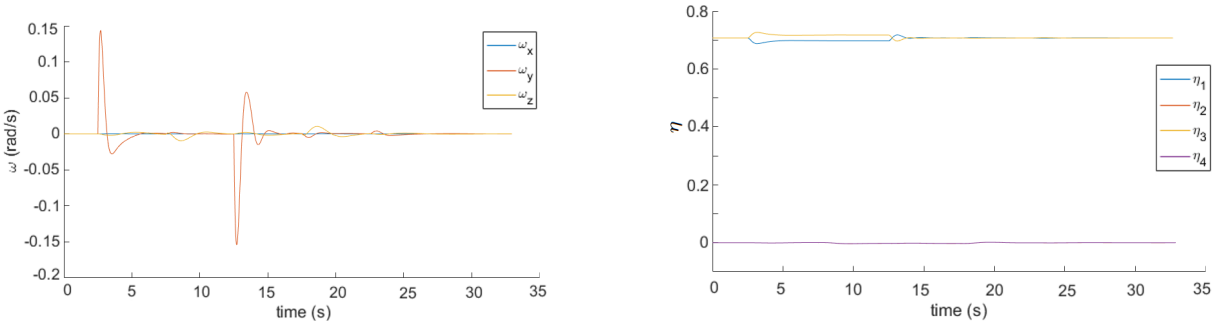

(a) Vehicle angular speed

(b) Vehicle orientation

Figure 5.8: Hybrid Quadrotor angular speed and orientation

The propeller angular speed (fig.5.9(a)) and motor current (fig. 5.9(b)) are closely related to the input actuation, which corresponds to the motor voltage. For the most part they display similar behaviour, but when changing wind speed in z_0 the differences are evident. Wind speed in z_0 corresponds to air speed in the axial direction of the propeller, which have a significant impact in their performance. At 12.5s, when introducing wind speed in that direction, there is a decrease in the propellers angular speed, as a result of the increased torque and current. The controller responds by increasing the input, witch also

causes a further increase in current.

At 22.5s the opposite occurs. Removing the wind speed causes the propeller to gain angular speed. It is also visible in both cases that, while the control action and current variation occur very quickly, the change in angular speed is smoother, as a result of the inertia and drag of the propeller.

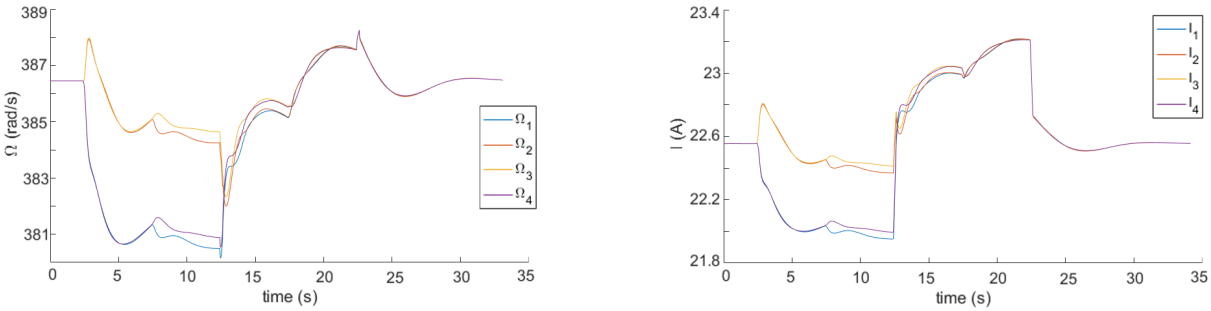

(a) Propeller angular speed

(b) Motor current

Figure 5.9: Propeller and motor state

5.4.2 Aerodinamic flight

In Forward flight wind was introduced in the same way as for Axial flight, but with a value of $5m/s$ (fig. 5.10(a)).

From the motor input (fig. 5.10(b)), some instability and oscillation are visible when the wind takes effect. This occurs in good part due to the irregularities in the profiles used to model the wing lift, drag and moment coefficients.

In this configuration, the direction normal to the wing z_b is aligned with z_0, and the result is a greater control action to compensate the wind in that direction.

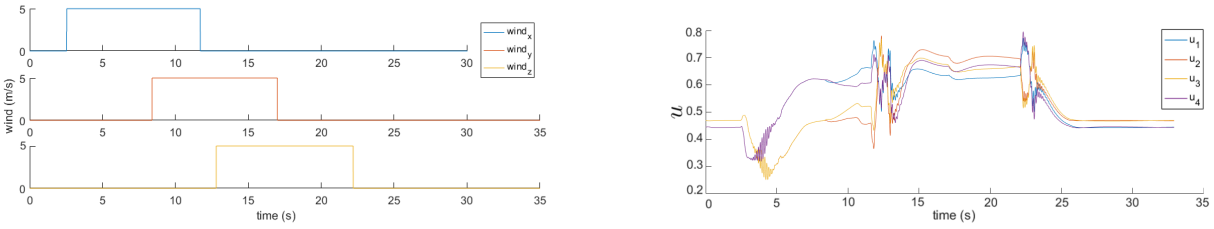

(a) Wind

(b) Motor input actuation

Figure 5.10: Response to wind disturbance in Forward flight

With wind speed along x_0 there is an increase in the vehicle speed, as the wind is pushing the vehicle forward. However, this reduces the wing lift, making the vehicle to fall and increase v_{bz}, as seen in figure 5.11(a). As a result, the control will provide more action to the propellers 1 and 4, to increase their thrust. This will rotate the vehicle backwards (fig. 5.11(b)), and make the axis z_b partially aligned with the direction of movement. This is the reason why the vehicle has a relatively high speed along z_b, but stops falling at around 8s (fig 5.11(b)).

As the wind in the x_0 direction is removed the wing regains a lot of lift and pitching moment, causing a spike in the vehicle orientation and regaining most of the altitude lost.

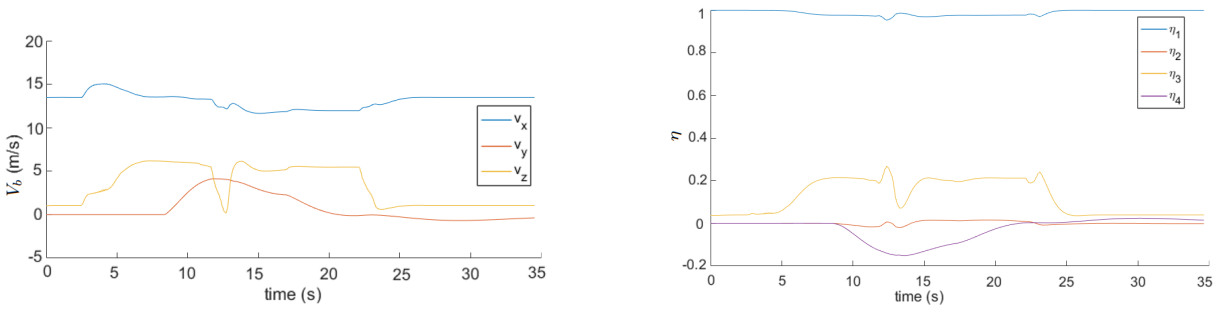

(a) Vehicle speed

(b) Vehicle orientation

Figure 5.11: Hybrid Quadrotor speed and orientation

Wind in the z_0 direction also causes the vehicle to fall, and the vehicle compensated by rotating backwards.

As the wind is completely removed, the vehicle converges to its equilibrium conditions of speed and orientation. The error in position y_b is expected, as the control does not directly considers it.

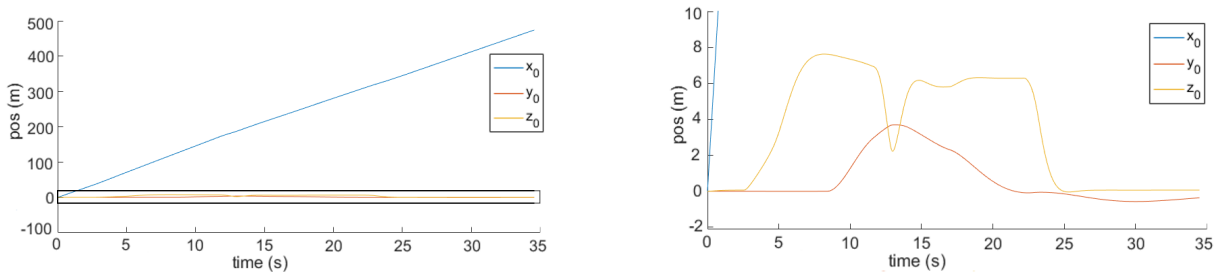

(a) Vehicle Position

(b) Detailed y_0 and z_0 position

Figure 5.12: Hybrid Quadrotor position

5.4.3 Complete flight

Performing a complete flight, from Axial flight to Forward flight and from Forward flight back to Axial flight, some oscillations appear, that were expected due to the use of discrete curves with irregularities for the wings coefficients. The controllers are also in part responsible for the small oscillations, as they need to allow the vehicle to move away from the equilibrium position to transition to the next controller.

The vehicle starts at position $[NED] = [0\ 0\ 0]$, with z_b oriented with x_0 (fig. 5.14(b)). The target point is $[10\ \ -150\ 0]$, with no fixed orientation.

As the vehicle transitions from Axial flight to Forward flight it quickly gains forward speed (fig. 5.13(b)) and transitions to Forward flight attitude. This fast transition is obtained by maxing out the motors, as visible in figure 5.13(a) at around 2s.

As the vehicle reaches Forward flight attitude, it will start to turn towards the desired point. The controller allows for a significant side-slip, due to the maximum banking allowed for the vehicle being rather small, performing the curve with a radius of around $30m$.

During the final part of the flight, it does overshoot the target position (fig. 5.21), due to its high linear

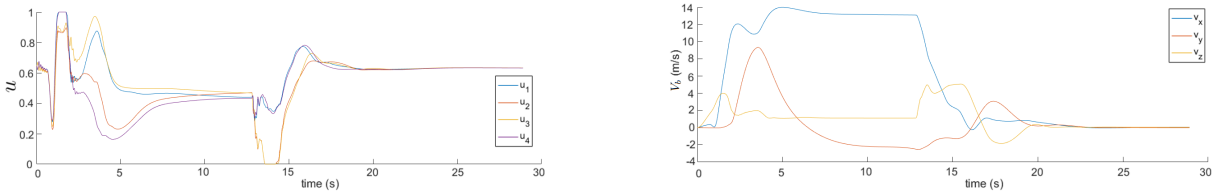

(a) Motor input action

(b) Vehicle speed

Figure 5.13: Hybrid Quadrotor actuation and speed

momentum, but it is capable of compensating it and move to the desired position.

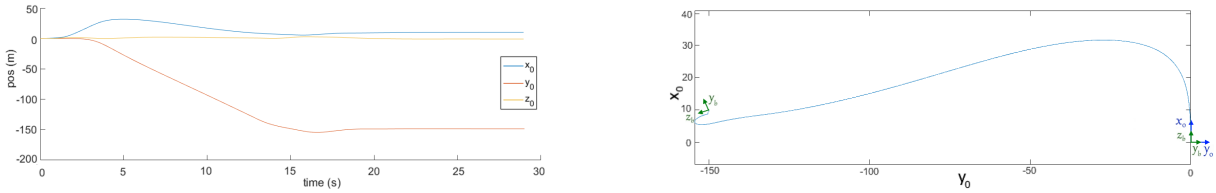

(a) Vehicle position vs time

(b) Vehicle trajectory (top view), and orientation

Figure 5.14: Hybrid Quadrotor position

5.5 Hybrid Plane Results

5.5.1 Axial flight

For the hybrid plane, wind of $1\ m/s$ was introduced, in the same way as for the Hybrid Quadrotor (fig. 5.6(a)).

In Axial flight only propeller 1 to 4 will be actuated, the 5th propeller and the control surfaces will not be actuated. The wind component in the x_0 direction shows a very small response from the controller, as both the speed and position are not greatly affected. The vehicle has a small aerodynamic resistance int the direction x_b, and consequently small drag force.

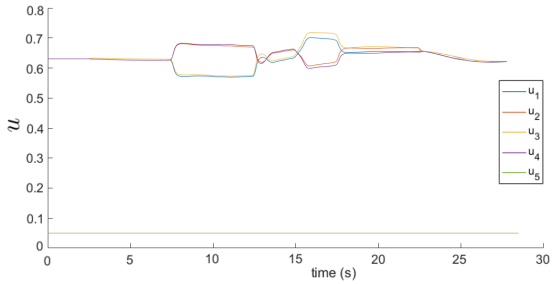

Figure 5.15: Motor input actuation

Wind in z_0, corresponding to the vehicles z_b causes the largest disturbance, as it corresponds to the direction normal to the wing.

The wind in the y_0 direction also causes disturbances in the other directions, mainly due to the aerodynamic structure in the tail, rotating the vehicle.

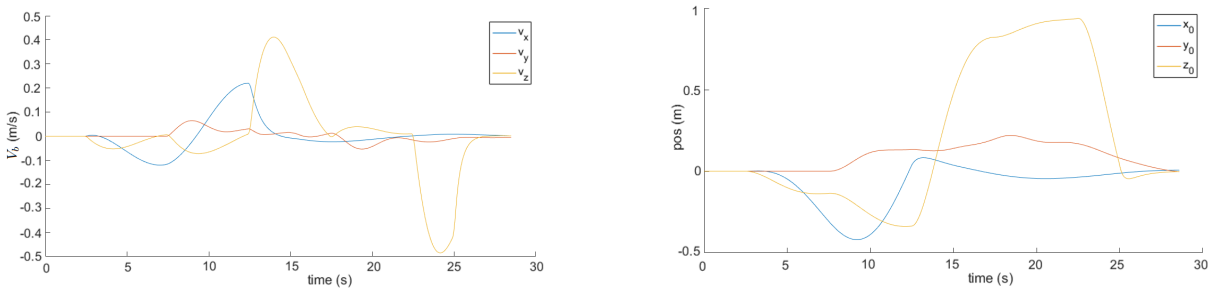

(a) Vehicle speed

(b) Vehicle position

Figure 5.16: Hybrid Plane speed and position

5.5.2 Forward flight

For the Forward flight test of the Hybrid Plane the wind speed was considered at $1\ m/s$, instead of the $5\ m/s$ used for the Hybrid Quadrotor. The control strategy used, in the case of the Hybrid Plane, was found to be more sensitive to the effects of external disturbances, specially in the x_b direction. Wind with a value of $5\ m/s$ in that direction drastically reduces the lift generated by the wing, and as the use of the propellers 1 to 4 is being controlled as function of the vehicle speed, they will not be activated, and the vehicle will simply fall. In the case of the Hybrid Quadrotor, it compensates the wing lift loss with the propellers, as they are always active.

As the vehicle rotates to compensate the orientation error the wind, in the y_b direction will have a component along $-x_b$, slowing the vehicle (fig. 5.20). This causes the propellers 1 to 4 to activate (fig. 5.17(a)), as it reaches speed speed below $12\ m/s$, corresponding to the transition between controllers (fig. 5.4(b)).

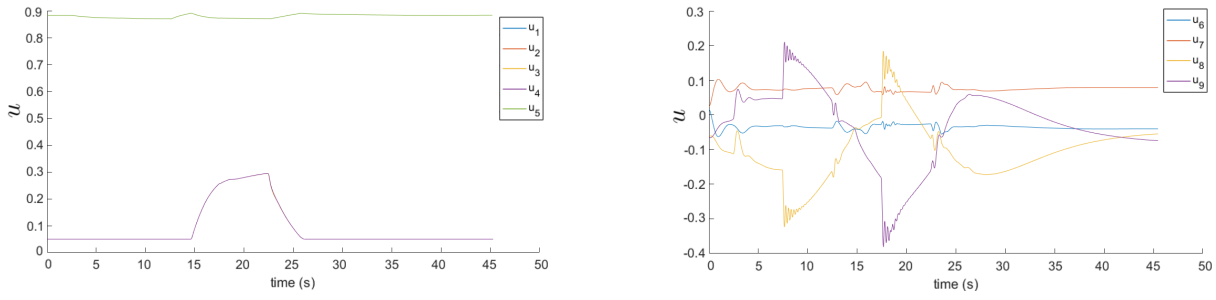

(a) Propeller input actuation

(b) Control surfaces input actuation

Figure 5.17: Input actuation

The control surfaces display some oscillatory behaviour, as a result of the irregularities in the look-up tables. But even so, the controller manages to stabilise the flight in the presence of wind.

After the removal of wind, the vehicle returns to its equilibrium conditions speed, although it takes more time than the Hybrid Quadrotor to do so.

The position in both y_0 and z_0 slowly return to zero, as the vehicle moves forward.

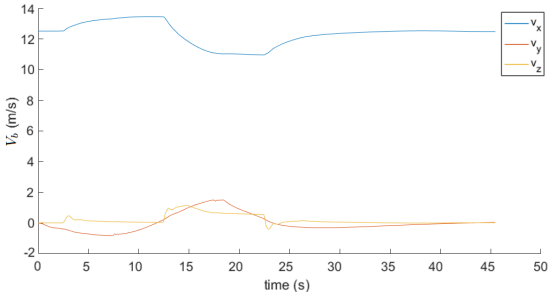

(a) Vehicle speed

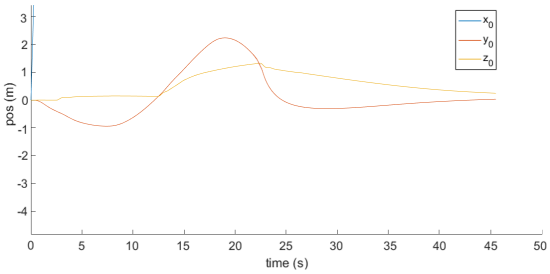

(b) Detailed y_0 and z_0 position

Figure 5.18: Hybrid Plane position

5.5.3 Complete flight

The vehicle starts at $[0\ 0\ 0]$, with x_b oriented with x_0(fig. 5.14(b)). The target point is $[10\ -400\ 0]$, with no fixed orientation.

The Hybrid Plane, with the implemented controller, can not perform a curve with a radius as small as the Hybrid Quadrotor, the target point was considered at a larger distance to allow the vehicle to perform the turn.

At start, the 5th propellers it actuated to near its maximum (fig. 5.19(a)), to quickly increase the vehicle air speed (fig. 5.20). As it gains speed the other 4 propellers have their actuation reduced, until they reach the minimum and the propellers stop.

As the vehicle reaches the 20m mark from the target position the controller cuts off the back the 5th propeller, and activates the others for a quick deceleration.

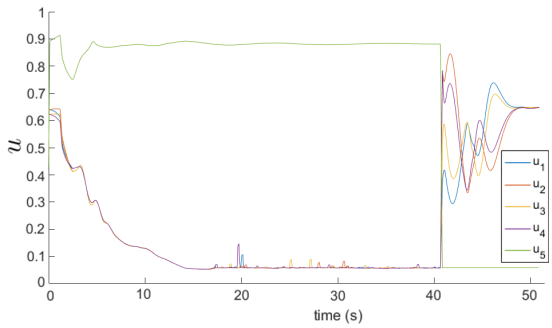

(a) Propeller input actuation

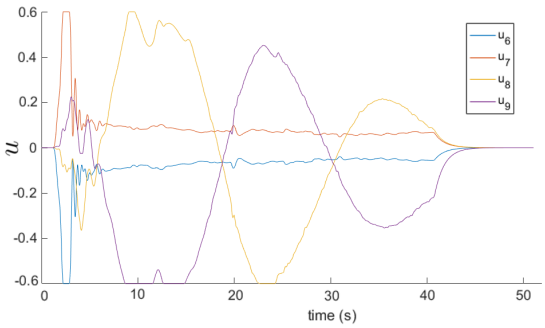

(b) Control surfaces input actuation

Figure 5.19: Input actuation

The control surfaces (fig. 5.19(b)) are only activated with the controllers K2 an K3, after the vehicle passes the $3\ m/s$ barrier. At low speeds their actuation quickly saturates, as the forces generated are small.

The speed V_x is keep near the target of $13\ m/s$, but during the turn, due to the rotation, the controller has more difficulty in attaining that speed. The Hybrid plane performance the turn with a radius of 120m. The controller is mainly using the control surface to performance the turn, which limits the vehicle turning rate.

The vehicle also takes more time to reach the maximum speed than the Hybrid Quadrotor, travelling

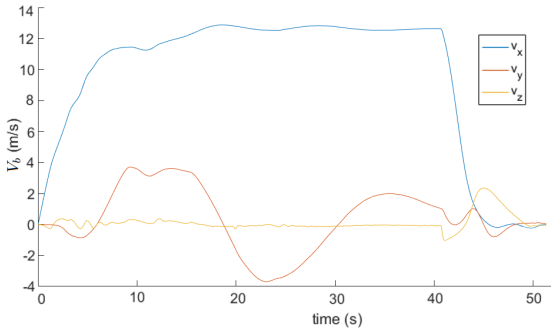

Figure 5.20: Hybrid Plane speed

further before starting to turn.

During the approach to the target position, it slightly overshoots it, but recovers to the desired position and stops.

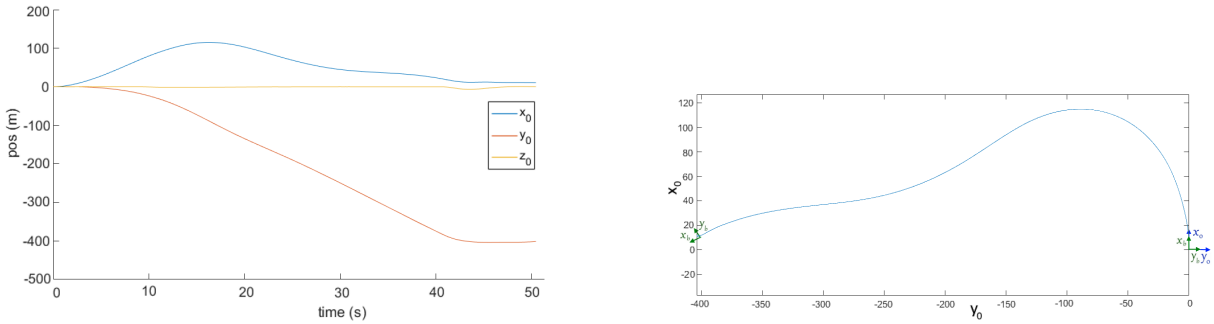

(a) Vehicle position

(b) Vehicle trajectory (top view), and orientation

Figure 5.21: Hybrid Plane position

Chapter 6

Conclusions

The first main objective of this thesis was the creation of a model capable of representing in detail the dynamics and kinematics of these types of hybrid vehicles. Special detail was necessary to handle the vehicle aerodynamics, as the vehicles are subjected to a wider range of scenarios. For the wings, the model proposed provides a close approximation to real word case by using curves from experimental data for the lift, drag and pitching moment coefficients, and covering the entire range for possible angles of attack. And the discretization of the wing allow to incorporate the effects of the vehicle rotation.

The propeller aerodynamics also have a major impact in the vehicle response. From the analysis to the models proposed, the difference in the approximations taken have a significant impact in the results for the propeller performance. And while for quadrotors or fixed wing aircrafts those effects are small, in these vehicles that is not the case. The propellers will be subject to significant lateral airflow, affecting the thrust and torque generated, and generating moments. They will also reach conditions of very high advance ratio, as the propellers are gradually turned off during the transition of the hybrid plane.

The final model for the propellers is one of the major contribution from this thesis to the area of hybrid quadrotors, and propellers in general. The inclusion of the effects of external airflow, a quadratic approximation for the lift coefficient, and including the moments generated due to the unbalance in the trust generated, it provides a closer approximation to real world results.

The model implemented in Simulink^{TM} is not specific just for these two vehicles, it can be used to simulate a wide variety of vehicles, within certain restrictions.

From the vehicles trim analysis it is visible the range increase in Forward flight compared to Axial flight, and what are the more efficient propellers for each vehicle. It is not possible however to conclude which is the more efficient approach, as the results are to close and some of the parameters of the vehicles, such as the weight, are estimations.

Another of the main objectives was to implement a control strategy capable of transitioning the vehicles trough the flight modes and able to handle disturbances. That objective was reached by combining the use of 4 LQR controllers per vehicle with an external loop to calculate weights to those controllers, and to alter the reference speed for a smother transition between controllers. This strategy proves enough to stabilise and control the vehicles in the presence of disturbances and with all the non lineari-

ties and irregularities present in the implemented model.

6.1 Future Work

The construction and testing of a real world prototype would provide further validation to the model proposed, including an in depth analysis of the propellers performance.

For the case of the Hybrid Plane, testing the use o two propellers in the back instead of one, to provide increased efficiency at high speed and remove the effects of the propeller torque in the vehicle rotation. It would also be interesting to analyse the vehicles performance with other motors and propellers.

Implement the models corresponding to the sensors, along with filters to reduce the noise from those. And further improve the control strategy proposed, to reduce the oscillatory effects noticed in the tests performed, and to be able to work with the limited number of state variables available through the sensors.

Bibliography

[1] Bell xv-3. https://en.wikipedia.org/wiki/Bell_XV-3. Accessed: 2016-9-20.

[2] Bell boeing v-22 osprey. https://en.wikipedia.org/wiki/Bell_Boeing_V-22_Osprey. Accessed: 2016-9-20.

[3] Ewr vj 101 supersonic vtol aircraft. http://www.diseno-art.com/encyclopedia/strange_vehicles/ewr_vj_101.html. Accessed: 2016-9-21.

[4] Lockheed martin f-35 lightning ii. https://en.wikipedia.org/wiki/Lockheed_Martin_F-35_Lightning_II. Accessed: 2016-9-21.

[5] Joby s2. http://www.jobyaviation.com/S2/. Accessed: 2016-9-20.

[6] Lilium. https://lilium.com. Accessed: 2016-9-20.

[7] Agustawestland aw609. https://en.wikipedia.org/wiki/AgustaWestland_AW609. Accessed: 2017-6-7.

[8] Dji phantom 4. http://store.dji.com/product/phantom-4?gclid=CPavlZSIlM8CFYky0wod_ywIxw. Accessed: 2016-9-21.

[9] Parrot bebop 2. https://www.parrot.com/fr/drones/parrot-bebop-2#parrot-bebop-2-. Accessed: 2016-9-22.

[10] The wingo. https://www.uavision.com/fixed-wing-uav-wingo/. Accessed: 2016-9-22.

[11] Amazon prime air. https://www.amazon.com/b?node=8037720011&ref=producthunt. Accessed: 2016-9-22.

[12] Textron demonstrates vtol aerosonde as it snags us army shadow contract. https://www.flightglobal.com/news/articles/textron-demonstrates-vtol-aerosonde-as-it-snags-us-a-424907/. Accessed: 2016-9-21.

[13] Jump 15. http://arcturus-uav.com/product/jump-15. Accessed: 2016-9-20.

[14] Ten-engine electric plane completes successful flight test. https://www.nasa.gov/langley/ten-engine-electric-plane-completes-successful-flight-test. Accessed: 2016-9-20.

[15] Dx korea 2016: Kari unveils tr60 tiltrotor uav. http://www.janes.com/article/63543/dx-korea-2016-kari-unveils-tr60-tiltrotor-uav. Accessed: 2016-9-22.

[16] Quadshot. https://transition-robotics.com/collections/quadshots. Accessed: 2016-9-23.

[17] Jumpship. https://transition-robotics.com/pages/jumpship. Accessed: 2016-9-21.

[18] Cebit 2016: Wingtra wants to be your hybrid drone. http://spectrum.ieee.org/tech-talk/robotics/drones/cebit-2016-wingtra-wants-to-be-your-hybrid-drone. Accessed: 2016-9-20.

[19] William J. Fredericks, Mark D. Moore, and Ronald C. Busan. Benefits of hybrid-electric propulsion to achieve 4x increase in cruise efficiency for a vtol aircraft. International Powered Lift Conference, 2013.

[20] Paul M. Rothhaar, Patrick C. Murphy, Barton J. Bacon, Irene M. Gregory, Jared A. Grauer, Ronald C. Busan, and Mark A. Croom. Nasa langley distributed propulsion vtol tilt-wing aircraft testing, modeling, simulation, control, and flight test development. AIAA AVIATION 2014 Conference, June 2014.

[21] Ronald C. Busan, Paul M. Rothhaar, Mark A. Croom, and Patrick C. Murphy. Enabling advanced wind-tunnel research methods using the nasa langley 12-foot low speed tunnel. AIAA AVIATION 2014 Conference, June 2014.

[22] E. Cetinsoy, S. Dikyar, C. Hancer, K.T. Oner, E. Sirimoglu, M. Unel, and M.F. Aksit. Design and construction of a novel quad tilt-wing uav. *Mechatronics*, 22:723–745, May 2012.

[23] Peter Ferrell, Brendan Smith, Brandon Stark, and YangQuan Chen. Dynamic flight modeling of a multi-mode flying wing quadrotor aircraft. International Conference on Unmanned Aircraft Systems, May 2013.

[24] Yann Ameho. *Du pilotage d'une famille de drones à celui d'un drone hybride via la commande adaptative*. PhD thesis, Institut Supérieur de l'Aéronautique et de l'Espace, 2013.

[25] Leandro R. Lustosa, François Defaÿ, and Jean-Marc Moschetta. Longitudinal study of a tilt-body vehicle: modeling, control and stability analysis. International Conference on Unmanned Aircraft Systems, 2015.

[26] Xinhua Wang and Lilong Cai. Mathematical modeling and control of a tilt-rotor aircraft. *Aerospace Science and Technology*, 47:473–492, October 2015.

[27] Menno Hochstenbach, Cyriel Notteboom, Bart Theys, and Joris De Schutter. Design and control of an unmanned aerial vehicle for autonomous parcel delivery with transition from vertical take-off to forward flight - vertikul, a quadcopter tailsitter. *International Journal of Micro Air Vehicles*, 7(4):395–405, December 2015.

[28] F. P. Beer and E. R. Johnston. *Vector Mechanics for Engineers*. McGraw-Hill, 7^{th} edition, 2006.

[29] Andrew H. Lind and Anya R. Jones. Unsteady airloads on static airfoils through high angles of attack and in reverse flow. *Journal of Fluids and Structures*, 63:259–279, April 2016.

[30] Andrew H. Lind, Jonathan N. Lefebvre, and Anya R. Jones. Time-averaged aerodynamics of sharp and blunt trailing edge static airfoils in reverse flow. *AIAA JOURNAL*, 52(12):2751–2764, December 2014.

[31] J. Gordon Leishman. *Principles of Helicopter Aerodynamics*. Cambridge University Press, 2^{nd} edition, 2006.

[32] Tommaso Bresciani. *Modelling, Identification and Control of a Quadrotor Helicopter*. PhD thesis, Lund University, 2008.

[33] Karolin Schreiter. Development and validation of a generic flight simulation based on aircraft geometry. American Institute of Aeronautics and Astronautics, 2011.

[34] Theoretical basis - aerodynamics. `https://www.apcprop.com/Articles.asp?ID=262#aero`. Accessed: 2017-1-15.

[35] Barnes W. McCormick. *Aerodynamics, Aeronautics, and Flight Mechanics*. Wiley, 2^{tnd} edition, 1995.

[36] Yau Lu, Chao yang Dong, and Qing Wang. Control allocation for aircraft with input constrains based on improved cuckoo search algorithm. *Defence Technology*, (13):1–5, 2017.

Appendix A

Vehicle Dimensions

Hybrid Quadrotor

Wingspan : $1.4m$ Length : $0.45m$	Propellers : 4 Motors : $4S$	Battery cells : 4 $ABLPA655275HG$	Wing surfaces : 2 Control surfaces : 0	

Total weight : $3.5Kg$	Motors : $4 \times 0.1Kg$ Propellers : $4 \times 0.015Kg$ Batteries : $4 \times 0.364Kg$ Electronics : $0.3Kg$ Wing : $1Kg$ Supports : $0.2Kg$

Wing	$x_b(m)$	$y_b(m)$	$z_b(m)$	$i_w(^\circ)$	$\zeta(^\circ)$	$A(m^2)$	$c_w(m)$	$l_c(m)$	$L_\sigma(m)$
S_1	0.05	-0.35	0	0	0	0.28	0.4	0.1	0
S_2	0.05	0.35	0	0	0	0.28	0.4	0.1	0

Propellers	$x_b(m)$	$y_b(m)$	$z_b(m)$	Orientation	Rotation
1 : 14×10	0.1	-0.4	0.45	x_b	$clockwise$
2 : 14×10	0.1	-0.4	-0.45	x_b	$counterclockwise$
3 : 14×10	0.1	0.4	-0.45	x_b	$clockwise$
4 : 14×10	0.1	0.4	0.45	x_b	$counterclockwise$

Table A.1: Hybrid Quadrotor specifications

Hybrid Plane

Wingspan : $1.5m$ Length : $1.4m$	Propellers : 5 Motors : 5	Battery cells : $4S\ 2P$ $ABLP8474J0HG$	Wing surfaces : 6 Control surfaces : 4	

Total weight : $4.5Kg$	Motors : $5 \times 0.1Kg$ Propellers : $5 \times 0.015Kg$ Batteries : $8 \times 0.222Kg$ Electronics : $0.3Kg$ Wings : $1.35Kg$ Supports : $0.5Kg$

Wing	$x_b(m)$	$y_b(m)$	$z_b(m)$	$i_w(^\circ)$	$\zeta(^\circ)$	$A(m^2)$	$c_w(m)$	$l_c(m)$	$L_\sigma(m)$
S_1	0.05	-0.55	0	8	0	0.14	0.4	0.1	0.1
S_2	0.05	-0.225	0	8	0	0.16	0.4	0.1	0.1
S_3	0.05	0.225	0	8	0	0.16	0.4	0.1	0
S_4	0.05	0.55	0	8	0	0.14	0.4	0.1	0
S_5	-0.9	-0.2	-0.17	0	-35	0.1	0.15	0.0375	0.1
S_6	-0.9	0.2	-0.17	0	35	0.1	0.15	0.0375	0.1

Propellers	$x_b(m)$	$y_b(m)$	$z_b(m)$	Orientation	Rotation
$1\ :\ 17 \times 8$	0.5	-0.4	0	$-z_b$	$clockwise$
$2\ :\ 17 \times 8$	-0.5	-0.4	0	$-z_b$	$counterclockwise$
$3\ :\ 17 \times 8$	-0.5	0.4	0	$-z_b$	$clockwise$
$4\ :\ 17 \times 8$	0.5	0.4	0	$-z_b$	$counterclockwise$
$5\ :\ 14 \times 10$	-0.4	0	0	x_b	$counterclockwise$

Table A.2: Hybrid Plane specifications

Battery cell	Energy (Wh)	Capacity(mAh)	Voltage (V)	Weight (Kg)
$ABLPA655275HG$	88.356	23880	3.7	0.364
$ABLP8474J0HG$	53.28	14400	3.7	0.222

Motor	$V_g(V)$	$R_m(ohm)$	$J_m(\frac{Nm}{s^2})$	$K_t(\frac{Nm}{A})$	$K_e(\frac{V\,s}{rad})$	$\tau_m(s)$	$L_m(H)$	$I_0(A)$	Weight (Kg)
	14.8	0.168	$10e^{-6}$	$10e^{-3}$	$12.5e^{-3}$	0.2	$1.1e^{-3}$	0.5	0.1

Table A.3: Batteries and Motor specifications

	N_p	$R_p(m)$	r_i	$c_p(m)$	$\theta_0(^\circ)$	$\theta_{tw}(^\circ)$	C_{L_α}	C_{L_M}	C_{L_Δ}	C_{D_0}	C_{L_α}
20×10	2	0.2540	0.1	0.034	60	-55	2.5	1	0.8	0.2	0.7
17×8	2	0.2159	0.1	0.030	38	-35	2.8	1.15	0.55	0.25	1.2
14×6	2	0.1778	0.1	0.027	35	-32	2.9	1.1	0.5	0.25	1.3
11×3	2	0.1397	0.1	0.022	22	-20	3.4	1	0.4	0.25	0.8
20×14	2	0.2540	0.1	0.034	60	-48	2.5	1	0.6	0.25	0.5
17×13	2	0.2159	0.1	0.030	48	-36	2.9	1	0.4	0.25	1.1
14×10	2	0.1778	0.1	0.027	50	-41	2.6	1	0.4	0.25	1.1
11×7	2	0.1397	0.1	0.022	50	-44	3	1	0.4	0.25	1.6
$20 \times 225EP$	2	0.2540	0.1	0.037	67	-50	2.2	1	0.4	0.25	0.5
17×18	2	0.2159	0.1	0.030	67	-50	2.2	1	0.4	0.25	0.8
14×13	2	0.1778	0.1	0.027	55	-41	2.6	1	0.4	0.25	1.2
11×10	2	0.1397	0.1	0.022	50	-34	2.6	1	0.4	0.25	1.1

Table A.4: Propeller model parameters